Politecnico di Milano

Department of Physics

Recombination Dynamics in Lead Halide Perovskites and the Role of Defects

Silvia Genaro Motti

PhD Dissertation

Supervisor:
Dr. Annamaria Petrozza

Tutor:
Prof. Guglielmo Lanzani

Chair of the Doctoral Program:
Prof. Paola Taroni

Doctoral Programme in Physics, XXXth Cycle

Milano, 2018

Table of Contents

List of Figures

List of abbreviations

BBO	Barium Borate
CCD	Charge-coupled Device
CB	Conduction band
CW	Continuous wave
DFE	Defect formation energy
DFT	Density functional theory
DMSO	Dimethyl-Sulfoxide
FWHM	Full width at half maximum
IR	Infrared
IPA	Isopropanol
$PbBr_2$	Lead Bromide
PbI_2	Lead Iodide
MA	Methylammonium
MABr	Methylammonium Bromide

MAI	Methylammonium Iodide
DMF	N,N-Dimethylformamide
NC	Nanocrystal
OPA	Optical Parametric Amplifier
PCBM	Phenyl-C61-butyric acid methyl ester
PB	Photo-bleach
PL	Photoluminescence
PLQY	Photoluminescence Quantum Yield
PV	Photovoltaic
PMMA	Poly methyl methacrylate
PEO	Polyethylene oxide
SHG	Second Harmonic Generation
SRH	Shockley-Read-Hall
SOC	Spin-Orbit Coupling
Spiro-OMeTAD	2,2',7,7'-Tetrakis [N,N-di(4-methoxyphenyl) amino]-9,9'-spirobifluorene
TCSPC	Time Correlated Single Photon Counting
TA	Transient Absorption
TOPO	tri-n-octylphosphine oxide
VB	Valence Band
XRD	X-Ray Diffraction
XPS	X-Ray Photoelectron Spectroscopy

Preface

The discovery and application of semiconductors make up to one of the most important advances in the history of science and technology, leading us from the early steps of computation to the current processing capabilities that could only be dreamed of not too long ago. Among the new generation of semiconductors, metal halide perovskites have been in the spotlight mostly due to the extraordinary performance achieved in photovoltaics, with conversion efficiencies that reached over 22% in less than a decade after the first device was reported in literature. Other promising applications such as light emitting diodes, photodetectors and lasers contribute to the increasing interest in the material. Some of the main reasons for this success are the high absorption coefficients, long carrier diffusion lengths and long carrier lifetimes, and also to the possibility of low cost solution-based fabrication. However, these convenient fabrication methods also imply in high density of defects in the material, and the presence of defects is also related to the material instability that still pose as one of the main challenges for reliable commercial application.

At the same time as we must study the nature and activity of the defects in order to improve material stability and performance, we also seek to understand the apparent defect tolerance in metal halide perovskites, that allowed for such impressive results achieved over the last few years.

Investigating defects in semiconductors usually require a combination of experimental techniques with computational studies. This thesis explores the photoluminescence properties, that are very sensitive to the presence of defects and provide a valuable tool for studying the material photophysics. The charge carrier dynamics of lead halide perovskites and how it's affected by the nature and activity of defects is investigated. Below, the contents of the following Chapters are summarized:

Chapter 1 defines basic concepts and figures of merit that will be discussed in the following Chapters. It also presents an overview on the structure and behavior of perovskite semiconductors, and some of the challenges for its optimization and application.

Chapter 2 describes the methods for sample fabrication and the optical spectroscopy techniques applied to the studies presented in this thesis.

Chapter 3 investigates the nature of defects in lead halide perovskites and their role on the carrier recombination dynamics. Different types of trapping sites are identified and the association of electron trapping to lattice deformation is shown, which could help explain the remarkable defect tolerance in this material.

Chapter 4 presents reversible variations of the semiconductor behavior that are observed as a quenching or an enhancement of the photoluminescence efficiency. The factors that regulate these photoinstabilities are discussed and related to the migration of ions under illumination.

Chapter 5 discusses the effects of oxygen and moisture in the efficiency and stability of the semiconductor and how these studies can help us develop efficient methods for thin film passivation and encapsulation. The surface treatment of perovskite thin films with polymer layers is demonstrated, resulting in improved short and long term stability and benefits to solar cell devices.

Chapter 6 briefly explores the properties of colloidal nanocrystals and how they could provide an insight into fundamental properties of metal halide perovskites.

Finally, **Chapter 7** summarizes the conclusions taken from the observations presented.

1

Introduction

Lead halide perovskites have been of great interest mostly due to the extraordinary performance achieved on photovoltaics, with conversion efficiencies that have reached over 22% in less than a decade after the first device was reported in literature. Other promising applications such as light emitting diodes, photodetectors and lasers contribute to the increasing interest in these materials. High absorption coefficients and long carrier diffusion lengths are some of the reasons for its success, but also the possibility of low cost solution-based fabrication. This Chapter will give an overview of the material structural and optoelectronic properties. It will also introduce some of the open questions and problems regarding defects and instabilities in perovskites, and give a brief theoretical background of recombination dynamics and how it can be explored to answer such questions.

1.1 Lead halide perovskites

The name perovskite depicts a family of materials with a crystal structure characterized by a ABX_3 formula, where A is a monovalent cation, X is a monovalent anion and B is an cation in 6-fold coordination, generally a 2+ metal. Oxide perovskites (where X=O) were the first of this family to attract great interest due to its magnetic and ferroelectric properties. Halide perovskites (where X = Cl, Br or I) have been studied

for over a century now,[1] but their promising opto-electronic properties have only been discovered in the 1990's, by Mitzi and coworkers, which demonstrated the possibility of application of halide perovskites as semiconductors on light emitting diodes (LEDs) and thin film transistors.[2–5]

The interest in the material grew dramatically with the application in solar cells, with power conversion efficiencies that increased from 3% to over 20% in less than a decade.[6] This steep improvement is unprecedented and it was particularly impressive in the case of a low cost material, processed by convenient solution based methods. Alongside the progress in PVs, perovskites have also promising light emitting applications, like LEDs[7,8] and lasers.[9–12] This success owes much to high absorption coefficients, and long carrier lifetimes.[13–15] There is still room for improvement, as the current power conversion efficiency record is still lower than the fundamental limit predicted by Shockley and Queisser, which is around 31% for materials with a similar band-gap[16,17]. However, most of the research effort nowadays has turned from the pursuit of higher efficiency to focus on other issues that hinder the commercial viability of perovskite solar cells, in particular the material instability.[18]

1.1.1 Crystal structure

The perovskite crystal structure was first reported for $CaTiO_3$ by the German mineralogist Gustav Rose and named after Russian mineralogist Count Lev Aleksevich von Perovski.[19] This type of material is characterized by a ABX_3 formula and the lattice is formed by corner sharing BX_6 octahedra and the A cation in the center, composing a crystal structure such as shown in Figure 1.1.

In the case of the semiconducting metal halide perovskites, B is a metal and X is either Cl, Br or I. Hybrid perovskites have an organic cation occupying the A site.

The crystal lattice has a pseudocubic symmetry. In the cubic structure, the BX bonds that form the octahedra are present at a right angle and equal lengths and $a = b = c$. However, the perovskite family includes variations, for example in tetragonal ($a = b \neq c$) or orthorhombic ($a \neq b \neq c$) symmetry.

The main subjects for the studies in this thesis are methylamonium lead iodide ($MAPbI_3$) and methylamonium lead bromide ($MAPbBr_3$), two of the most commonly studied semiconducting perovskites. $MAPbI_3$ adopts a tetragonal crystal structure at room temperature and undergoes a phase transition between 130K to 160K to an orthorhombic structure. At higher temperatures, the lattice adopts a cubic symmetry,

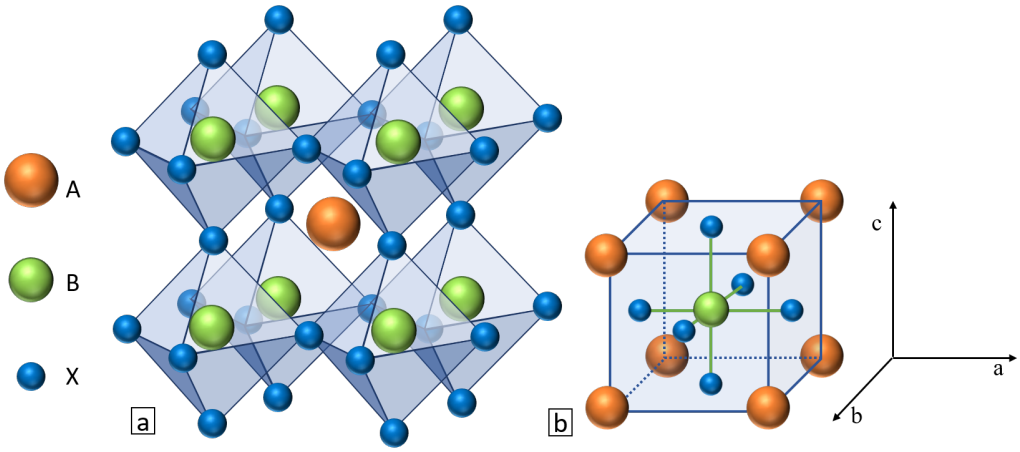

Figure 1.1: a) Perovskite lattice structure; b)Perovskite unit cell.

with a phase transition around 330 K. $MAPbBr_3$ adopts a cubic structure at room temperature. The phase trasition from tetragonal to the cubic structure occurs around 240K.[20]

Metal halide perovskites are formed by ions bound predominantly by relatively weak electrostatic interactions and this results in a soft nature of the lattice, that is subject to instabilities and structural deformations depending on the morphology and environmental conditions.[21–23]

1.1.2 Electronic structure

Metal halide perovskites, unless fabricated in confined configurations (such as colloidal nanocrystals or layered structures with dielectric confinement), are three dimensional semiconductors and can be described with an electronic band structure, where the valence band (VB) maximum and the conduction band (CB) minimum are separated by an energy gap E_G. The band structure of a semiconductor can form either a direct or indirect band-gap. In the direct case, the VB maximum and the CB minimum occur at the same point in the Brillouin zone. The occupation of the bands follow the Fermi-Dirac statistics, and the probability of occupation of a band of energy E by an electron, at a certain temperature T is given by:

$$f(E) = \frac{1}{1 + e^{(E-E_F)/k_B T}} \tag{1.1}$$

where k_B is the Boltzmann constant and E_F is the Fermi level. In the ideal ground state of an intrinsic semiconductor, at 0 K, the Fermi level lies exactly in the center of the band-gap, i.e. the VB is completely filled and the CB is completely empty, as illustrated in Figure 1.2.

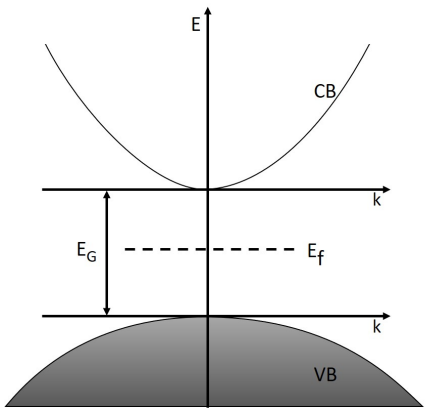

Figure 1.2: Occupation probability function of an intrinsic semiconductor in equilibrium in the ground state, at 0 K.

Experimental data and density functional theory (DFT) calculations determined that the most commonly studied lead halide perovskites are direct band-gap semiconductors,[24] despite the long carrier lifetimes in these materials that are similar to what is expected of indirect band-gap semiconductors. There has been some evidence of a slightly indirect gap in lead halide perovskites[25,26], possibly induced by Rashba-splitting of the bands.[27,28]

The band structure of lead halide perovskites is dictated by the Pb-X lattice, where an antibonding hybrid orbital between the s orbitals of Pb and p orbitals of X compose the VB maximum, while the CB minimum is formed by a non-bonding hybrid state between the p orbitals of Pb and the p orbitals of X.[29,30] As a consequence to that, the band-gap of the material can be tuned by changing the halide composition, from lead iodide perovskites with band-gap around 1.6 eV to wider gaps around 2.4 eV in lead bromides and 3 eV in lead chlorides, covering the whole visible range. Mixed halide compositions result in intermediate band-gaps. Although the orbitals of the A site cation do not contribute to the formation of the VB maximum and CB minimum, its size and shape regulates the distances and angles of the metal halide lattice, afecting the electronic structure and fine tuning the band-gap. For example, smaller cations result

in higher band-gaps, such as the case of $CsPbBr_3$, that has a band-gap around 10 meV wider than $MAPbBr_3$. Furthermore, differences in lattice distortions and crystalinity resulting from variations in the fabrication methods also have an impact in the fine electronic structure.[31,32]

Impurities and lattice distortions can cause energetic disorder in the semiconductor resulting in a distribution of electronic states at the band-edge. The distribution of these states can be modeled as an exponential tail stretching from the conduction band, that is commonly refered to as Urbach tail and described by[33]:

$$exp(\frac{\sigma(h\nu - E_U)}{kT}) \tag{1.2}$$

where E_U is the Urbach energy.

1.1.3 Optical absorption

The absorption of a photon with energy equal or higher than E_G induces the transition of an electron from the VB to the CB, resulting in a hole in the VB. In the dipole approximation, the photon wavevector is negligible compared to the reciprocal space unit of the crystal lattice, and only vertical transitions are optically allowed. In indirect gap semiconductors, the conservation of momentum is maintained by additional absorption or emission of phonons. The resulting electron and hole have opposite momentum and their respective kinetic energies depend on the curvature of the VB and CB, which can also be represented by their effective masses (m^*).[34] When an absorbed photon has $\hbar\nu > E_G$, the excess energy is converted into kinetic energy.

For metal halide perovskites, the effective masses of electrons and holes are similar ($m_e^* \approx m_h^*$), so the excess energy is approximately equally balanced between the two charge carriers. Immediately after the absorption, the photogenerated carriers are out of equilibrium. In a few hundred femtoseconds, elastic and inelastic scattering re-distributes the momentum and establishes a thermal distribution of the carrier population, normally with a higher tamperature than the lattice. This hot carrier distribution relaxes by electron-phonon interaction, reaching the lattice temperature in a few ps.[34] After this first regime of relaxation, when the lattice and carriers are in thermal equilibrium, the excess of photogenerated carriers return to the ground state by radiative or non-radiative recombination processes, which occur at longer time scales, up to tens or hundreds of nanoseconds in metal halide perovskites.

Figure 1.3 shows the absorption and photoluminescence (PL) spectra of $MAPbI_3$,

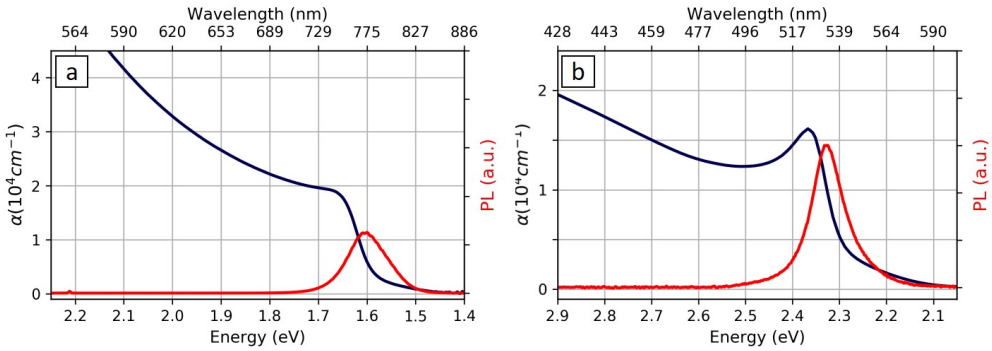

Figure 1.3: Absorption (dark blue) and photoluminescence (red) spectra of a 500nm thick polycrystalline film of $MAPbI_3$ (a) and 300nm thick film of $MAPbBr_3$ (b).

featuring a band-gap around 1.6 eV, and $MAPbBr_3$, with a band-gap around 2.4 eV.

1.1.4 Excitons

One striking feature in the lineshape of the absorption spectra, particularly in the case of $MAPbBr_3$, is the presence of a peak at the band-edge corresponding to the absorption of excitonic states.[35]

Excitons are quasi-particles resulting from the Coulomb interaction between an electron and hole pair, and can be regarded as a hydrogen atom system according to the Wannier-Mott exciton model, delocalized over a certain Bohr radius.[36] The binding energy (E_b) of the exciton is essentially the energetic spacing between the excitonic state and the edges of the VB and CB. Light absorption at the band-edge is regulated by E_b. A series of hydrogen resonance lines affect the optical absorption of the semiconductor, as can be described by Elliot's equation[37,38]:

$$\alpha(\nu) \propto \frac{\mu_{cv}^2}{\hbar\nu}\left[\sum_{n=1}^{\infty}\frac{4\pi\sqrt{E_b^3}}{n^3}\delta(\hbar\nu - E_G + \frac{E_b}{n^2}) + \frac{2\pi\sqrt{E_b}\theta(\hbar\nu - E_G)}{1 - e^{-2\pi\sqrt{\frac{E_b}{\hbar\nu - E_G}}}}\right] \tag{1.3}$$

where $\alpha(\nu)$ is the absorption coefficient for a certain frequency of light, n is a positive integer and μ_{cv} is the transition dipole moment.

Figure 1.4 shows the experimental absorption spectrum of $MAPbBr_3$ and the fitted result of Elliot's equation. The dashed lines shows the individual contributions of the band-to-band absorption without the effect of Coulombic interactions and the excitonic resonance at the band-edge. Only one resonance level is considered here. The excitonic

effects in a 3D semiconductor increase the absorption cross section, resulting in higher absorption coefficients across the whole absorption spectrum. This is made clear by the increase of α from the band to band absorption coefficient without Coulombic interactions (plotted as a light blue dashed line) to the α obtained from Equation 1.3 (solid dark blue line). This absorption enhancement is beneficial for PV applications, maximizing the light harvesting properties. On the other hand, the bound electron hole pairs require some additional energy to be dissociated and usually have higher recombination rates, hampering charge extraction.

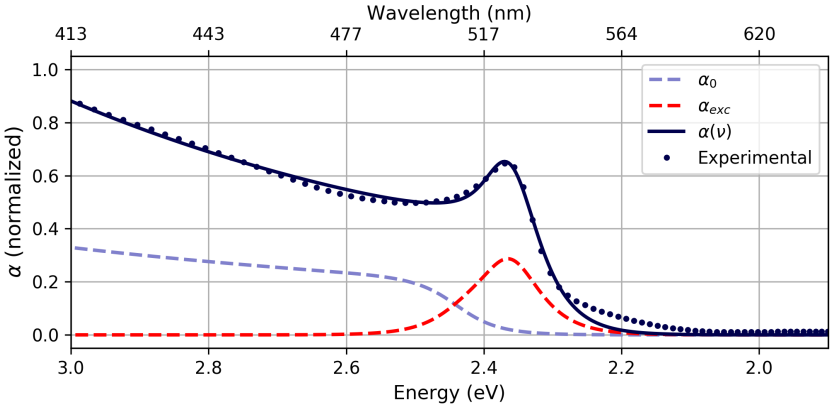

Figure 1.4: Absorption spectrum of a $MAPbBr_3$ thin film (data points) and the fit of equation 1.3 (solid line). The individual contributions of the excitonic absorption (red) and the band-to-band absorption without Coulombic interactions (light blue) are plotted in dashed lines.

According to the model descibed by Saha,[39] at thermodynamic equilibrium, the populations of excitons and free carriers is dictated by E_b, the excitation density, and the temperature. The role of excitons in the photophysics of lead halide perovskites has been long discussed, but except for nanocrystals or layered configurations presenting some level of confinement, the values determined for the exciton binding energy in these materials is low when compared for example to organic materials. Values for E_b have been reported from 2 meV to 60 meV, with lower values for lead iodide perovskites compared to lead bromides.[40–43] As a consequence, most of the data analysis and theoretical models found in the literature neglect the population of excitons in the solar cell operating regime at room temperature[38,40], although their contribution to light emission at certain conditions has been considered.[44,45]

1.1.5 Photoluminescence

After absorption of excitation light and thermalization of the photo-generated carriers to the band-edges (Figure 1.5a), the system relaxes back to the ground state through different mechanisms of electron-hole recombination. The energy resulting from the transition of electrons back to the VB can be released as a photon in a radiative process (Figure 1.5b). Alternatively, carriers can recombine non-radiatively.

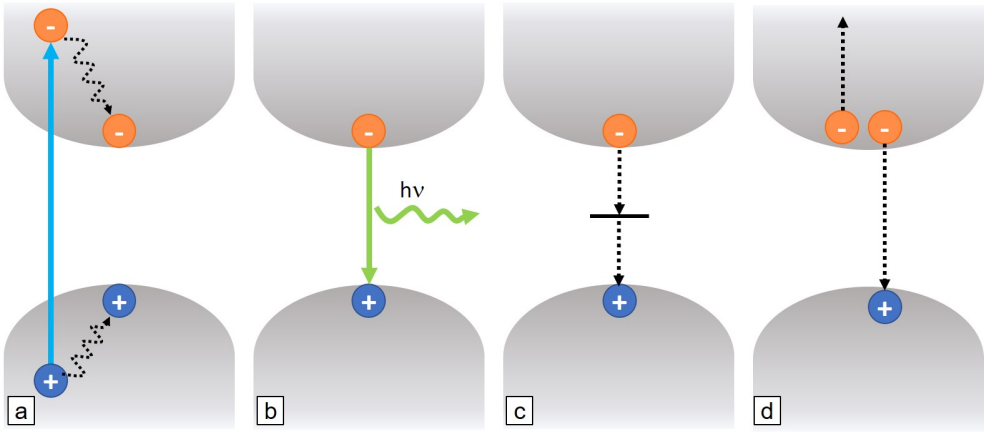

Figure 1.5: a) Thermalization of carriers after photoexcitation; Carrier decay to the ground state by b) Radiative recombination, c) trap-assisted recombination and d) Auger recombination.

The main channels for non-radiative recombination are trap-assisted, when a carrier is trapped in a localized intra-gap state and then recombines with a carrier of opposite charge (Figure 1.5c), and Auger recombination. In the Auger process, the energy of a recombining electron-hole pair is transferred to a third carrier that is excited to higher energy levels (Figure 1.5d). This excess energy is released as heat as the carrier relaxes back to the band-edge. Being a three-body mechanism, Auger recombination becomes relevant at high carrier densities. The radiative recombination of an electron and hole pair can be directly observed as photoluminescence (PL), and for a direct band-gap semiconductor with weak carrier-phonon coupling, Stokes shift is close to zero and the energy of the emitted photons is centered right at the band-gap. The PL decays reflect the combination of relaxation channels in the system, as they depend on the carrier population in the excited state. The depopulation of the excited state can usually be described by a rate equation:

$$\frac{dn}{dt} = -R(n) - k_t n - \gamma n^3 \tag{1.4}$$

where $R(n)$ is the radiative recombination rate, k_t is the the rate constant of carrier trapping and γ is the third order rate constant that describes non radiative Auger recombination. The PL lifetimes are also related to the carrier diffusion lengths according to:

$$L_D(n) = \left(\frac{\mu k_B T}{e R_T(n)} \right)^{1/2} \tag{1.5}$$

where L_D is the diffusion length, μ is the carrier mobility, k_B is the Boltzmann constant, T is the temperature and e is the elementary charge. R_T is the total recombination rate, related to the PL lifetime τ by $R_t = 1/\tau$.[15]

Section 1.3 will describe in more detail the excited state dynamics of perovskites and how the PL can provide valuable information on the material properties.

1.1.6 Photovoltaic application

The first succesful application of perovskites on photovoltaics (PVs) was reported by Miyasaka and coworkers in 2009, achieving 3.8% of power conversion efficiency from a dye-sensitized solar cell (DSSC) device in which $MAPbI_3$ was used as a sensitizer on a TiO_2 scaffold.[46] After significant improvement of performance reported over the following years, Lee et al. reported in 2012 that, remarkably, after replacing the TiO_2 for an inert AlO_2 scaffold, 10.9% efficiency was achieved.[47] With improvement of fabrication methods, the conversion efficiency approached 20% in the following couple of years,[6] and has reached 22.1% up to the present day.

In general, solar cells are built on a transparent substrate covered with a transparent conductive oxide (for example tin oxide or indium tin oxide). The photoactive material is placed between the oxide electrode and a metallic electrode, with charge-selective transport layers in between, and light comes through the transparent side (Figure 1.6a). The charge transport layers are usually wide band-gap materials whose band alignment with respect to the absorber promote either electron or hole transfer (Figure 1.6b). The most common ETL and HTL materials are TiO_2, 2,2',7,7'-Tetrakis[N,N-di(4-methoxyphenyl) amino]-9,9'-spirobifluorene (Spiro-OMeTAD), Phenyl-C61-butyric acid methyl ester (PCBM), and poly(3,4-ethylenedioxythiophene)-polystyrene sulfonate (PEDOT:PSS).

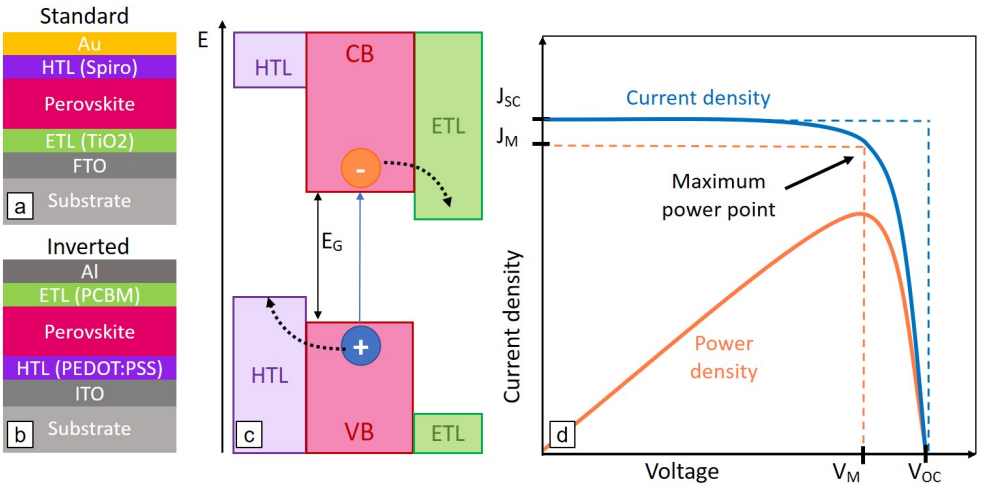

Figure 1.6: Common solar cell architectures, in standard (a) or inverted (b) structure, depending on the position of the electron transport layer (ETL) and the hole transport layer (HTL); b) Band diagram illustrating the band alignment of the ETL and HTL with respect to the photoactive semiconductor; c) Typical current density voltage curve of a solar cell.

For a semiconductor to be suitable for PV applications, it should first of all have high absorption coefficients, preferably with a low band-gap, so that a thin layer of material is able to efficiently capture sun light. As seen in Figure 1.3a, $MAPbI_3$ has a strong absorption coefficient and a low band-gap, making it a good absorber that covers most of the solar spectrum. Long carrier lifetimes, i.e., long diffusion lengths,[13,48] are also desirable, as it allows for efficient charge extraction by the electrodes. Furthermore, the maximum power conversion efficiency can only be achieved when the non-radiative recombination of carriers is negligible, that is, when the radiative efficiency is 100%.[49,50] The PLQY is therefore an important parameter to be optimized in photoactive materials for PV applications[51].

Solar cell devices can be characterized by the current density (J) as a function of voltage (V) between the two terminals (Figure 1.6c). The maximum power ($P = J \cdot V$) is reached at a voltage V_m and current density J_m. The maximum current density output is J_{SC} and the maximum device photovoltage is the open circuit voltage (V_{OC}), corresponding to the point in which the current equals zero. The ratio between $J_m \cdot V_m$ (marked as the orange dashed square in Figure 1.6c) and $J_{SC} \cdot V_{OC}$ (blue dashed square in Figure 1.6c) is the device fill factor ($FF = \frac{J_m \cdot V_m}{J_{SC} \cdot V_{OC}}$). The efficiency ($\eta$) of the solar

cell is the ratio of power density output by the power density of incident light (P_s)[52] and can be described by:

$$\eta = \frac{J_{SC} \cdot V_{OC} \cdot FF}{P_s}$$

The maximum V_{OC} achievable, as predicted by Shockley and Queisser,[16] varies with the band-gap of the material. The real V_{OC} is limited by the recombination channels. When other channels compete with radiative recombination, the V_{OC} decreases, making this parameter closely related to the losses in the semiconductor.

1.2 Challenges: Defects and instabilities

Some of the key factors for the success of metal halide perovskites are also related to issues that are yet to be solved before the material reaches the market. Metal halide perovskites are ionic materials that can be fabricated using solution-based methods close to room temperatures. Although these mild processing conditions are interesting for low cost device fabrication and flexible applications, they might also result in a high probability of defects.[53] These defects and the relatively weak electrostatic interactions that form the lattice are also related to high ion mobility and structural deformations.

As much as metal halide perovskites have shown impressive power conversion efficiency and high photoluminescence efficiency, one of the main challenges for a commercial application of perovskites in devices is improving the stability of the material, which suffers from the degradation of the material in the long term, but is also affected by reversible changes of the photo and electrical behavior over varied time scales.

1.2.1 Native crystalline defects

Imperfections in crystalline solid materials can be divided into point defects or higher dimensional defects like grain boundaries, line dislocations, rotations or large defective volumes. Figure 1.7 illustrates the types of point defects in a unit cell of a crystal lattice composed by two types of ions, that can be vacancies, interstitials, antisites or impurities. For ionic crystals, these defects can either be neutral or charged, and include pairs such as anti-sites (where an ion take another's ideal position), Frenkel defects (a

vacancy and an interstitial of the same ion) and Schottky defects (two vacancies of oppositely charged ions).

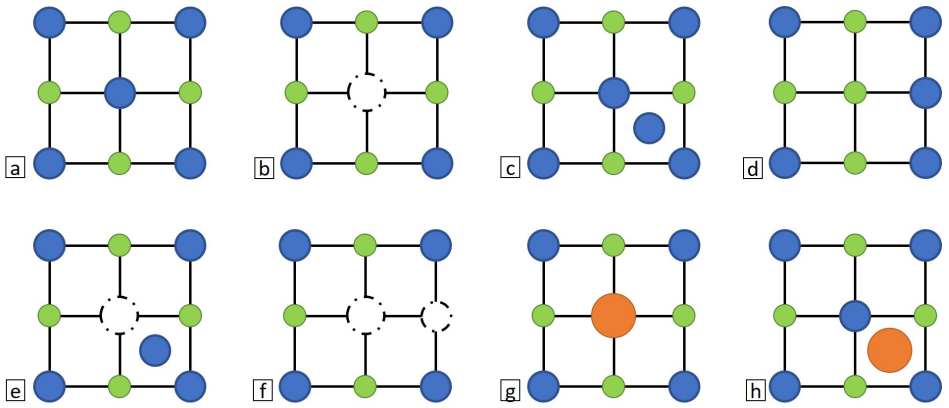

Figure 1.7: Point defects in a crystalline solid. a) Ideal lattice; (b) vacancy; c) interstitial; d) anti-site; e) Frenkel pair; f) Schottky pair; g) Substitutional impurity; h) Interstitial impurity.

Native point defects are the most studied type of defects in lead halide perovskites. In $MAPbI_3$, for example, the possible types of defects are vacancies V_{MA}, V_{Pb} , and V_I, interstitials MA_i, Pb_i , and I_i and anti-site I_{MA}, I_{Pb}, Pb_{MA}, Pb_{MA}, Pb_I, MA_{Pb}, and MA_I.

Detecting specific defects is a difficult task, but their presence and properties can be predicted theoretically. Density Functional Theory (DFT) is commonly used to calculate the defect formation energies (DFE). The DFEs are typically calculated from the chemical energy required to form a defect from the constituting materials and the energy associated to the exchange of electrons with the Fermi level of the system. The defects with the lowest DFEs are the more stable ones, and therefore assumed to be the the types present in higher densities. Varying the Fermi energy across the semiconductor band-gap, from the maximum of the VB to the minimum of the CB, also varies the DFE of a charged defect. When the DFEs of a defect at different charge state meet, it defines the point at which the defect can change its charge state by acquiring electrons or holes. When the energy state of a defect is located within the semiconductor band-gap it can act as a trap site for a charge carrier. The trapped carrier can be detrapped and return to the CB (in the case of an electron) or to the VB (in the case of a hole), or it can recombine with a free carrier of opposite charge. This trap assisted recombination is usually detrimental for the semiconductor performance as it limits the free carrier

lifetime.

Values for the density of trap states in polycrystalline $MAPbI_3$ have been reported in the literature varying around 10^{15}-10^{16} cm^{-3}.[22,54] Such values are quite high when compared to the trap densities in other semiconductors that are used for PV applications with similar performance. For example polycrystalline Silicon (10^{13}-10^{14} cm^{-3}),[55] single crystal Si (10^{8} cm^{-3}),[56] CdTe (10^{13}-10^{15} cm^{-3}),[57] and CIGS (10^{13} cm^{-3}).[58]

The surprising high efficiency achieved in polyscrytalline $MAPbI_3$ PV despite its high defect density has prompted research efforts in trying to understand the nature of trapping sites in this type of material and the reasons for this defect tolerance. One explanation is that the majority of defects in the bulk of $MAPbI_3$ have energy levels in the conduction or valance bands or relatively close to those, making them shallow trap states. The larger formation energies calculated for defects that can form deep trap states imply these defects are probably not present in relevant densities.[59] Chapter 3 will discuss the nature of trap states in $MAPbI_3$ and $MAPbBr_3$ and how the carrier trapping and detrapping dynamics could contribute to the defect tolerance.

1.2.2 Instabilities in lead halide perovskites

There has been a large variability in perovskite properties reported in the literature. Transformations have been observed occurring in these materials, detected as transient behaviors in electrical response, optical properties or structural characterization, as a response to different stimuli. The inconsistencies in experimental observations are related to intrinsic instabilities in the material, mainly electronic and structural changes occurring on different time scales and induced by the experimental conditions such as light soaking, atmosphere, external bias and sample microstructure. These transformations can be divided into i. Irreversible material degradation; ii. Reversible changes occurring in the presence of applied electric fields and charge transfer and iii. Reversible photoinduced changes in bare perovskite samples. It is not in the scope of this work to investigate the irreversible degradation mechanisms, but these will be briefly discussed in Chapter 5. The instabilities present in working devices will also not be discussed, as other works have been dedicated to that. This work focus instead on the reversible photoinstabilities, and the transformations occuring on bare lead perovskite films on inert substrates.

One particular characteristic of metal halide perovskites is the migration of ions through the lattice.[60] Much effort has dedicated to studying the ion mobility and their

effects on photocurrent hysteresis in perovskite solar cells.[61–64] The migration of ions is also related to several unusual properties of metal halide perovskites like the photoinduced phase segregation in mixed halides,[65–68] photoinduced poling,[69,70] and switchable photovoltaic effect.[71] Iodine, bromine and the A-site cation are generally considered as the major migrating species.[72–74] In the case of $MAPbI_3$, for example, iodine is reported to be the most mobile ion, followed by MA and then Pb.

deQuilettes et al. reported the PL enhancement in $MAPbI_3$ films in inert atmosphere and has linked the phenomenon with the halide migration through the films.[67] Mosconi et al. proposed a photoinduced healing mechanism to explain the PL enhancement observed as a result of Frenkel defect annihilation.[75] That is, a Frenkel pair formed by an iodide vacancy and an interstitial would recombine resulting in the healed crystal lattice. Such process would be triggered by illumination, due to the lower energy barriers for the halide migration in the photoexcited state. The opposite has also been observed, i.e. a quenching process triggered by illumination. Chapter 4 will discuss these observations and the parameters that regulate the different effects. Furthermore, it has been observed that lead halide perovskites are extremely sensitive to the atmosphere,[76–79] as will be discussed in Chapter 5.

1.3 Photoluminescence as a probe for defects

Monitoring the photoluminescence (PL) quantum efficiency and dynamics is an effective approach for gathering information about the opto-electronic properties of a semiconductor.[80] The PL decays usually are closely correlated to the carrier lifetime in the material and it also reflects the density of trapping defects and non-radiative channels. It is an alternative approach to probe the semiconductor properties and the material stability without the presence of electrodes, applied electric fields and interfaces that might have an effect on the material behavior. As this Section will show, the PL dynamics are determined by a combination of parameters such as recombination rate constants, trap state densities, and non-radiative recombination rates.[81] This makes the PL intensity extremely sensitive to small variations in the material properties that normally can't be perceived by other optical techniques.

1.3.1 Shockley-Read-Hall Recombination

As mentioned in Section 1.2.1, defects in the lattice can create electronic states between the VB and CB with the ability to trap electrons or holes. The trapped carrier can either be released as a free carrier by thermal activation or recombine non-radiatively with a free carrier of opposite charge. The Shockley-Read-Hall (SRH) model for carrier recombination has generally been applied to doped semiconductors, such as the case of silicon solar cells. In a highly doped semiconductor, the trapped carrier immediately recombines with the excess carriers of the opposite charge and the excited state dynamics are determined by the trapping lifetime of the minority carrier. Although lead halide perovskites can be considered as only lightly doped semiconductors, SRH recombination has been reported as the dominant decay path at low excitation intensities.[54,82–84]

The most commonly used description of this process is the SRH expression for the rate of trap assisted recombination:

$$R_{SRH} = \frac{np}{\tau_n(p+p_t)+\tau_p(n+n_t)}$$

where n and p are the densities of electrons and holes, respectively, n_t and p_t are the density of trapped electrons and holes, and $\tau_{n,p} = \frac{1}{\beta_{n,p}N_t}$ is the lifetime of electron/hole trapping, where N_t is the total density of available trap states and $_{n,p}$ is the coefficient for carrier recombination rate. When N_t is much larger than the density of free carriers, it can be consider that the trap assisted recombination is the dominant decay path for carriers. The excited state decay can then be described by:

$$\frac{dn}{dt} = -\beta_n N_t n$$

In this regime, the relaxation of the system follows monomolecular dynamics, and accordingly, the resulting PL dynamics is a monoexponential decay and the PL intensity will have a linear dependence on the excitation intensity.

1.3.2 Recombination dynamics

A system of rate equations adapted from the model reported by Stranks et al.[83] was used to simulate the evolution of populations of free electrons, free holes and trapped carriers. For simplification, the model considers one single type of trap, as it takes into account that in the presence of both holes and electrons traps, the more abundant

type would have a dominant effect on the dynamics. Here it's considered that the electron traps are dominant based on experimental data.[54] The rate equations for the populations of free and trapped carriers are:

$$\frac{dn_e}{dt} = G - \beta_{rad} n_e n_h - k_t n_e (N_t - n_t) - \gamma n_e n_h^2 \tag{1.6}$$

$$\frac{dn_h}{dt} = G - \beta_{rad} n_e n_h - R_t n_h n_t - \gamma n_e n_h^2 \tag{1.7}$$

$$\frac{dn_t}{dt} = k_t n_e (N_t - n_t) - R_t n_h n_t \tag{1.8}$$

where n_e is the population of free electrons, n_h the free holes and n_t the trapped carriers, G is the photogeneration rate, $\beta_r ad$ is the radiative recombination rate constant, γ is the Auger recombination rate constant, k_t is the trapping rate constant, N_t is the density of available traps, and G_n is the rate constant of recombination of a trapped electron with a free hole. The PL intensity at a given time can be obtained by

$$I_{PL} = \beta_{rad} n_e n_h \tag{1.9}$$

When $G = 0$ and the initial electron and hole populations are set as the density of absorbed photons right after a short pulse of excitation light, the PL decays can be obtained from 1.9 and can be fitted to the experimental data. The steady state conditions can be simulated setting the initial populations to zero and defining the generation rate G as the absorbed photons over time according to the illumination conditions.

1.3.3 Trap filling

The PL intensity can be obtained as a function of the excitation intensity I_{pump} from the steady-state solution of the three rate equations 1.6-1.8. As a consequence of the two competing recombination paths (trap-assisted and bimolecular) the solution is characterized by two different regimes.

At low excitation intensity, when $N_t >> n_e$, the most likely recombination path for electrons is through trapping, which is a monomolecular process. On the other hand, the dynamics of holes will be determined by the recombination of free holes with trapped electrons, which is a bimolecular process. In other words, the free electron density will increase linearly with excitation intensity and the free hole density will increase with

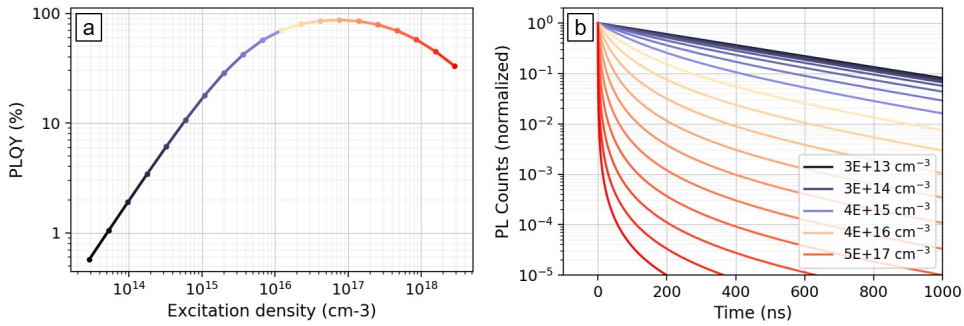

Figure 1.8: Simulated a) PLQY and b) PL dynamics.

the square root of the intensity. The steady-state PL intensity resulting from the the density of free carriers will therefore scale superlinearly as

$$I_{PL} \propto I_{pump}^{3/2} \tag{1.10}$$

At higher excitation intensities, as the density of photo-generated carriers reaches the density of trap states, the radiative recombination of free electrons and holes becomes dominant. The free carrier recombination is a bimolecular process, thus the steady state PL intensity transitions to a linear dependence on the excitation intensity. Finally at even higher intensities, third order processes such as Auger and Auger-like recombination start becoming relevant, resulting in a sublinear dependence on excitation intensity.

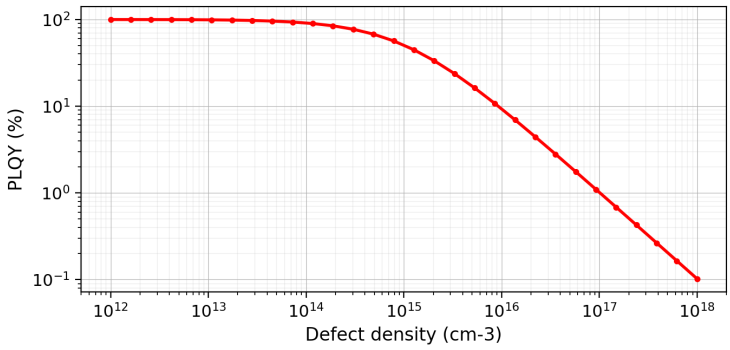

Figure 1.9: Simulated PLQY at excitation density 10^{15} cm^{-3}, as a function of defect density.

Figure 1.9 shows the PLQY at a fixed excitation density of 10^{15} cm^{-3} simulated for different defect densities, illustrating the impact of defects on the PLQY in the region where $N_t > n_e$. Although the maximum value of PLQY when $N_t < n_e$ is shown as 100%, a metal halide perovskite thin film with 100% PLQY has not been reported to date. In reality there are several non-radiative paths that are not taken into account in this simplified picture, as well as the role of interface recombination and photoinduced creation of additional loss channels.

As a consequence to the trap limited behavior of the excited state dynamics, the PL efficiency and lifetimes are very sensitive to the presence of defects. Not only does this allows us to probe the quality of different samples by probing the PL properties, it also allows us to monitor structural instabilities in the films that result in variations in defect composition and therefore fluctuation of PL efficiency.

2

Methods

2.1 Sample fabrication

This work contemplates lead halide perovskites of different compositions, namely $MAPbI_3$, $MAPbBr_3$ and $CsPbBr_3$. The samples studied in this work were solution deposited polycrystalline thin films. The quality of the films and the absence of precursor residues could be asserted by X-Ray Diffraction (XRD) measurements.

Lead(II) bromide ($PbBr_2$, 98%), N,N-dimethylformamide (DMF, anhydrous, 99.8%), Chlorobenzene (anhydrous, 99.8%), and dimethyl sulfoxide (DMSO, anhydrous, 99.9%) were purchased from Sigma-Aldrich; methylammonium bromide (MABr) and methylammonium iodide (MAI) were purchased from Dyesol; and lead (II) iodide (PbI_2, 99.9985%, CAS No. 10101-63-0) was purchased from Alfa Aesar. All chemicals were used without any further purification. Glass substrates were cleaned in acetone and isopropyl alcohol (IPA) for 10 minutes by sonication. The cleaned glass substrates were treated with Oxygen plasma for 10 minutes before any further deposition. All samples were prepared inside gloveboxes under N_2 atmosphere. The methods for preparing the samples are described below.

$MAPbBr_3$ thin films:

The film deposition was based on a Nanocrystal-Pinning technique reported by Cho et al.[85] The films were spin-coated in two steps (500 rpm for 7 seconds, then 3000 rpm for 90 seconds). A precursor solution of MABr and $PbBr_2$ (molar ratio 1.05:1) in DMSO was spin-coated onto the clean glass substrate. After 60 seconds, 300 µl of

chlorobenzene was dropped on the spinning sample. The samples were then annealed at 90°C for 10 minutes.

$MAPbI_3$ thin films:

The deposition was performed with quenching of the precursor solution with toluene as an antisolvent during spin coating, based on the procedure reported by Xiao et al.[86] A 1.45 M precursor solution of PbI_2:MAI:DMSO in a molar ratio of 1:1:1 was prepared in DMF. This solution was spin coated onto the glass substrate at 4000 rpm, with an acceleration of 4000 rpm/s, for 15 s. After 6 seconds, toluene was dropped onto spinning sample. The samples were then annealed at 100°C for 10 minutes.

Isolated, micrometer sized, $MAPbBr_3$ crystallites:

$MAPbBr_3$ crystals were formed by adding 150 µl of a solution of MABr and $PbBr_2$ in DMF (molar ratio 1:1, 30 wt% concentrated) to a solution of an antisolvent, in this case 3 ml of chlorobenzene. After injection of the precursor solution, micrometer-sized crystals precipitate instantaneously. The crystals were then deposited on clean glass substrates, and left to dry at room temperature.

2.2 Steady state characterization

2.2.1 Absorption

Absorption measurements on thin films or solutions in quartz cuvettes were performed using a spectrophotometer (Perkin Elmer Lambda 1050). The obtained values for absorbance allows us to estimate the density of photogenerated carriers as:

$$n_0 = \frac{P \cdot \lambda_{pump}}{RR \cdot h \cdot c \cdot A \cdot \delta(\lambda_{pump})} \tag{2.1}$$

where λ_{pump} is the wavelength of the excitation light, P the incident power, RR the repetition rate, A the area of the illuminated spot, h the Planck constant* and c the speed of light. The term $\delta(\lambda_{pump})$ is the penetration depth of the excitation light at the wavelength used, and can be obtained from the absorption measurements according to Lambert-Beer law:

*$h = 6.626070040 \cdot 10^{-34} J \cdot s$

$$I_T = (I_0 - I_R) \cdot e^{-d \cdot \alpha(\lambda)} \tag{2.2}$$

$$\delta(\lambda_{pump}) = \alpha(\lambda_{pump})^{-1} \tag{2.3}$$

where I_0 is the intensity of the incident light, I_T the intensity of transmitted light, I_R the intensity of reflected light, α is the absorption coefficient for a given wavelength and d is the sample thickness.

2.2.2 Photoluminescence

Most of the steady state Photoluminescence (PL) spectra reported in this thesis, as well as the evolution of steady state PL intensities over time were acquired with a fiber coupled spectrometer (Ocean Optics Maya Pro 2000) that operates with a silicon photodetector array. Infrared sensitive spectra reported in Chapter 5 were recorded with a spectrograph coupled to a nitrogen cooled photomultiplier tube. The excitation source was provided by various lasers, specified for each experiment reported.

A software with a graphic interface was built using Python for communicating with the spectrometer and acquiring spectra and recording the emission of the samples over time.

Photoluminescence quantum yields (PLQY)

Relative PL quantum yield (PLQY) was obtained from the measured integrated PL at varying excitation intensities and plotted as:

$$RelativePLQY = \frac{I_{PL}}{I_{pump}} \tag{2.4}$$

Absolute values of PLQY were obtained from measurements performed in an integrating sphere (Labsphere). The wavelength dependent response of the system was calibrated using a certified tungsten lamp (Labsphere). Excitation was provided by CW diode lasers and spectra acquired through an optical fiber coupled from the sphere to a spectrometer (Ocean Optics Maya Pro 2000). PLQY values were calculated employing the method proposed by de Mello et al.[87], as

$$PLQY = \frac{P_c - (1 - A) \cdot P_b}{L_a \cdot A} \tag{2.5}$$

where L_a is the integrated intensity of the excitation light in the empty sphere, P_b is the integrated intensity of the diffuse PL when the sample is placed outside of the laser beam path and P_c is the intensity of the PL when the sample is directly hit by the laser. A is calculated as

$$A = 1 - \frac{L_c}{L_b} \tag{2.6}$$

where L_c and L_b is the integrated intensity of the excitation light when the sample is directly in or outside of the beam path, respectively.

2.2.3 Confocal microscopy

A home built microscope in confocal configuration allows for transmission and PL maps with sub-micrometer resolution and a maximum range of 50µm. The excitation source is provided by a supercontinuum laser (SuperK Extreme, NKT Photonics), and the output is tuned by an acousto-optic modulator (SuperK Select, NKT Photonics). The signal is collected in transmission geometry and focused into a fiber coupled to a photodiode and a Lock-in amplifier. The sample can be mounted in a nitrogen flow chamber and is scanned on a piezoelectric translation stage.

2.3 Time resolved Photoluminescence

Time-resolved PL measurements were performed using a femtosecond laser source and either a streak camera detection system (Hamamatsu C5680) or a Time Correlated Single Photon Counting (TCSPC) setup. Two femtosecond laser sources were used:

1. Unamplified tunable Ti:Sapphire laser (Coherent Chameleon Ultra II, temporal and spectral bandwidths of ∼140 fs and ∼5 nm, respectively), operating at 80 MHz. An acousto-optical modulating pulse picker (APE Pulse Select) was employed for controlling the repetition rate of excitation according to the lifetimes of the emission of the samples.

2. Q-switched Ti:Sapphire based regenerative amplifier (Coherent RegA 9000) operating at 250kHz seeded by a mode-locked Ti:Sapphire oscillator (Coherent Micra-18) operating at 80 MHz, providing pulses of ∼100 fs.

The photoluminescence is collected in reflection geometry, at a right angle from the excitation line and focused onto a spectrometer coupled to the detection system, which

can be either a Streak Camera or a TCSPC system.

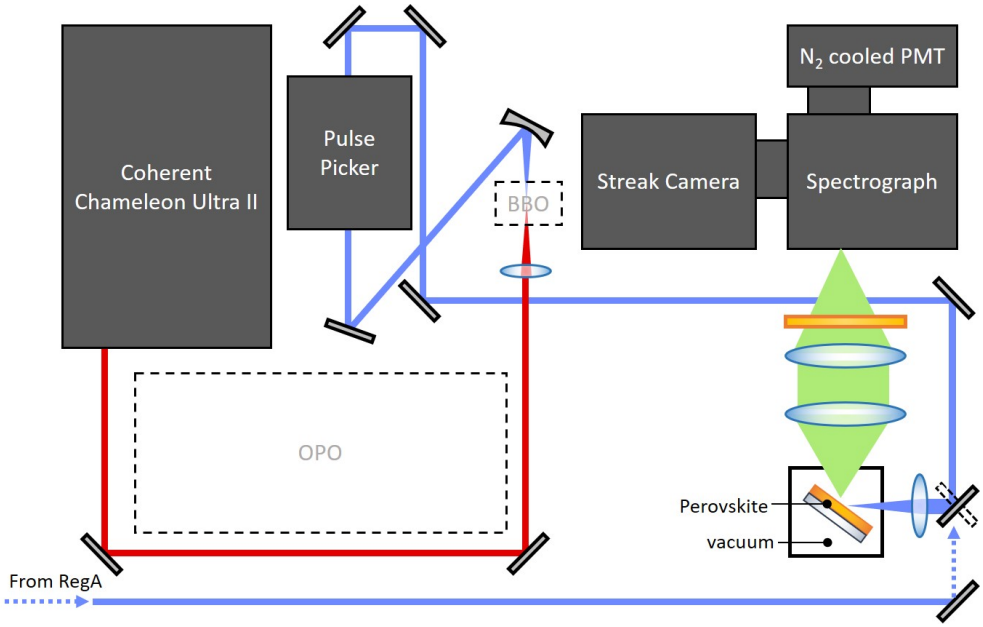

Figure 2.1: Simplified diagram of the experimental setup for time resolved PL experiments.

Time Correlated Single Photon Counting (TCSPC)

The principle of TCSPC is the repetitive illumination of the sample with a pulsed laser and the detection of a single photon for each pulse of excitation. The delay times between the detected photon and the reference signal is measured electronically and the photon counts as a function of time delay build up a histogram of the PL decay. To achieve reliable counting, the intensity of the detected signal must be attenuated so that the rate of detected photons per excitation pulse is kept below 5%.

For TCSPC measurements performed in this work, the detection system was a InGaAs photodiode coupled to a nitrogen cooled photomultiplier tube, and the time correlated counting provides a time resolution of ~ 1 ns.

Streak camera detection

For better time resolution and sensitive detection in the visible (400 - 800 nm) region, a Streak Camera (Hamamatsu C5680) was used. The principle of a Streak Camera

is the conversion of light into electrons and the time dependent spatial deflection of these electrons. After wavelength dispersion by the spectrograph, the collected light is focused onto the photocathode of the streak tube and converted into a number of electrons proportional to the intensity of the light. The electrons are accelerated against a phosphor screen. During acceleration, a variable voltage is applied, deflecting the electrons at angles according to the time of arrival. The image on the phosphor screen is taken by a CCD camera, with the temporal dispersion on the y axis and the wavelength dispersion on the x axis.

The electron deflection can be obtained with either a linear voltage sweep module, resulting in time resolution of up to ∼300 ps, or with a high speed sinusoidal voltage module that provides time resolution up to 2 ps.

2.4 Transient Absorption

Transient absorption (TA) dynamics can be measured in the so called pump-probe configuration. In this type of technique, the sample is excited by a short laser pulse and probed by a second short pulse that arrived with a certain time delay with respect to the excitation. The changes to the probe beam induced by the photoexcitation can be time resolved by scanning the time delay between the pulses, with a maximum time resolution that is determined by the pulse duration.

In the experiments reported in this thesis we use TA spectroscopy to obtain the dynamics of the excited state of the semiconductor by measuring the decay of the photo-bleach that results from the photo-excitation.

Experimental setup

An amplified Ti:sapphire laser (Quantronix Integra-C) generates pulses of $\sim$ 100 fs centered at 800 nm. A broadband white light probe is generated by focusing the pulses into a thin sapphire plate. The fundamental output from the amplifier can be converted to 400 nm by Second Harmonic Generation (SHG) or alternative wavelengths in a Non-linear Optical Parametric Amplifier (NOPA). The pump beam is spatially delayed with a mechanical stage providing temporal resolution of $\sim$ 150 fs and range of 1 ns. Alternatively, longer time range can be achieved with pump light provided by a Q-switched Nd:YVO_4 laser (Innolas Picolo) which is electronically triggered and synchronised to the Ti:sapphire laser via an electronic delay. The pump pulses have a width of ∼700 ps

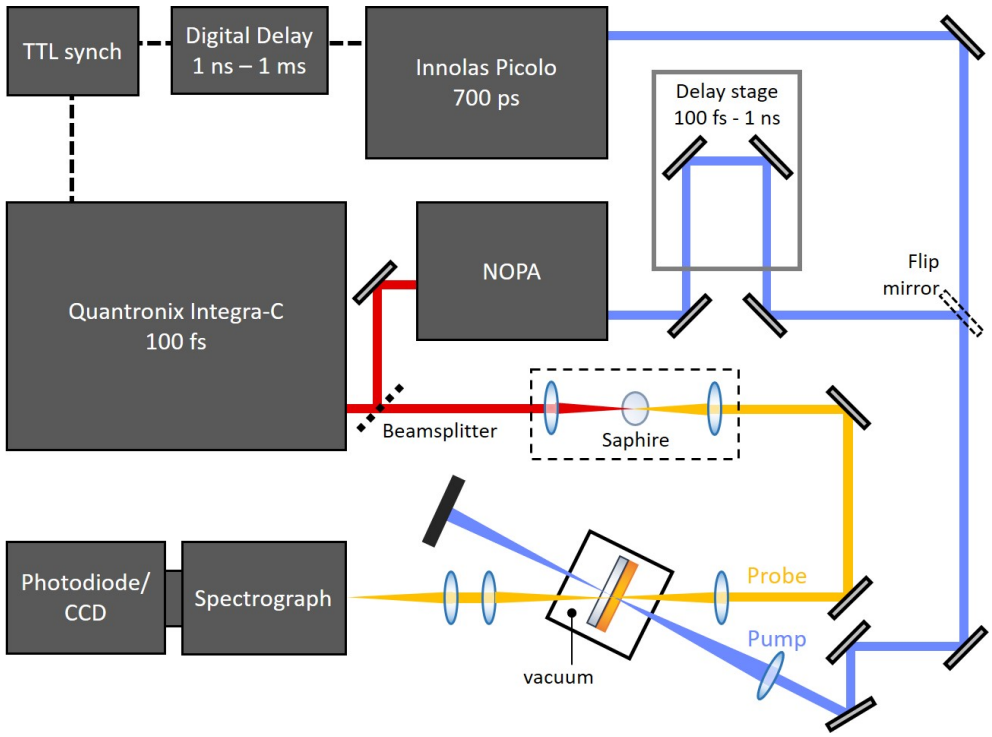

Figure 2.2: Simplified diagram of the experimental setup used for Transient Absorption.

FWHM. Including jitter, and the system has a combined time resolution and jitter of approximately 200 ps. After interaction with the sample, a home-built prism spectrometer disperses the probe light on to a fast CCD array, enabling broadband shot-to-shot detection.

In the measurements presented in this thesis the TA dynamics were obtained using the Q-switched Nd:YVO_4 laser in order to measure the long lifetimes of the carriers in the range up to 1 ms. The excitation wavelength was 532 nm (obtained by SHG of the fundamental output of the Nd:YVO4 laser) for $MAPbI_3$ samples and 355 nm (obtained by Third Harmonic Generation) for $MAPbBr_3$ samples.

2.5 Atmosphere and temperature control

The experiments reported in this work required careful control of the atmosphere and temperature to which the samples were exposed. Measurements in vacuum were performed under active pumping and pressure bellow 10^{-5} mbar. Dry atmosphere was obtained from a cylinder of dry air (Nordival, purity 5.5). Temperature control was achieved using liquid nitrogen and a cold finger cryostat (Oxford Instruments), where the sample is kept in vacuum (pressure bellow 10^{-5} mbar).

3

Nature of defects and their role in recombination dynamics

The high density of defects that is inherent to solution processed materials doesn't seem to impose a strong restriction to the efficiency achieved from metal halide perovskite devices. The native carrier trapping sites present in these materials have been a matter of discussion in the field, and how they affect the dynamics of charge carriers may be related to some of the unusual characteristics of metal halide semiconductors and their impressive performance. This Chapter investigates the nature of the defects in these materials and their impact on the carrier dynamics, combining spectroscopic measurements with theoretical predictions. The contents of Section 3.1 have been adapted from Meggiolaro et al. (2018).*

3.1 Defects in $MAPbI_3$

Defect tolerance in semiconductors is usually understood as either a low density of defects reuslting from high defect formation energies (DFE) or as the low impact of the presence of defects on the carrier diffusion lengths and lifetimes[89]. It has been indicated

*[88] Meggiolaro, D. et al. "Iodine chemistry determines the defect tolerance of lead-halide perovskites". *Energy & Environmental Science*, 11, 3, pp. 702–713. (2018)

by several studies that native defects in $MAPbI_3$ would introduce only shallow states, explaining their low impact on performance[59,90,91].

Adinolfi et al. reported a distribution of bulk trap states in $MAPbI_3$ (single crystal) reaching energy levels around 0.2–0.3 eV above the valence band (VB) and below the conduction band (CB)[92]. Several groups have carried out first-principles investigations on the nature of the defects that originate these trap states[59,90,91,93,94], and seem to agree on the predominance of shallow states. On the other hand, the presence of deep traps formed by iodine interstitials has also been reported[95]. In this Section it is briefly discussed the identification of defects in $MAPbI_3$ by first-principles calculations. Associated to the results of the computational studies, the impact of such defects on the carrier dynamics is investigated by spectroscopic measurements.

3.1.1 The role of Iodine oxidation state in carrier trapping

First-principles calculations were performed by Dr. Daniele Meggiolaro and Prof. Filippo de Angelis from CNR-ISTM in Perugia, Italy. The density and properties of native defects were predicted using large supercell calculations, based on hybrid DFT, including dispersion corrections and spin–orbit coupling.

Figure 3.1 shows the DFE diagram versus the Fermi energy for $MAPbI_3$ showing the most stable defects in stoichiometric conditions. Solid lines indicate the stable charge states of a given defect, while the blue dashed lines indicate the metastable neutral state of I_i. The energy of positive defects increases by increasing E_F while the energy of negative defects decreases, and that of neutral defects is stable with respect to E_F. E_F ranges from the top of the valence band (E_F=0) to the bottom of the conduction band (E_F=1.58 eV). The native Fermi level is indicated by the vertical black dashed line at 0.65 eV. The thermodynamic ionization levels are determined by the crossing of the lines representing different charge states of a given defect in Figure 3.1a. Figure 3.1b shows the thermodynamic ionization levels for the most stable defects represented in Figure 3.1a, referenced to E_F=0.

It was found that despite the high density expected of Pb- and MA-related defects, only V_{Pb} and I_i exhibit charge transitions within the band gap, making these defects possible carrier trapping sites. However, due to small capture cross-sections and high activation energies, the trapping activity of V_{Pb} is strongly quenched.[88] This indicates that interstitial iodine is the only stable and active trap source among native point

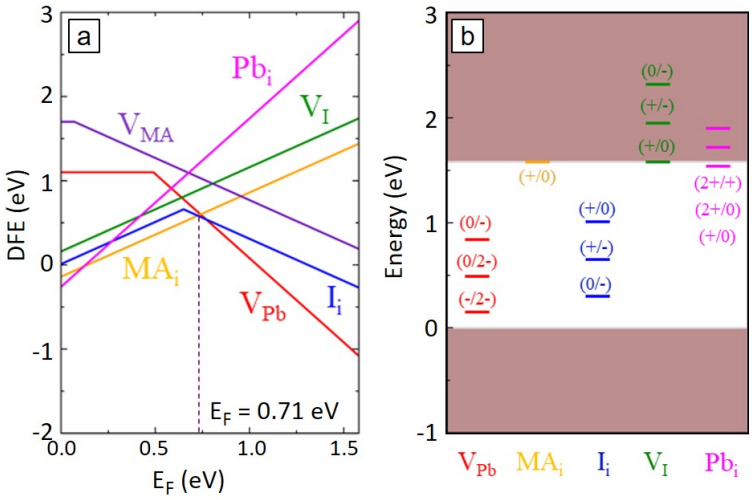

Figure 3.1: a) Defect formation energy (DFE) diagram versus the Fermi energy (E_F) for $MAPbI_3$ showing the most stable defects in stoichiometric (iodine-medium) conditions; b) Thermodynamic ionization levels for the most stable defects calculated in a) referenced to the VB corresponding to E_F=0. Data provided by Dr. Daniele Meggiolaro and Prof. Filippo de Angelis. Adapted from: [88]

defects. However, it results from the redox chemistry of iodine that these interstitials are amphoteric sites which can trap electrons through the $+/0$ ionization level placed at 0.57 below the CB edge and holes through the $0/-$ level at 0.29 eV below the VB.

3.1.2 Lattice deformation and slow electron detrapping

Having established that interstitial iodine is the most relevant trapping site in $MAPbI_3$, the properties of this defect were studied.

Figure 3.2 shows the calculated most stable geometrical structures of interstitial iodine in its positive (a), neutral (b) and negative (c) charge states, and their respective I-I distances. Relevant iodine atoms involved in the trapping/detrapping processes are highlighted in yellow. For I_i^+ the average of the two I-I bond lengths is reported. The energy versus structural coordinates of I_i versus the root mean square displacement (RMSD) of the relevant iodine atoms with respect to their position in I_i^+. The energies for the positive species are referenced to the VB maximum, while those of the negative species are referred to the CB minimum, simulating the energetics after photoexcitation

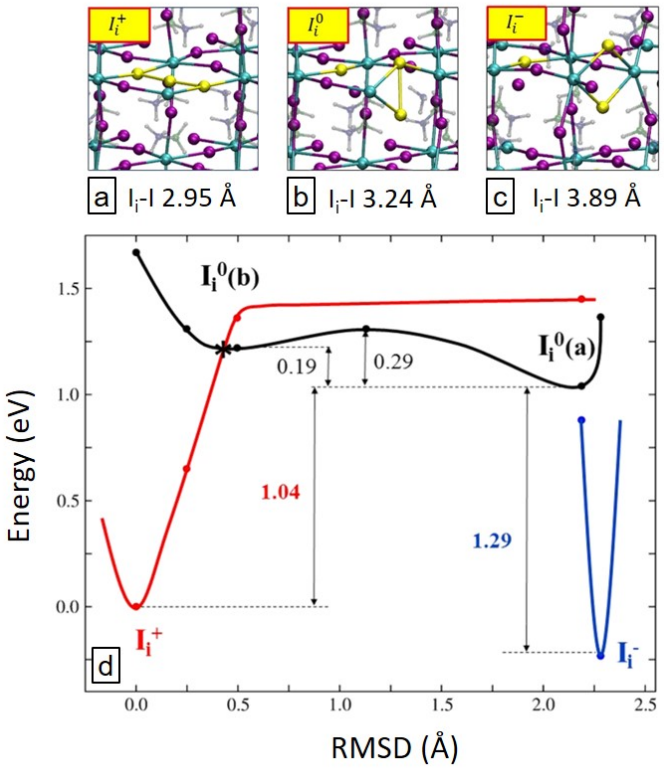

Figure 3.2: a) Local geometrical structures of interstitial iodine in its positive (a), neutral (b) and negative (c) charge states. d) Configuration diagrams of interstitial iodine in its positive (red), neutral (black) and negative (blue) charge states versus the root mean square displacement (RMSD) of the highlighted iodine atoms with respect to their position in I_i^+. Data provided by Dr. Daniele Meggiolaro and Prof. Filippo de Angelis. Adapted from: [88]

(before recombination). The separate positive/neutral and negative/neutral energies have the same reference, thus they can be compared, while the positive/negative energies cannot be directly compared. The points are calculated values while the solid lines are an interpolation to guide to the eye.

According to the model proposed, hole trapping by I_i is associated with a very small geometrical rearrangement and no energy barriers. Therefore, hole trapping, detrapping and trap-assited recombination is expected to be relatively fast, characterizing a possibly efficient deactivation channel for photogenerated charge carriers. Electron trapping by I_i^+ results in a rearrangement of the lattice through a small energy barrier, and release

of the trapped carrier by thermal activation or trap-assited recombination requires a significantly larger barrier to be overcome. Consequently, the lifetimes of trapped electrons are expected to be very long, in agreement to the trapping and recombination dynamics reported by Leijtens et al.[54]

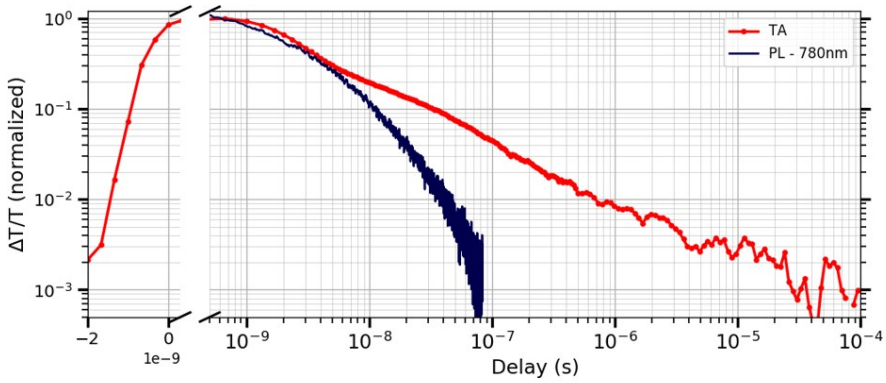

Figure 3.3: PL dynamics (dark blue) corresponding to the integrated band-edge emission centered at 780 nm, and the Transient Absorption dynamics (red) probed at the photo-bleach band at 770 nm, of a $MAPbI_3$ thin film

Combined with the calculations, the recombination dynamics of $MAPbI_3$ were investigated by photoluminescence (PL) and Transient Absorption (TA). Figure 3.3 shows the TA dynamics of a $MAPbI_3$ thin film probed at the peak of the photo-bleach at 770 nm and PL dynamics of the band-edge emission measured at similar illumination conditions. It was observed that the photo-bleach (PB) dynamics has two components, a short living decay and a very long one of tens of microseconds, which has no emissive analogue, thus corresponding to a non-radiative decay process.

Figure 3.4 shows the PL decays taken at different excitation densities and temperatures. The decays at the lowest excitation density show one fast component that can be assigned to trapping dynamics and a long tail[96]. The recombination at the lower excitation densities are strongly dependent on the trapping behavior, so they were compared as a function of temperature, as shown in Figure 3.5a. A gradual change could be noticed in the relative contribution of the two components. The temperature dependence of the TA dynamics (Figure 3.5b) shows a similar trend. Despite being taken at high excitation intensities, TA is more sensitive to the population of the non-emissive states. The relative contribution of the fast and slow components to the TA signal were compared, and it was observed that while the fast component decreases

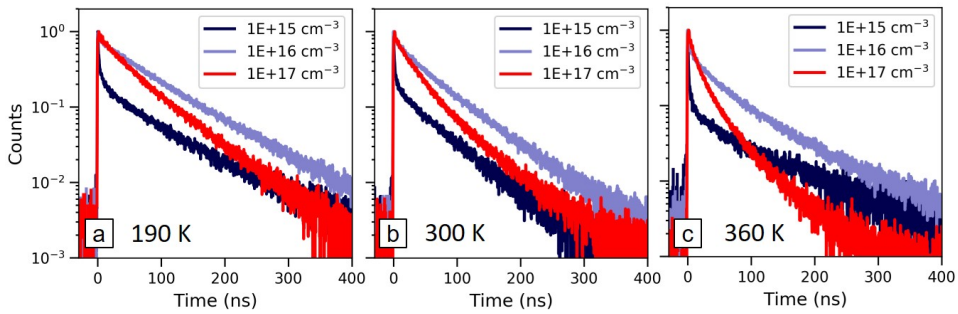

Figure 3.4: PL dynamics of a $MAPbI_3$ thin film at different excitation intensities at a) 190 K, b) 300 K and c) 360 K.

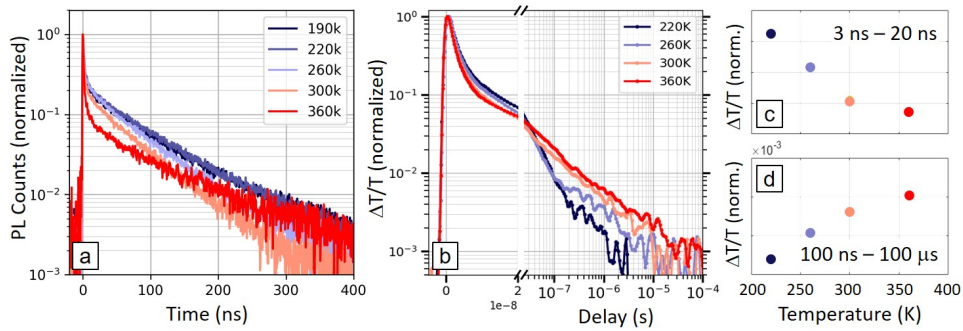

Figure 3.5: PL dynamics of a $MAPbI_3$ thin film at different temperatures; b) TA dynamics of $MAPbI_3$ at different temperatures; c) $\Delta T/T$ of the fast component and d) $\Delta T/T$ of the long lifetime component as a function of temperature. TA dynamics measured by Dr. Alex Barker

with increasing temperature (Figure 3.5c), the signal corresponding to the slow component increases. The intensity of the PB observed is related to the population of the corresponding electronic states, in this case, the free carriers at the band-edge. The presence of trapped carriers result in remaining free carriers of the opposite charge. The long component observed in the TA dynamics corresponds then to the remaining free carriers that slowly recombine non-radiatively with the trapped carriers. It can then be inferred that the the population of long living trapped carriers is increasing with temperature, suggesting the presence of an energy barrier to its formation. This slow component can be assigned to the recombination of electrons trapped by positive interstitial iodine with free holes in the VB.

This slow decay of trapped electrons is consistent with the activation energy required

to restore the lattice geometry upon change of the charge state of the defect, according to the configuration diagram of Figure 3.2d.

3.2 Defects in $MAPbBr_3$

In the previous Section it was presented the theoretical predictions of the defect properties in $MAPbI_3$ and its implications on carrier dynamics, which was supported by experimental TA and PL dynamics. $MAPbBr_3$ is expected to have a similar defect chemistry (as shown by the DFE diagram and thermodynamic ionization levels in Figure 3.6).

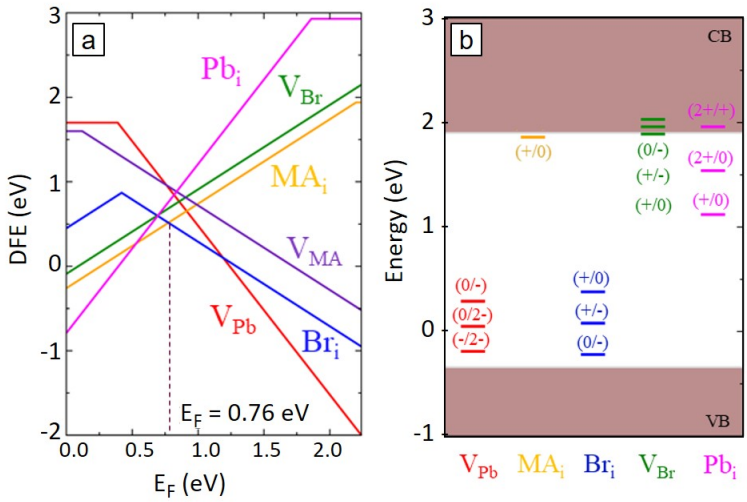

Figure 3.6: a) Defect formation energy (DFE) diagram versus the Fermi energy (E_F) for $MAPbBr_3$ showing the most stable defects in stoichiometric conditions; b) Thermodynamic ionization levels for the most stable defects calculated in a) referenced to the VB corresponding to E_F=0. Data provided by Dr. Daniele Meggiolaro and Prof. Filippo de Angelis. Adapted from: [97]

To study the case of $MAPbBr_3$, one additional tool can be explored: the emission associated with defects, that, as the following Section will show, can provide direct insight into the trap states of the semiconductor.

3.2.1 Emissive trap states

Photoexcitation of lead halide perovskites can induce several transformations in the material, as was briefly discussed in Section 1.2.2. In particular, under certain conditions it can be observed a quenching of the PL emission, related to the formation of defects due to ion migration.

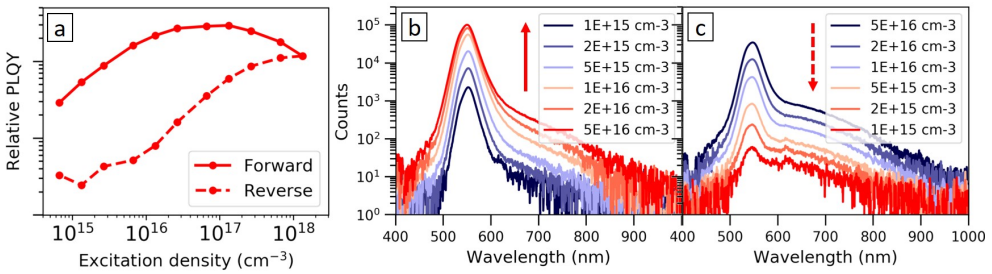

Figure 3.7: a) Relative PLQY curves of a $MAPbBr_3$ thin film taken in vacuum with increasing (solid lines) or decreasing (dashed lines) excitation densities (Adapted from: [98]); PL spectra b) before and after the intensity cycle, and a) with increasing and b) decreasing excitation intensity.

Figure 3.7a shows the relative PLQY of a $MAPbBr_3$ thin film taken with increasing and decreasing excitation density, where a strong hysteresis can be observed. This effect indicates increase of the density of trap states, and it will be investigated in more detail in Chapter 4. The PL spectrum was monitored during this experiment, as shown in Figure 3.7. When plotting the spectra on a semilog scale, the low intensity tail of the PL emission can be seen. When measuring in the reverse order, it could be observed that this tail is enhanced, becoming a broad emission band centered around 700 nm.

In order to obtain more information concerning the subgap emission, an infrared sensitive detector was used, and the spectra were measured in separate windows using the appropriate filters to remove artifacts such as pump scatter and the multiple orders of diffraction from the spectrometer. Surprisingly, a second broad emission band was found in the near infrared region, centered around 1000 nm. These two bands (SG-vis, the subgap band centered around 700 nm and SG-ir, the near-infrared band centered around 1000 nm) have distinct origins, as indicated by their opposite behavior after prolonged exposure to light, which is associated with the quench of the band-edge PLQY. While the SG-vis band increases in intensity, the SG-ir band is simultaneously quenched. Both bands presented the particular bahavior of trap state emission, that is, while the band-edge PLQY increases with excitation intensity, the emission efficiency

of these subgap states decreases, due to a saturation effect.

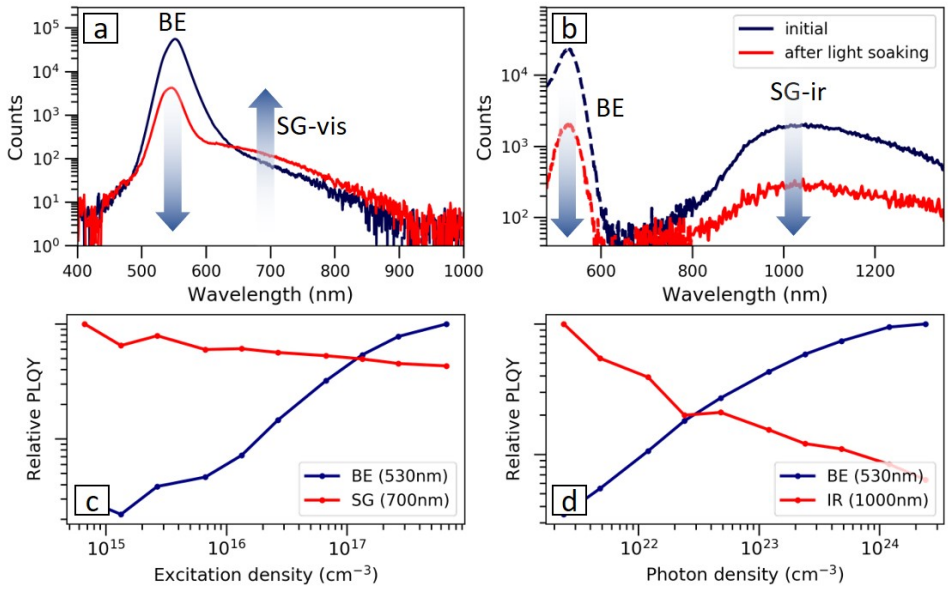

Figure 3.8: PL spectra of a $MAPbBr_3$ thin film taken with a) a detector sensitive to visible light and b) an infrared sensitive (spectral response not calibrated, so the relative intensity should not be compared); Relative PLQY of the band edge (BE) emission compared to the emission taken c) at 700 nm (SG-vis band), as a function of excitation density using a pulsed laser, and d) at 1000 nm (SG-ir band), as a function of photon density using a CW laser.

Because of the limited spectral response of the detectors, capturing both SG-vis and SG-ir emissions in the same measurement could only be achieved at low temperature, when these bands can be seen with higher intensity.[99] The relative intensity of these bands was compared in two different cases, as shown in Figure 3.9. The first case was a $MAPbBr_3$ thin film on glass, coated with PMMA and measured on the substrate side. As shown in Figure 3.9b, both the band-edge emission and SG-ir emission decreased with increasing temperature, as expected in these materials. The SG-vis emission couldn't be observed even at low temperature. The second case was a bare film measured on the perovskite side. Both samples were measured under high vacuum, so one could expect the naked surface of the perovskite to be more defective. In this case both SG-vis and SG-ir bands were seen, and the intensity of the SG-ir band appears to be slightly quenched in the presence of the SG-vis band.

This observation, combined with the opposite behaviors demonstrated in Figure

3.8a-b, indicates that the two bands correspond to competing recombination paths, and the SG-vis band is associated with a more effective recombination channel. That is, the presence of the SG-vis band seem to be associated with higher losses and lower intensity of the band-edge PL. Furthermore, the lower intensity of SG-ir in the presence of SG-vis is consistent with higher the rates for carrier capture in the trap state associated with the SG-vis band, which would limit the carrier capture originating the SG-ir emission.

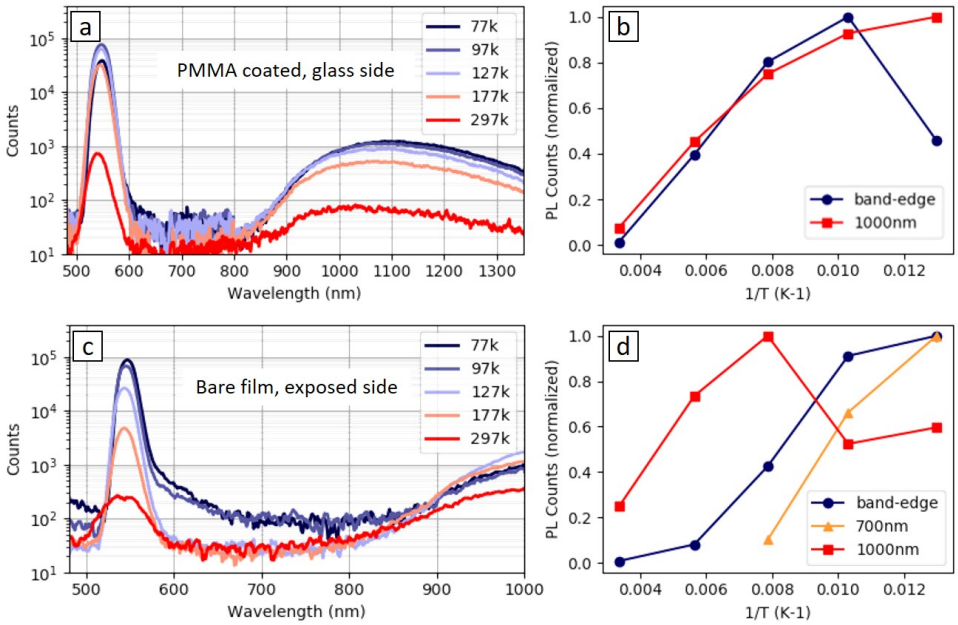

Figure 3.9: a) PL spectra at different temperatures of a $MAPbBr_3$ film coated with PMMA, measured on the glass side; b) Relative PL intensity as a function of temperature for different regions of the spectrum; c) PL spectra at different temperatures of a bare $MAPbBr_3$ film measured on the exposed side; d) Relative PL intensity over temperature for the bare film.

3.2.2 Origins of the subgap emission

To help identifying the nature of the defects that correspond to these subgap bands, perovskite films were compared coated with different charge extraction layers. The samples compared were $MAPbBr_3$ thin films prepared with identical procedures but coated with either a layer of PCBM, that is an electron extracting layer, or Spiro-OMeTAD, that is a hole extracting layer, or with PMMA, that is an inert insulating polymer and

should not significantly affect the semiconductor. First, the relative intensity of the band-edge emission was evaluated, as shown in Figure 3.10a.

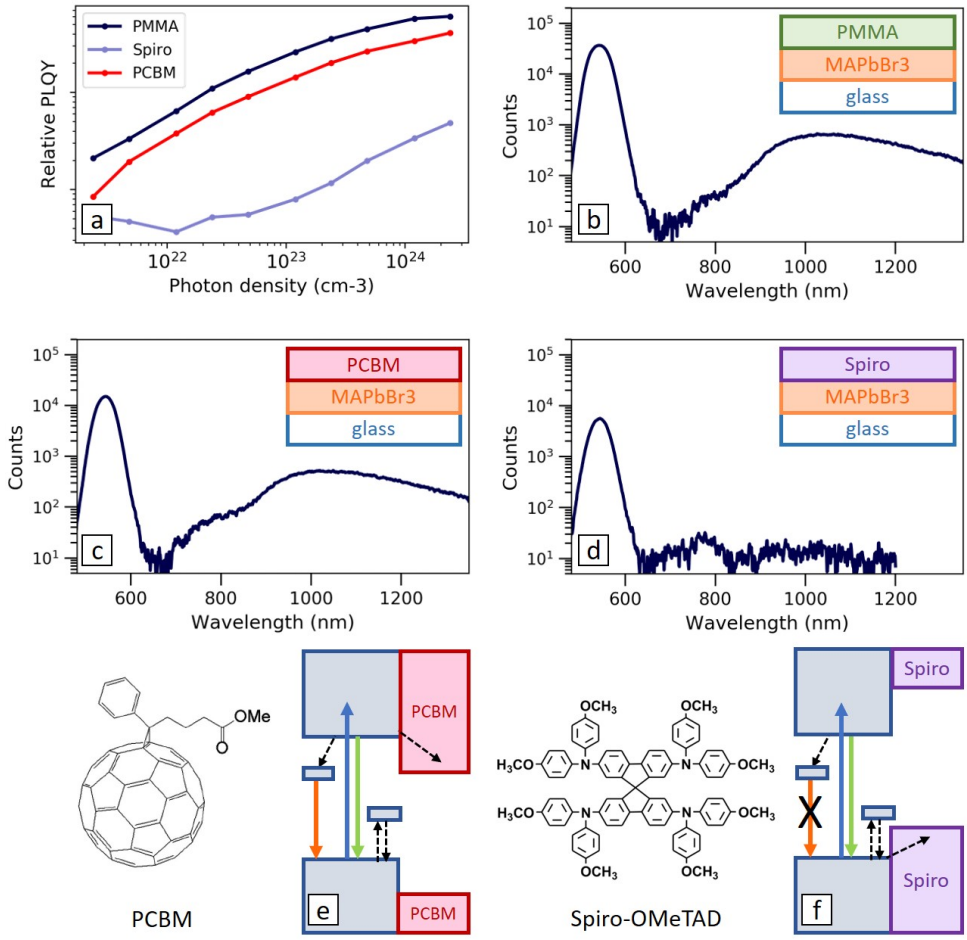

Figure 3.10: a) Relative PLQY of a $MAPbBr_3$ thin film coated PMMA, PCBM or Spiro-OMeTAD; PL spectra of $MAPbBr_3$ coated with b) PMMA, c) PCBM and d) Spiro-OMeTAD; Band diagram illustrating the band alignment and charge transfer between the perovskite layer and PCBM (e) or Spiro-OMeTAD (f).

Both the PCBM and Spiro-OMeTAD coated samples showed lower PL intensity, as it would be expected in the presence of charge extraction. This effect was however much more dramatic in the perovskite film coated with Spiro-OMeTAD. A similar trend was observed by Leijtens et al. in the photocurrent measurements performed in

$MAPbI_3$ thin films coated with PMMA, PCBM or Spiro-OMeTAD[54], and was reported as an indication of majority electron trapping in the perovskite layer. The PL spectra of these samples were then compared. The excitation source used was a laser with wavelength of 400 nm. Since both PCBM and Spiro-OMeTAD absorb the 400 nm light, the measurements were performed on the substrate side of the samples, so as to directly photoexcite the perovskite layer. Figure 3.10b shows the PL spectrum of a film coated with PMMA, Figure 3.10c shows the spectrum obtained at analogous experimental conditions from a perovskite film coated with PCBM, and Figure 3.10d shows the spectrum from a sample coated with a Spiro-OMeTAD layer. The SG-ir emission is seen for both the PMMA and PCBM coated perovskite, but it's strongly quenched in the Spiro-OMeTAD coated film. Following the observations of Leijtens et al.[54] and considering the photoexcitation is performed on the substrate side of the perovskite film, it can be considered that trapping occurs in a faster timescale than the carrier transfer to the extraction layer. Thus in the case of PCBM, part of the photoexcited electrons should be trapped in the perovskite film and part would be extracted, and the presence of the PCBM layer would not affect the observations of electron traps (as illustrated in Figure 3.10e). For the perovskite coated with Spiro-OMeTAD, on the other hand, the trapped electrons would have very low recombination rates, as the free holes would be extracted (as illustrated in Figure 3.10f). Therefore the SG-ir emission can be associated with electron trapping defects.

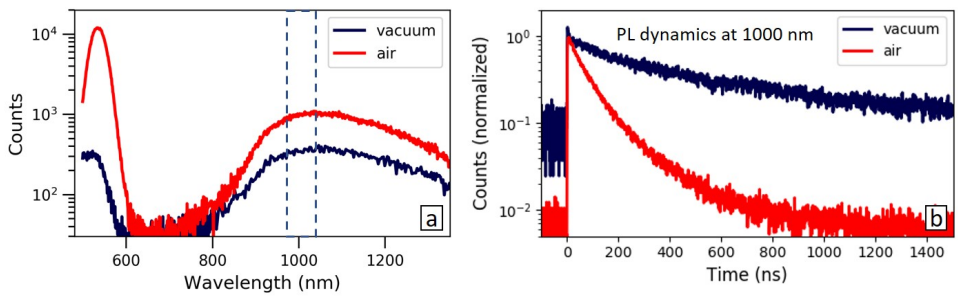

Figure 3.11: a) PL spectra and b) PL dynamics at 1000 nm of a $MAPbBr_3$ thin film in high vacuum (dark blue) or after exposure to air (red).

Another interesting observation regarding the nature of these defects is how they react to the atmosphere. The behavior of the emission was monitored when a film kept in high vacuum is exposed to air. As shown in Figure 3.11a, the intensity of the band

edge PL increases under air exposure, which is consistent to previous reports of defect passivation by oxygen[76,77]. These effects will be discussed in more detail in Chapter 5. Interestingly, the intensity of the SG-ir emission is also enhanced, indicating that this emission is not associated with the defects that are passivated. The passivation most likely occurs on other trap states, which are likely more efficient non-radiative recombination centers. This is consistent with the oxygen passivation of hole traps as reported in the literature[100] and to our assignment of the SG-ir emission to electron trapping defects. The lifetime of the SG-ir emission after exposure to air, as shown in Figure 3.11b, becomes shorter, contrary to what is observed on the band edge lifetimes due to defect passivation (as will be further discussed in Chapter 5). This could be related to a higher density of free holes that accelerates the recombination of trapped electrons.

3.2.3 Carrier trapping and recombination dynamics

The dynamics of these subgap emissions were then investigated. Figure 3.12 shows the TA dynamics of a $MAPbBr_3$ thin film probed at the peak of the PB at 525 nm. In a similar way to the dynamics obtained from $MAPbI_3$ (Figure 3.3), a very long component can be seen extending to several microseconds. As discussed in Section 3.1.2, the PB at the band edge is related to the population of free photoexcited carriers and can also reflect the population of trap states when a majority of one species is trapped resulting in remaining free carriers of opposite charge. The band-edge PL dynamics taken from the same sample at similar illumination conditions is very similar in scale to the faster component in the TA decay, stretching for a few nanoseconds. Interestingly, both SG-vis and SG-ir emissions showed longer lifetimes, and while the PL dynamics probed at 700 nm (SG-vis) was still close to the band-edge lifetimes, the emission at 1000 nm (SG-ir) was found to be much longer, decaying on a microsecond scale.

Finally, the temperature dependence on the dynamics of the SG-ir emission were investigated. Figure 3.13a shows the PL dynamics of the SG-ir emission taken at 1000 nm at different temperatures. The sample was kept under illumination at room temperature for several minutes to avoid effects of photoinstabilities and then cooled down to 77K. Each decay was fitted with a stretched exponential and the lifetimes were used to fit the Arrhenius equation:

$$k = \frac{1}{\tau} = A \cdot e^{-Ea/(k_B \cdot T)} \tag{3.1}$$

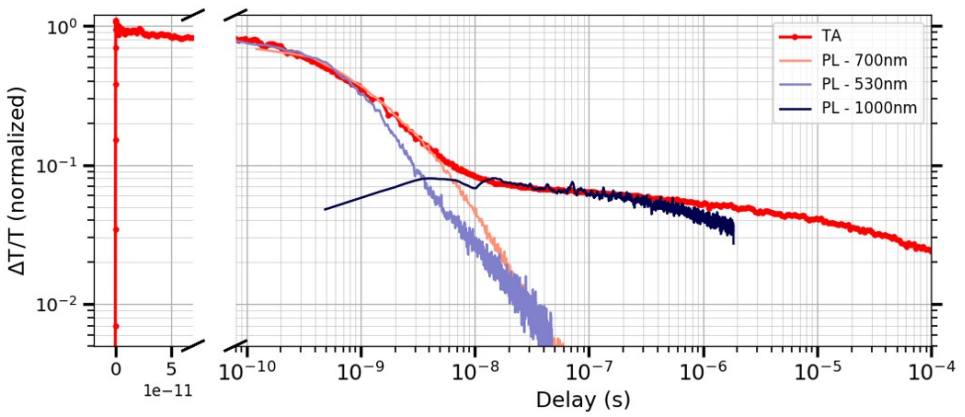

Figure 3.12: PL dynamics (light blue) corresponding to the integrated band-edge emission centered at 530 nm, subgap emission dynamics taken at 700 nm (orange) and 1000 nm (dark blue), and the Transient Absorption dynamics (red) probed at the photo-bleach band at 525 nm, of a $MAPbBr_3$ thin film

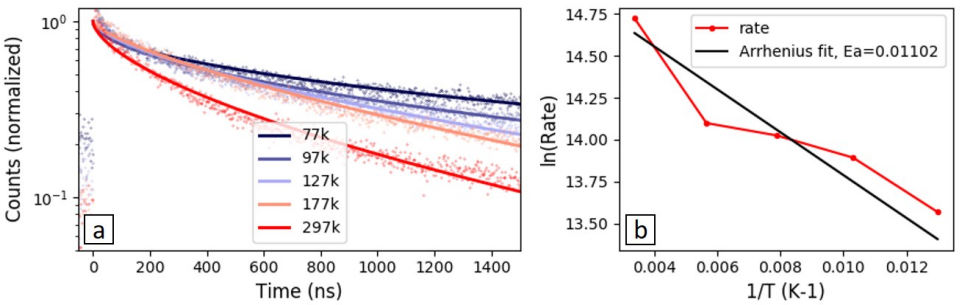

Figure 3.13: a) PL dynamics of the emission at 1000 nm from a $MAPbBr_3$ thin film at different temperatures, each of them fitted with a stretched exponential, and Arrhenius plot of the temperature dependence of the rates.

where k is the decay rate, τ is the PL lifetime, k_B is the Boltzmann constant[†], T is the temperature, A is the pre-exponential factor and Ea is the activation energy.

The values obtained for activation energy for the trapped electron recombination as shown in Figure 3.13 are much lower than the theoretical predictions, however, as discussed previously, both the trapping process and the release of a trapped carrier (by thermal activation or trap-assisted recombination) involve an energy barrier, which

[†] $k_B = 8.6173303 \cdot 10^{-5} eV \cdot K^{-1}$

means that trapping rates will probably also be affected by the temperature of the system. Therefore the populations of the trap states might also be varying. Nonetheless, the temperature dependence of the SG-ir emission lifetimes is an indication of the presence of this energy barrier, which is consistent with the lattice geometrical rearrangement, as discussed previously.

3.3 Defect tolerance as a consequence of trapping dynamics

The low rates for recombination of trapped carriers can have an interesting effect on the semiconductor efficiency. This Section demonstrates a qualitative model that takes into account the different types of traps that can be present in the material, and investigate how the trapping dynamics affect the steady state radiative efficiency. The system of rate equations described in Section 1.3.2 can be adapted to include two types of traps:

$$\frac{dn_e}{dt} = G - \beta_{rad} n_e n_h - k_{te} n_e (N_{te} - n_{te}) - R_{th} n_e n_{th} - \gamma n_e n_h^2 \tag{3.2}$$

$$\frac{dn_h}{dt} = G - \beta_r a d n_e n_h - k_{th} n_e (N_{th} - n_{th}) - R_{te} n_h n_{te} - \gamma n_e n_h^2 + G_{up} n_{th} \tag{3.3}$$

$$\frac{dn_{te}}{dt} = k_{te} n_e (N_{te} - n_{te}) - R_{te} n_h n_{te} \tag{3.4}$$

$$\frac{dn_{th}}{dt} = k_{th} n_h (N_{th} - n_{th}) - R_{th} n_e n_{th} - G_{up} n_{th} \tag{3.5}$$

where N_{te} is the density of electron traps and N_{th} is the density of hole traps. n_{te} and n_{th} are the density of trapped electron and holes, k_{te} and k_{th} are the trapping rates and R_{te} and R_{th} are the rates of recombination of a trapped carrier with its counterpart.

In a simplification of the model it is considered that release of a trapped carrier only occurs when it recombines with a free carrier of opposite charge, considering this is more likely to occur than thermal activation of the trapped carrier back to the CB or VB. This means that, when including the two types of traps, part of the carriers will be permanently trapped without a recombination channel available. To circumvent that, it was considered an additional term for a trapped carrier to be released as a free carrier, with a rate G_{up}. Based on the theoretical predictions presented in the previous

Sections, electron trapping is associated with a lattice distortion, therefore one expects lower rates for electron trapping and detrapping compared to holes. For the sake of simplification of the model, it is considered that due to the lower energy barriers for detrapping, only holes have a significant rate of release as a free carrier (G_{up}).

Given the number of free parameters in this altered version of the model, finding accurate values from experimental data is impractical. One can however simulate the expected outcome using tentative values for the rates and densities that are similar to the values found in fits of the simplified model. The PLQY as:

$$PLQY = \frac{n_{PL}}{n} = \frac{\beta_{rad} n_e n_h}{n} \tag{3.6}$$

where n is the excitation density and n_{PL} is the total emitted photons, obtained by the integrated radiative decay.

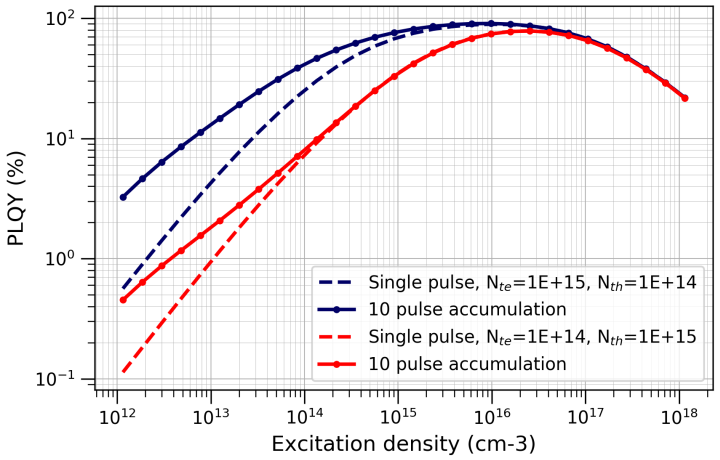

Figure 3.14: Simulated PLQY for $N_{te} > N_{th}$ (dark blue) and $N_{te} < N_{th}$ (red), where N_{te} is the density of electron traps and N_{th} the density of hole traps. Dashed lines are obtained from a single pulse calculation, while the solid lines are obtained after a 10 pulse accumulation.

Figure 3.14 shows the simulated PLQY as a function of excitation density, obtained from Equation 3.6 and calculated from the carrier dynamics resulting from the Equations 3.2-3.5. The curve in red is simulated with a higher density of hole traps, while the curve in blue is simulated with a higher density of electron traps. In the example illustrated here, the excitation is pulsed, with a repetition rate of the laser of 250 kHz,

which is similar to the conditions of most of the experimental data presented in this Chapter. Given the long lifetimes of trapped carriers, the pulse pile up must be taken into account, so the remaining populations at 4 μs after the first pulse simulated are used as initial conditions for the next pulse arrival. This results in a trap filling effect. Dashed lines in Figure 3.14 represent the values obtained from a single pulse calculation, while the solid lines are obtained after a 10 pulse accumulation. From the four curves, it can be observed that:

1. The lower trapping rates of electron trapping defects make them a less efficient recombination center than hole traps, resulting in a shift of the trap filling region of the PLQY rise with excitation intensity.

2. The longer lifetimes of trapped carriers result in a slow trap filling under illumination, reducing the effective trap density.

Both of these effects result in lower non-radiative losses and higher radiative efficiencies in the low excitation intensity regime, which is the relevant regime for solar cell operation.

As the computational results presented in Section 3.1.1 are supported by the spectroscopic experiments, one interesting conclusion taken from it is that both electron and hole traps considered in this model are interstitial halogens. The amphoteric nature of these traps suggests that the fabrication conditions can favor the formation of either. Thus, under oxidizing conditions, hole traps can be converted into less detrimental electron traps, improving the efficiency of the semiconductor.

3.4 Chapter conclusions

The results presented in this Chapter reveal fundamental properties of trap states in lead halide perovskites. The agreement between optical spectroscopy measurements with the computational studies provides a consistent framework for understanding of defects activity in these semiconductors. The conclusions taken from the first-principle calculations can be summarized in two points:

1. Interstitial halogen (I_i or Br_i) are the most relevant carrier trapping sites, and can act as either electron or hole traps, depending on their oxidation state.

2. Electron trapping is associated with a distortion of the lattice. This results in an energy barrier for carrier trapping and detrapping and therefore low rates for both processes.

The computational studies were supported by experimental data that demonstrate the presence of long living electron traps in both $MAPbI_3$ and $MAPbBr_3$. The discovery of emissive trap states in $MAPbBr_3$ is particularly important, as it allows to directly probe the presence and dynamics of trapping sites. It also helps understanding the mechanisms behind photoinstabilities commonly observed in the radiative efficiency of the material.

Understanding these fundamental characteristics of the semiconductor is very promising for device applications, as it provides an insight into potential improvements of fabrication methods. The amphoteric nature of interstitial defects and their capability of trapping electron or holes according to the oxidation state implies that the formation of less detrimental trap states can be favored by controlling the oxidizing conditions during and after the film fabrication.

4

Photoinduced healing and formation of defects

This Chapter will focus on reversible photoinduced changes observed in perovskite properties. In particular, these studies try to disentagle the conflicting reports in literature regarding PL bahavior. PL quenching has been observed from lead halide perovskite thin films of different compositions as a result of a photoinduced trap formation in inert atmosphere. On the other hand, previous reports showed instead an enhancement of PL under illumination, and a self-healing mechanism was proposed. These instabilities have been a challenge for reliable device application and to the understanding of the material. This Chapter investigates the factors that regulate these effects and possible mechanisms, aiming to consolidate these conflicting reports. The contents of this Chapter have been adapted from Motti et al. (2018).*

4.1 Ion migration in perovskites

One very clear example of photoinduced changes observed in perovskites is the case of mixed halide compositions. It is well known that the band-gap of lead halide perovskites

*[97] Motti, S. G. et al. "Photoinduced formation, healing, and passivation of defects in lead halide perovskites". *under review*, (2018)

can be tuned by varying the halide composition, covering the whole visible range. What would be an interesting feature of the material to be applied in optoelectronic devices is rendered impractical by the instability of the lattice. The sharp PL spectrum of the mixed halide material is seen to split under illumination, giving rise to emissive subgap states.[101] Hoke et al. reported that light soaking causes a splitting of X-ray diffraction (XRD) peaks, suggesting segregation into two crystalline phases,[65] one being bromine rich and the other iodine rich. More recently, Barker et al. demonstrated that ion segregation takes place via halide defects, resulting in iodide-rich low-band-gap regions close to the illuminated surface of the film. The ion segregation is a result of higher ion mobility under illumination,[102,103] and driven by the strong gradient in photoexcitation through the thickness of these films, which have strong absorption coefficients.[104] The phase separation in these materials is reversible in dark, as iodine and bromide intermix, driven by entropy, and return the system to a homogeneous condition with the original intermediary band-gap. The formation of domains with distinct band-gaps makes the mixed halide materials a good model for studying ion migration in metal halide perovskites, but similar behavior can be observed in tribromide and triiodide perovskites.

4.2 Photoinduced slow dynamics

4.2.1 PL quenching and enhancement

As discussed in section 1.3.3, the PLQY of metal halide perovskites increase with increasing excitation density until Auger-like processes kick in at high excitation densities. Figure 4.1 shows the Relative PLQY of $MAPbBr_3$, $MAPbI_3$, and $CsPbBr_3$, where this expected behavior can be observed. However, when the curves are obtained in forward (increasing excitation intensity) or reverse (decreasing excitation intensity) order, the curves show hysteresis, with reduced PL efficiency after illumination. In direct contradiction, an enhancement of PL under illumination has also been reported[67,83,96] and a self-healing mechanism was proposed to explain it.[75] These oppositely behaving instabilities have been reported to be dependent on excitation intensity and defect density,[105] and both PL enhancement and quenching have been observed on the same sample depending on light intensity.[106] These effects have been considered individually but a comprehensive picture of the competing processes is yet to be reported. To

consolidate these conflicting observations, the factors that regulate these effects were investigated.

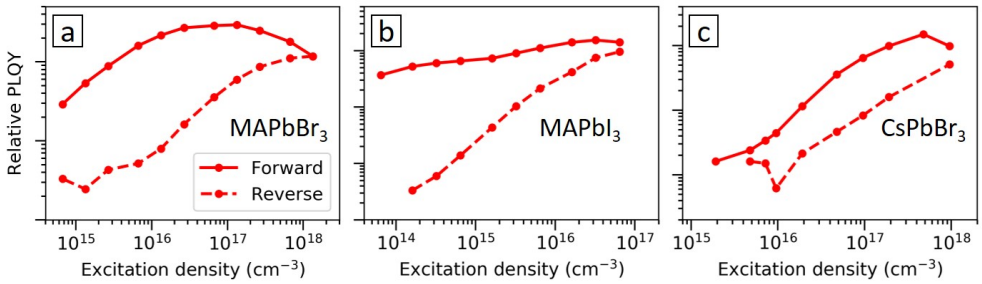

Figure 4.1: Relative PLQY curves of a (a) $MAPbBr_3$, (b) $MAPbI_3$ and (c) $CsPbBr_3$ polycrystalline thin film taken in vacuum with increasing (solid lines) or decreasing (dashed lines) excitation densities. Adapted from: [98]

In order to exclude the effects of oxygen and moisture on the instabilities,[76–78] all measurements were performed under vacuum (pressure $<10^{-5}$ mbar, under constant pumping). Figure 4.2a shows the integrated PL over time, at room temperature, of a polycrystalline film of $MAPbI_3$, excited with a modulated laser with fixed pulse width of 200 ns and varying modulation frequency, i.e. the period (δ) between one excitation pulse and the other. The PL intensity was seen to vary over time, either being enhanced or quenched. At low modulation frequencies, i.e. when δ is long and the sample is in dark for longer times, the PL signal grows. Increasing the time the sample is exposed to light (at high frequencies), a quenching process becomes dominant. This indicates that photoexcitation can lead to different photoinduced processes in perovskites, which have opposite effects on the radiative efficiency. Therefore more detailed experiments were performed to understand the processes in play and which factors regulate single effects.

4.2.2 Temperature dependence

Figure 4.2b shows the temporal evolution of the integrated PL intensity of a $MAPbI_3$ film measured over time after the start of illumination with CW light, which would be analogous to a very high modulation frequency. Each curve was taken on a fresh spot of the sample, at different temperatures. At 77K the PL appears to be stable, but at slightly higher temperatures, the emission increased over time. At even higher

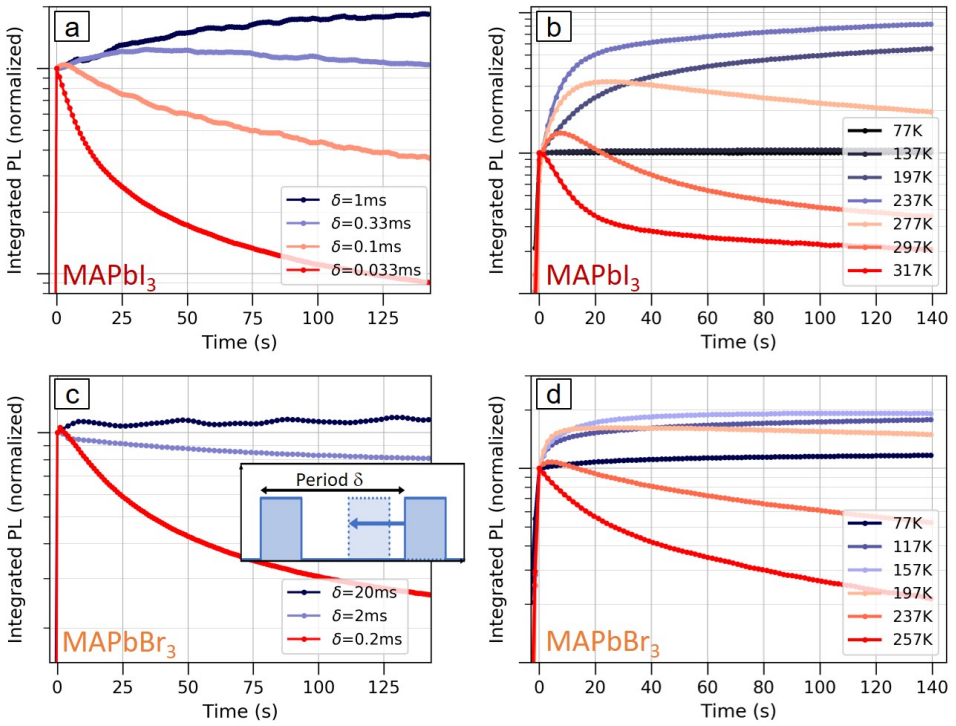

Figure 4.2: Integrated PL intensity over time under illumination (fluence ~0.5 µJ cm-2, excitation density ~10^{16} cm^{-3}) on fresh spots of polycrystalline films of $MAPbI_3$ (a) and $MAPbBr_3$ (c) with increasing modulation frequency (decreasing period) of the excitation light. Pulse width was fixed at 200 ns for $MAPbI_3$ and 10 µs for $MAPbBr_3$; and Integrated PL over time of $MAPbI_3$ (b) and $MAPbBr_3$ (d) at different temperatures under cw excitation. Adapted from: [97]

temperatures, the enhancement is seen combined with a quenching of the PL emission, which is dominant at room temperature and higher, in agreement with the data shown in Figure 4.2a. Similar behavior was observed for $MAPbBr_3$ films, though with different thresholds between PL quenching and enhancement (Figure 4.2c-d).

The temperature dependence of the PL behavior shown in Figure 4.2b,d is evidence of the competition of two thermally activated processes that either enhance or quench the PL emission. The larger contribution of quenching with increasing temperature suggests higher activation energies compared to the enhancement process, and the greater stability of $MAPbI_3$ compared to $MAPbBr_3$ at low temperatures suggests higher activation energies for both processes in $MAPbI_3$.

To confirm this observation a qualitative model was developed to fit the temperature

dependence of the PL instabilities as a sum of two components, one for a growth and one for a decay, each of them varying in temperature with different activation energies. The PL intensity over time for each temperature is fitted to the sum of the two components:

$$I_{PL}(t) = I_0 \cdot PLq(t) + I_0 \cdot PLe(t) \tag{4.1}$$

where I_0 is the initial intensity of PL emission when the sample is first exposed to light and PLq(t) and PLe(t) are the quenching and enhancement of the PL intensity over time, respectively. The individual components are described by stretched exponential functions as:

$$PLq(t) = 1 \cdot e^{-(t/\tau_q)^c} + bg \tag{4.2}$$

$$PLe(t) = Amp_e \cdot (1 - e^{-(t/\tau_e)^c}) + bg \tag{4.3}$$

where τ_q and τ_e are the lifetimes and c is the stretching factor. Each curve of experimental data is normalized by the initial intensity, so the amplitude of PLq is fixed as 1 and the amplitude of PL_e is determined by Amp_e. The term bg defines the lowest value for the quenching decay. Since the maximum extent of these effects cannot be measured, the parameters Amp_e and bg (that describe the maximum and minimum changes in the PL intensity) are left as free parameters to be adjusted according to the experimental data. The temperature dependence of the transients is obtained from the Arrhenius equation:

$$k_{q,e} = A_{q,e} \cdot e^{-Ea_{q,e}/(k_B \cdot T)} \tag{4.4}$$

where $k_{q,e}$ is the rate for each process, which relates to τ as $\tau_{q,e} = \frac{1}{k_{q,e}}$. k_B is the Boltzmann constant[†], T is the temperature, $A_{q,e}$ is the pre-exponential factor and $Ea_{q,e}$ is the activation energy for each process. The set of experimental data for all temperatures were globally fitted with Equation 4.4, which would provide the temperature dependence of $\tau_{q,e}$. Inside the fitting routine, the curves for each temperature are fitted with Equation 4.1. Table 4.1 shows the fit parameters of A and Ea for $MAPbI_3$ and $MAPbBr_3$.

It's worth highlighting that the activation energy values reported in Table 4.1 are only rough estimates, since the fitting process involves many free parameters. Nonethe-

[†] k_B=$8.6173303 \cdot 10^{-5} eV \cdot K^{-1}$

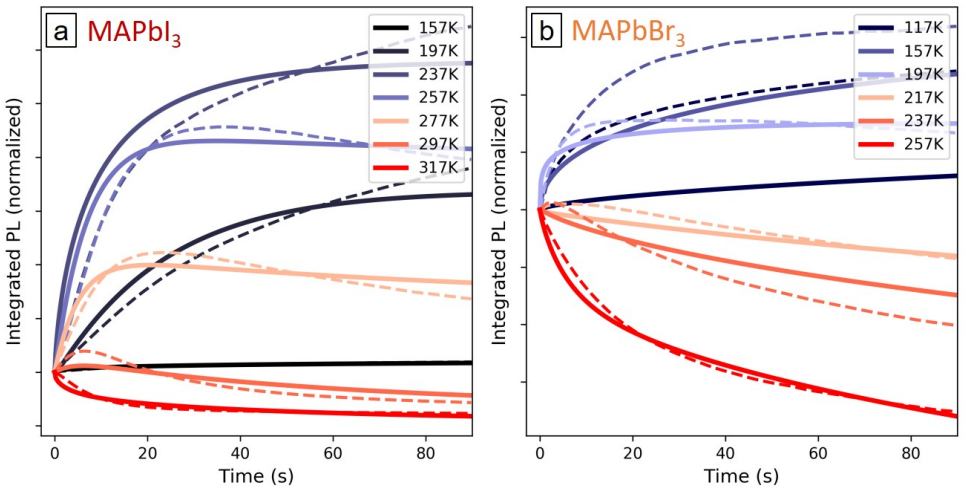

Figure 4.3: Temperature dependence of the PL instabilities on a) $MAPbI_3$ and b) $MAPbBr_3$. Dashed lines are the experimental data from Figure 4.2b-d and the solid lines are fits of Equation 4.1.

Table 4.1: Global fit parameters used on Equation 4.4 for obtaining the values of $\tau_{q,e}$ for the curves on Figure 4.3.

	A_q	A_e	Ea_q	Ea_e
$MAPbI_3$	27.48 ± 0.350	8.497 ± 0.044	0.191227 ± 8.9e-05 eV	0.098742 ± 8.8e-05 eV
$MaPbBr_3$	27.88 ± 0.331	11.36 ± 0.174	0.1837 ± 0.0013 eV	0.0823 ± 0.00038 eV

less, it reproduces the trend observed and it serves as a qualitative proof of concept of the competition of the two thermally activated processes. It also demonstrates that the PL quenching has higher activation energies than the PL enhancement, and that $MAPbI_3$ has slightly higher activation energies for both processes compared to $MAPbBr_3$.

4.2.3 Geometry dependence

Although one can observe dominant enhancement or quenching of PL at specific conditions, the final effect is not always predictable, and different samples can show opposite effects when submitted to the same parameters. To identify which other factors affect these processes, the effect of the experiment geometry was also investigated.

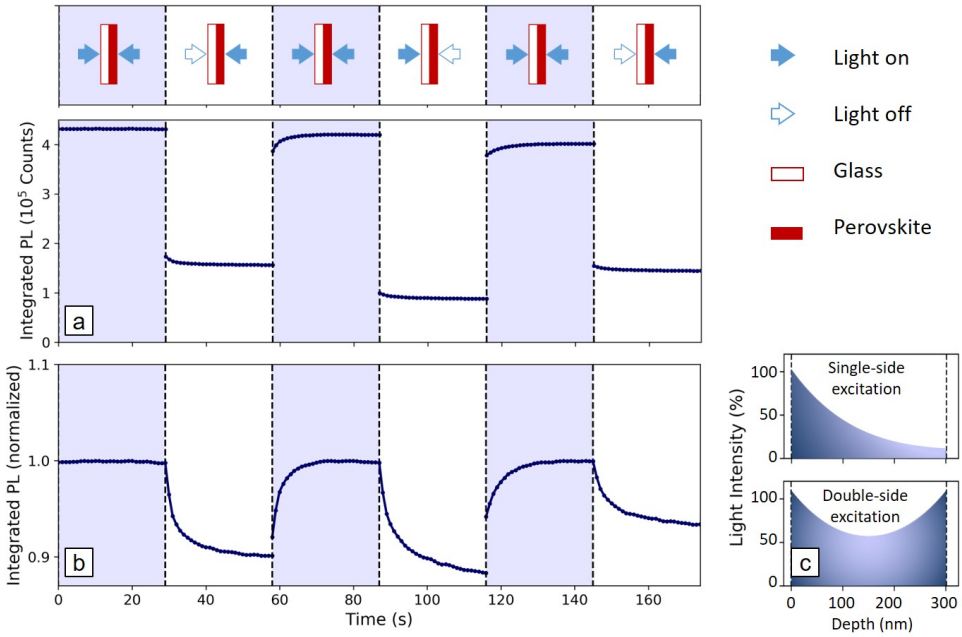

Figure 4.4: a) Integrated PL intensity over time of a $MAPbI_3$ film on glass. Excitation is performed with symmetrical beams (560 nm, CW) of equal intensity impinging on both perovskite and glass side of the sample. The beams are blocked and unblocked according to the illustration on top; b) Same data of (a), but each section of the time trace is normalized to help visualization of the variations over time; c) Photoexcitation profiles for the case of single- and double-sided illumination. Adapted from: [97]

Figure 4.4a shows the integrated PL over time of a $MAPbI_3$ film on glass, illuminated with two collinear excitation beams of equal intensity on opposite sides. The film was first illuminated with the two symmetrical beams on both the film and glass sides. After observation of stable PL emission, one of the beams was blocked. The emission from the remaining excitation beam is seen to quench over time. After unblocking the second beam and restoring the symmetrical excitation, the PL intensity shows an enhancement over time and partially recovers. Repeating the process when blocking the opposite beam gives us to the same behavior. Figure 4.4b shows the same data with each section normalized to exclude the large variations of signal intensity when blocking and unblocking the beams and allowing for better visualization of the intensity changes over time. This indicates a critical role of the illumination profile through the material.

The effect of the illumination profile could also be observed in the dependence of

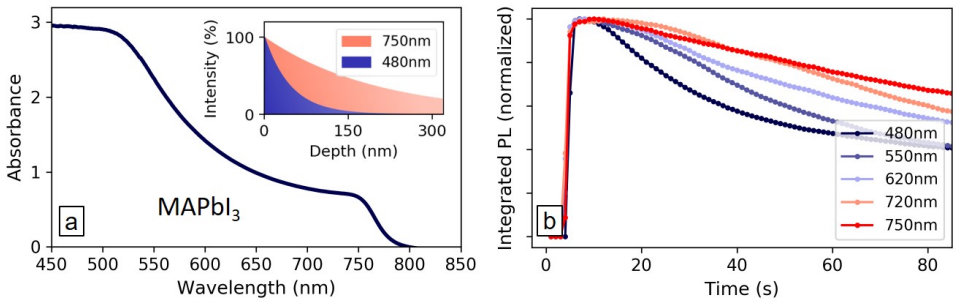

Figure 4.5: a) Absorption spectrum of $MAPbI_3$ thin film and photoexcitation profiles when using 480 nm or 750 nm light (inset); b) Integrated PL over time obtained using excitation light of different wavelengths. Adapted from: [97]

excitation wavelength. As shown in Figure 4.5a, the absorbance of a $MAPbI_3$ film increases significantly at shorter wavelengths, meaning shorter penetration depths and a steeper illumination gradient (inset of Figure 4.5a). Figure 4.5b shows the integrated PL from a $MAPbI_3$ film obtained using different excitation wavelengths. The photon density over the illuminated area was kept constant, correcting for the different photon energies, and each curve was taken on a fresh spot of the film. It was observed that the PL quenching is favored at shorter wavelengths, while exciting the film closer to the band-gap results in more stable PL.

4.3 Defect diffusion

4.3.1 Electronic effects vs structural transformations

Given the long lifetimes of trapped carriers in these materials,[54,88] it has been considered the role of trap-states filling. For investigating if trap-filling effects could result in slow changes in the observed PL intensity the system of rate equations described in Section 1.3.2 was used.

First the TA decays were fitted with a hole dynamics, since this model considers only electron trapping, and the remaining population of free holes will reflect both the radiative decay and the long timescale of trapped carrier relaxation to ground state. The parameters obtained from the fits were used to simulate the steady state conditions

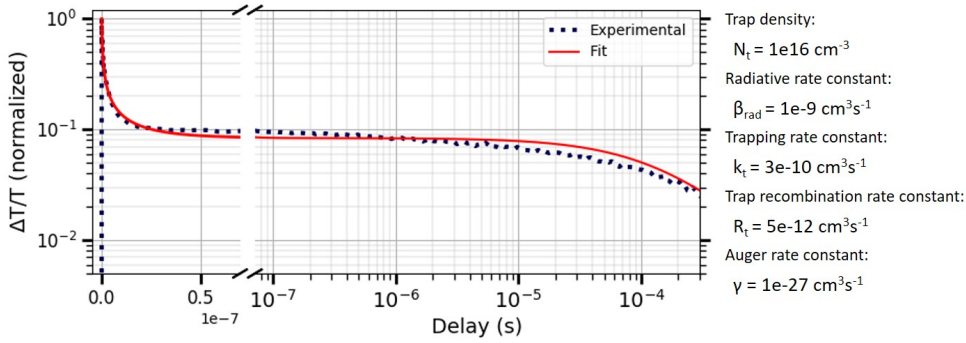

Figure 4.6: Transient Absorption dynamics of a $MAPbBr_3$ thin film taken at the peak of the band-edge photo-bleach (525 nm). Dotted line is the experimental data and solid red line is the fit of a free hole population dynamics obtained from the rate Equation 1.7.

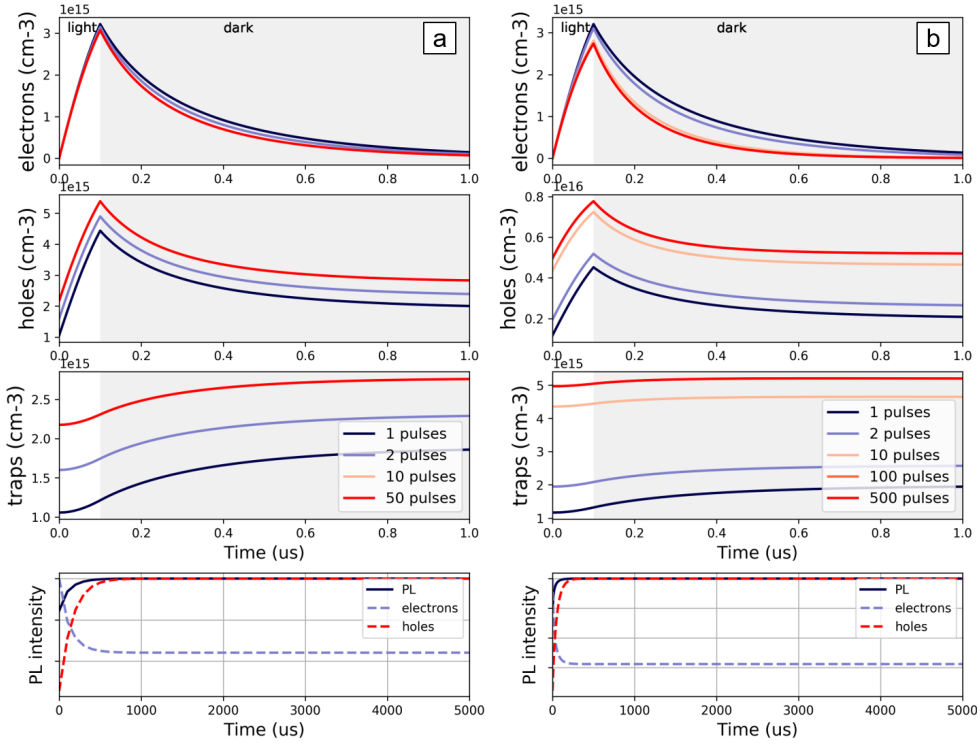

Figure 4.7: Simulation of the modulated illumination with pulses of 100ns and frequencies of (a) 10 kHz and (b) 100 kHz.

from equations 1.6, 1.7 and 1.8.

The evolution of the carrier populations in time was obtained switching the generation rate on and off to simulate the modulated illumination. The PL intensity can change over time because of pulse piling up and trap filling effects, but in the conditions similar to the experiments performed in this work, these effects should reach a steady state condition on a scale shorter than milliseconds. Several variations of the parameters above were tested in order to rule out that longer timescales could result from different combinations of values, but in all the possible scenarios considered, stable PL is established after no more than a second. Therefore it was concluded that the PL instabilities observed in the scale of seconds to minutes are not related to electronic effects.

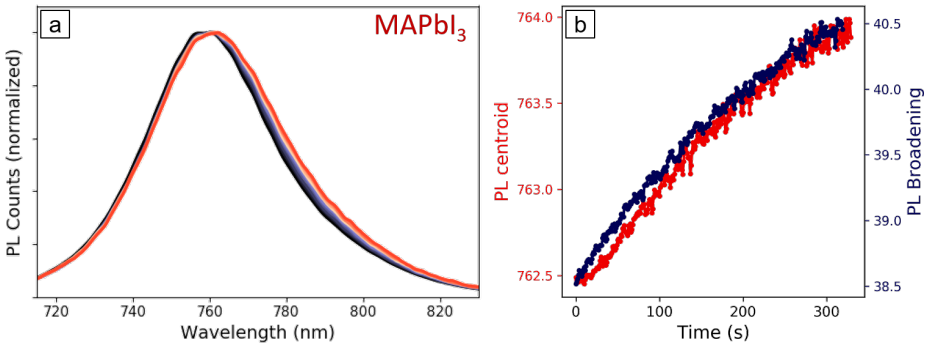

Figure 4.8: a) PL spectrum of a $MAPbI_3$ film during the quenching (100 kHz, 200 ns pulses), from t=0 s (dark blue) to t=300 s (red) under illumination, and b) PL broadening and shift of center of mass over time. Adapted from: [97]

When the spectrum of the emission was monitored during the PL quenching process (Figure 4.8), it could be observed a slight but consistent broadening of the linewidths, which may be consistent with a heating scenario. However, the PL position also slightly red shifts (Figure 4.8), which is the opposite behavior from the usual temperature dependence of this material,[20,40,107] i.e. the band-gap becomes larger as the temperature increases. On the other hand, this is in agreement with an increasing density of trap sites in the film, increasing the disorder in the lattice and density of subgap states.[108]

4.3.2 Mechanisms for defect diffusion-related activity

Section 4.2 showed that the PL quenching is favored by high temperatures, an illumination gradient through the thin film, and a sufficiently high repetition rate of photoexcitation. Comparable observations have been made in mixed halide perovskites of composition $APbI_{(3-x)}Br_x$. Barker et al.[104] have demonstrated that phase segregation into iodine and bromine rich regions occurs as ions migrate via halide defects, and that the ion migration is driven by the strong photoexcitation gradient through the thickness of the films. Once returned to the dark, entropically driven intermixing of the ions returns the system to a homogeneous condition. The effect of the photoexcitation gradient suggests that the photoinduced trap formation that causes PL quenching is associated to the ion migration through the film.

In collaboration with computational studies, a mechanism for these processes was proposed. It's known that $MAPbI_3$ and $MAPbBr_3$ have similar defect chemistry, with the presence of long living electron traps[54,88] (as discussed in Chapter 3). These long lifetimes result in higher steady-state population of the trapped carrier, and it was considered that these filled traps can be reactive and trigger structural transformations, explaining the photoinduced instabilities. Mosconi et al. proposed a photoinduced healing mechanism by Frenkel defect annihilation,[75] i.e. a Frenkel pair formed by an iodide vacancy (V_I^+) and an interstitial (I_i^-), recombines resulting in the healed crystal lattice. The defects I_i^+ and I_i^- tend to aggregate forming a stable defect pair (Figure 4.9a. Electron trapping at I_i^+ affects the stability of the pair and increases the distance of I_i^0/I_i^- (Figure 4.9b, facilitiating the approximation of I_i^- and V_I^+ and their recombination. This process is entropically disfavored, with a small energy barrier (~0.1 eV) related to the defect migration.

The PL quenching, on the other hand, could possibly be associated to a bimolecular mechanism, boosted by increasing the density and/or mobility of reactive species, which is consistent with the prevalence of PL quenching at higher temperatures and higher excitation density. Considering again the long-living trapped electron at I_i^+, two filled traps (I_i^0) could react to form an I_2 molecule:

$$2I_i^0 \longrightarrow I_2 \tag{4.5}$$

which has no energy barrier,[109] but requires the migration and encounter of I_i^0. This

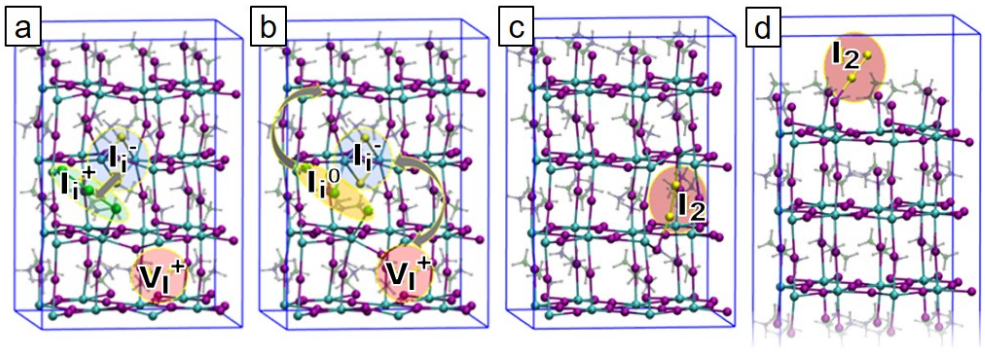

Figure 4.9: a) Optimized structure of the interacting I_i^+/I_i^- defect pair (shaded green and blue areas, respectively) and a distant V_I^+ defect (shaded red area). The formation of the I_i—V_I^+ defects in the presence of an interacting I_i^+ is endothermic by 0.55 eV. b) Electron trapped at I_i^+ to form I_i^0/I_i^- defect pair (shaded orange and blue areas, respectively). The arrows indicate the direction of I_i^0 migration and I_i—V_I^+ annihilation. The formation of the I_i—V_I^+ defects in the presence of a neutral I_i^0 is endothermic by 0.86 eV. c) Optimized structure of an unstable bulk I_2 molecule (dark red shaded area), which migrates to the perovskite (001) surface in d) to form a stable surface bound I_2 molecule (dark red shaded area). Binding of an I_2 molecule to the perovskite surface (bulk) is exothermic (endothermic) by 0.48 (0.40) eV. Data provided by Dr. Daniele Meggiolaro and Prof. Filippo de Angelis. Adapted from: [97]

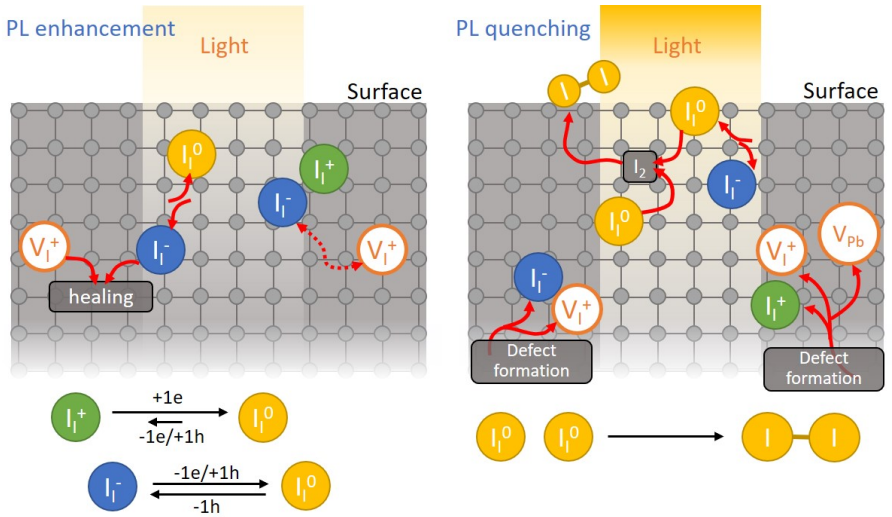

Figure 4.10: Illustration of the possible mechanisms PL enhancement by Frenkel defect annihilation PL quenching promoted by formation of surface-coordinated I_2. Adapted from: [97]

process competes with capture of a second electron at I_i^0, but formation of I_2 is possibly favored. I_2 can be trapped as an unstable complex in the bulk (Figure 4.9c) or it may reform the I_i^+/I_i^- pair. In any case, it tends to migrate to the surface (or grain boundary) where it is stable as surface-coordinated I_2 (Figure 4.9d). The release of I_2 from $MAPbI_3$ films under illumination has been previously detected.[102] The iodine imbalance between surface and bulk (or iodine loss, if I_2 is allowed to escape) can trigger a series of compensating reactions that disrupt the pristine lattice. This is consistent with the wavelength dependence that indicates PL quenching is favored when photoexcitation is concentrated close to the surface.

4.4 Chapter conclusions

By monitoring PL fluctuations under systematic control of the experimental parameters, there could be identified two distinct processes behind the reversible instabilities observed in lead halide perovskites. Excluding atmosphere related effects, it was revealed that long range photoinduced ion motion favors the formation of non-radiative recombination channels. On the other hand, at certain conditions in which the long-range ionic motion is partially blocked, it is possible to observe photo-healing effects.

An important consequence of the role of photoexcitation gradients on these instabilities is that the observations are highly dependent on the experiment parameters, such as wavelength and repetition rate of excitation light, film thickness, spot size, and temperature. This could explain some of the discrepancies found in literature. These phenomena can alter the semiconductor properties, i.e., the carrier dynamics, trap density, PLQY and device efficiency, affecting the interpretation of optical measurements. It's important to consider the order in which data is acquired when varying the excitation intensity and temperature, as there might be strong hysteretic effects. It can also be suggested that previous light soaking should be considered to guarantee the sample stability during the experiment and that uniform illumination (such as achieved with large spot diameters and longer wavelengths close to the band-gap) should be preferred in order to reduce ion migration.

In combination with first-principle calculations a model of photoinduced ion migration was proposed that can result in PL quenching or enhancement. The quenching is associated with the formation of I_2 from two I^0 species. Thus it will be favored in the presence of high trap density concentration and/or a high ionic mobility to increase

the probability of a bimolecular encounter. The stabilization of coordinated I_2 at the surface (or grain boundary) is a fundamental factor for the efficiency loss. Based on this model, the key to avoid PL quenching and perovskite degradation is the passivation of surface sites to which I_2 can bind to. These surface sites, even if not directly involved in trapping/detrapping events, stabilize the formation of I_2, leading to iodine imbalance in the bulk and stimulating the production of additional defects.

5

Defect passivation and the role of atmosphere

Atmosphere has been known to have a strong impact on metal halide perovskites. Defect passivation has been observed after the exposure of thin films to air, however with detrimental effects over longer time scales. This Chapter investigates the effects of atmosphere on perovskite thin films and how it can inspire the development of new methods for surface treatment and encapsulation. Section 5.1 shows the effect of oxygen and moisture on the PL efficiency and stability and Section 5.2 demonstrates the application of polymer coating for improved material stability and solar cell performance. The contents of Section 5.1 have been adapted from Motti et al. (2016)* and Section 5.2 has been adapted from Kim et al. (2018).†

5.1 Atmospheric effects

Promising semiconductors for photovoltaic applications are expected to have a good resistence to the environmental conditions that solar panels need to withstand. Lead

*[98] Motti, S. G. et al. "Photoinduced Emissive Trap States in Lead Halide Perovskite Semiconductors". *ACS Energy Lett.*, 1, 4, pp. 726-730. (2016)

†[110] Kim, M., Motti, S., Sorrentino, R., and Petrozza, A. "Enhanced Solar Cells Stability by Hygroscopic Polymer Passivation of Metal Halide Perovskite Thin Film". *Energy Environ. Sci.*, DOI: 10.1039/C8EE01101J, (2018)

halide perovskites unfortunately have low damage thresholds compared to silicon, for example. Degradation of perovskite materials can be caused by moisture, oxygen, light, and heat[111,112]. The degradation mechanisms in which oxygen and moisture play important roles[79,113–116] are usually considered as one of the main challenges to be overcome for reliable device application. However, in shorter timescales, the exposure of the material to air has also shown positive effects. In particular, it has been reported that the PL intensity can increase up to three orders of magnitude when samples are exposed to air[76,77]. This section investigates the effects of oxygen and moisture on the defect density and instabilities of lead halide perovskites.

5.1.1 Defect passivation in the presence of oxygen

As discussed in Chapter 4, the relative PLQY of lead halide perovskites show a hysteretic behavior when cycling back from high to low excitation density under vacuum. When the experiment is performed in air, the observations are different.

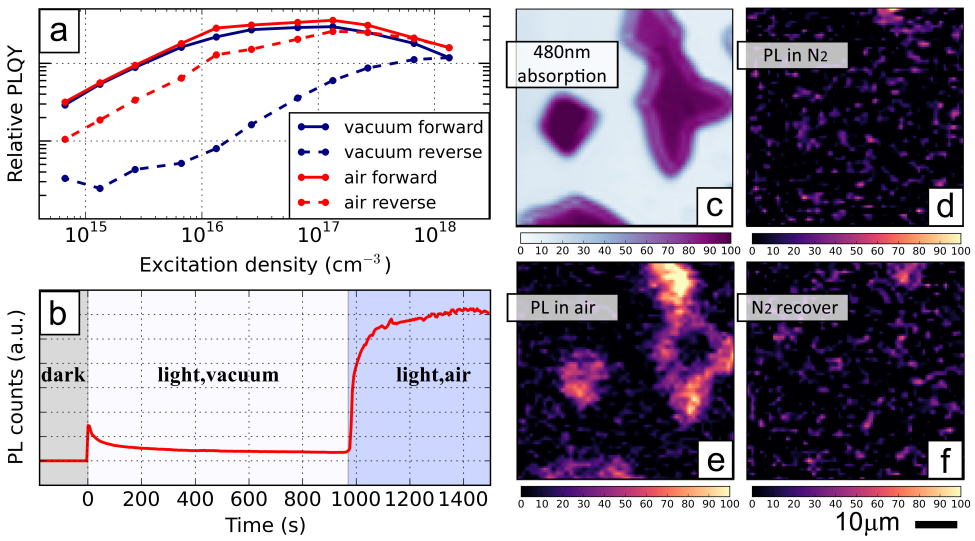

Figure 5.1: a) Relative PLQY curves of $MAPbBr_3$ polycrystalline thin films in air (red) and active vacuum (blue), taken with increasing (solid lines) or decreasing (dashed lines) excitation densities; b) Time trace of integrated PL under illumination in vacuum and during air exposure; c) Transmission (taken at 480 nm) and d-f) PL maps under N_2 flow and air. Adapted from: [98]

Figure 5.1a shows the relative PLQY of $MAPbBr_3$ thin films kept either in vacuum or in ambient atmosphere. The solid lines show the data collected with increasing

excitation density, while the dashed lines show the data collected on the same spot of the sample with the excitation density varying back from high to low values. When the experiment is performed in air, the relative intensity of PLQY was higher and the a hysteretic behavior was strongly attenuated. To investigate the time scale in which this changes occur, the steady-state PL intensity was monitored over time. Figure 5.2b shows the evolution of the PL intensity, at a excitation density of 10^{16} cm^{-3}, first under active vacuum, just after the excitation beam is unblocked (t=0), then followed by exposure to air. Under active vacuum, a quenching of the PL emission was observed under illumination, such as discussed in Chapter 4. As soon as the sample is exposed to air, substantial enhancement of PL emission was observed. The microscopy maps shown in Figure 5.2c-f provide further visualization of this effect. Figure 5.1c shows the transmission map of excitation light at 480 nm on a sample of isolated, micrometer sized, $MAPbBr_3$ crystallites. Figure 5.1d shows the PL map under N_2 flow, which shows very low signal. When exposing the same sample to air, the crystallites gradually became more luminescent, as shown in Figure 5.1e. It was also observed that this effect is reversible, as shown by the quenched PL in Figure 5.2f, obtained when the sample was brought back under N_2 flow.

To understand these significant changes to steady-state PLQY, the recombination dynamics were also investigated by time resolved PL and transient absorption (TA), under different atmospheric and illumination conditions. Figure 5.2a shows the PL decays of the integrated PL under active vacuum, from low to high excitation density. As described in Chapter 4, when the experiment is performed from high to low fluences (Figure 5.2b), a photoinduced increase of trap density is observed, which results in shorter PL lifetimes. On the other hand, after the sample is exposed to air, the lifetimes increase by over one order of magnitude (Figure 5.2c). Measurements in air were taken from the same spot on the sample, from high to low excitation density, after a few minutes of stabilization under continuous illumination. The intensity dependence of the dynamics measured in air recover the trend seen on a fresh spot of the sample as in Figure 5.2a, showing the expected transition from trap-limited monomolecular decay to bimolecular recombination with increasing excitation density, such as discussed in 1.3.2. Furthermore, the observed dynamics in air become more stable and were not seen to change depending on the order of measurement.

To investigate the dynamics of trapped carriers transient absorption (TA) measurements, which is sensitive to both emissive and non-emissive species, were also performed. Given the long time scales for recombination of free and trapped carriers in lead halide

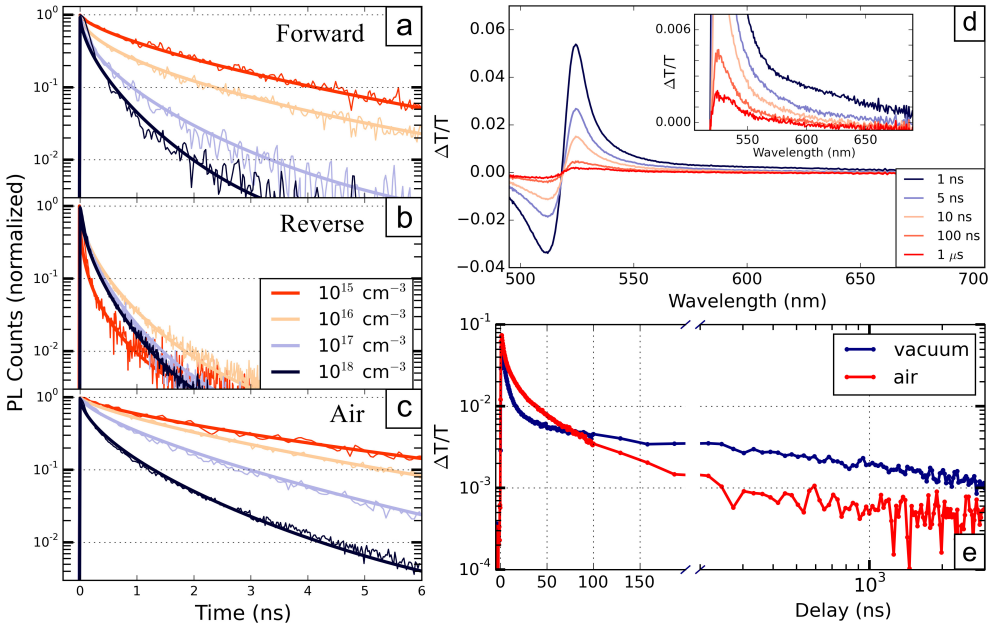

Figure 5.2: PL decays of MAPbBr3 thin film with increasing (a) and decreasing (b) excitation density in vacuum, and (c) in air. d) Transient Absorption spectra of $MAPbBr_3$ thin film, showing a long subgap bleach (inset); e) TA dynamics at 530 nm in vacuum (blue) and air (red). Adapted from: [98]

perovskites[54], the measurements were performed in the ns-µs regime.

Before the acquisition, the sample was stabilized in vacuum under illumination corresponding to an excitation density of 10^{17} cm^{-3}. Figure 5.2d shows the TA spectra obtained in vacuum. The positive peak at 525 nm can be assigned to the photo-bleach (PB) that is induced by the population of photoexcited carriers at the edge of the conduction or valence bands, thus its dynamics follow those of both the electrons and holes. In the TA spectrum, the PB band is seen to extend as a weak tail to longer wavelengths (inset of Figure 5.2d) that corresponds to the filled trap states. The dynamics of the band-edge PB, probed at 525 nm, (Figure 5.2e) shows an initial decay that is completed in a few ns and a slow component extending over the experimental limit of 3 microseconds. Whilst the first component follows the carrier trapping dynamics as well as the bimolecular radiative recombination dynamics, as seen in the PL decays, the slow component can be assigned to the recombination dynamics of the trapped carrier with the free carrier of opposite sign.

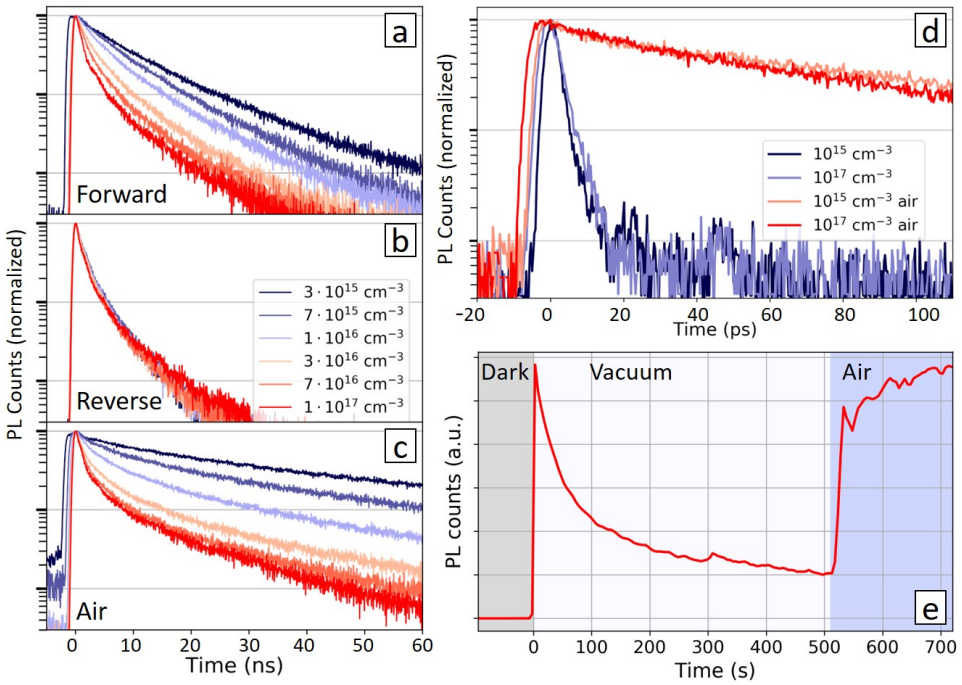

Figure 5.3: PL decays of $MAPbI_3$ thin film with increasing (a) and decreasing (b) excitation density in vacuum, and (c) in air; d) PL decays of $CsPbBr_3$ thin film at different excitation densities under vaccum (blue) or in air (red); e) Time trace of integrated PL of a $CsPbBr_3$ thin film under illumination in vacuum and during air exposure. Adapted from: [98]

After exposure to air the fast component of the dynamics shows a longer lifetime compared to vacuum, in agreement with the PL dynamics behavior, while the slow component is quenched due to lower density of trapped carriers. These observations provide further evidence of the passivation of trap states in air, and allows to estimate a trapping time scale around few ns and a recombination time of trapped carriers of the order of a few µs.

It's worth highlighting that the passivation of trap states in air is observed not only for $MAPbBr_3$, but also for $MAPbI_3$ and $CsPbBr_3$ polycrystalline films as demonstrated by the PL intensity and dynamics in vacuum and air, as shown in Figure 5.3.

The chemistry underlying these effects has not yet been completely explained. It has been demonstrated that oxygen molecules can interact with the perovskite under

illumination leading to the formation of superoxide anion integrated in the perovskite lattice.[79,117–119] Another possible mechanism for the passivation is the oxidation of interstitial iodine as proposed by Meggiolaro et al.[100] These mechanisms may explain the interaction of oxygen with defects in the perovskite semiconductor and result in PL enhancement, but are also associated with degradation processes that occur over longer time scales.

5.1.2 The effect of moisture

To confirm that the PL enhancement described in Section 5.1.1 was related to the presence of oxygen, the effects of exposure of the films to moisture were also investigated.

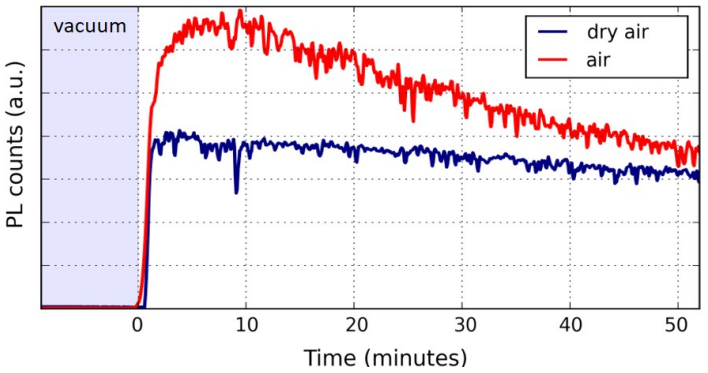

Figure 5.4: Integrated PL intensity of $MAPbBr_3$ after exposured to dry air (blue) and ambient atmosphere with relative humidity ~40% (red). Adapted from: [98]

Figure 5.4 shows the integrated PL intensity of a $MAPbBr_3$ film over time. After a few minutes of illumination in vacuum, the sample was exposode either to dry air (purity grade 5.5, i.e. 99,9995%) or air from the room (red line), which had a relative humidity around 40%. After exposure of the sample (at time = 0), PL enhancement was observed in both cases, indicating that oxygen is probably the main active agent in the passivation process. When the sample is exposed to moist air instead, a stronger enhancement was observed, followed by a quenching of the PL over longer times.

Water absorption in the perovskite layer has been considered a major issue for device stability[115], as the water molecules trigger the degradation process[114,116]. However Leguy et al. has demonstrated that the first stage of hydration of the crystal structure is fully reversible[120]. Given the stronger enhancement of PL when the sample is exposed to

moist air, it is possible that the hydration of the surface and grain boundaries contribute to the enhancement at an early time, but is detrimental after exposure for longer than a few minutes.

5.2 Surface treatment and encapsulation

As discussed in the previous sections, oxygen and moisture can have either positive or negative effects on perovskite carrier recombination efficiency. Understanding these effects can help the development of surface treatments and encapsulation methods. Interface engineering of perovskite surfaces by inserting a layer between the perovskite and charge transport layers has been an option to improve device stability[121,122]. The interfacial layers can either be semiconducting or insulating, as long as they are thin enough to allow for charge tunneling. According to the choice of material, these interlayers can not only protect the perovskite from degradation but also passivate the interface, reducing undesirable losses by charge recombination through defects[123].

The moisture related degradation mechanisms of perovskite films can be inhibited by device encapsulation with hydrophobic barrier layers. However, to efficiently protect the perovskite from water interaction, the hydrophobic barrier layer should providde complete film coverage, and since the perovskite layer is hydrophilic, depositing a uniform hydrophobic layer on top is likely to lead to the formation of rough films with pinholes. Encapsulation with effective water barrier layers often require complicated processes or expensive materials[124,125]. This Section studies perovskite films covered with low cost insulating polymers and compare the benefits of hydrophilic and hydrophobic materials on the semiconductor performance and stability.

5.2.1 Hygroscopic vs hydrophobic polymer encapsulation

A thin polymer layer was deposited over the perovskite film to improve the semiconductor stability. Two polymers were compared: a hygroscopic polymer, polyethylene oxide (PEO), which absorbs water before the perovskite layer and a hydrophobic polymer, polystyrene (PS), which repels water molecules from the perovskite layer. The degree of coverage of the polymer films on the perovskite surface (ϕ) depends on the

concentration of the polymer precursor solution. ϕ was estimated by the chemical surface composition obtained from X-Ray Photoelectron Spectroscopy (XPS).

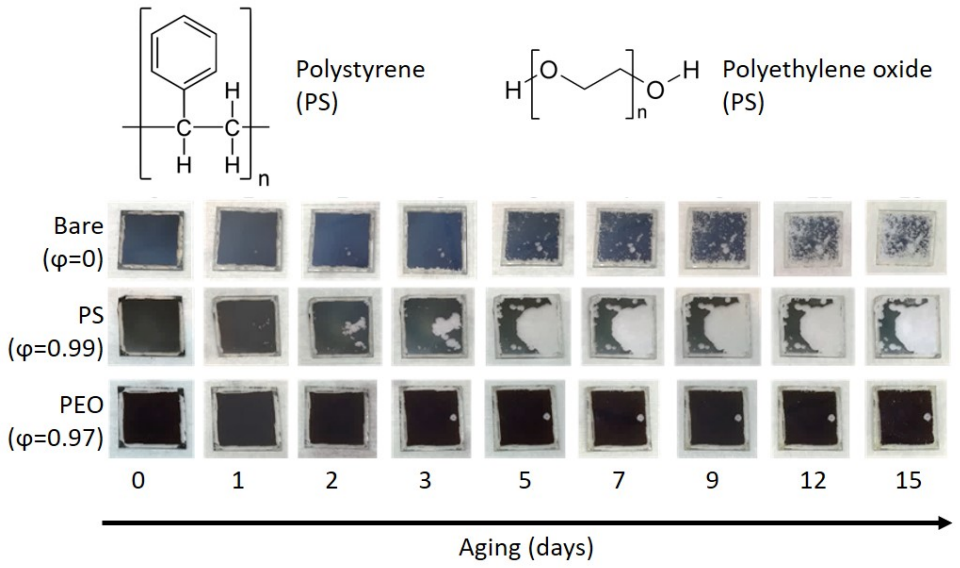

Figure 5.5: Photographs of the $MAPbI_3$ films with and without PEO and PS passivation layer processed from 10 mg/ml concentrations ($\phi \sim 0.99$) during exposure to a relative humidity of 88% over 15 days. Photos taken by Dr. Min Kim. Adapted from [110].

Figure 5.5 shows the appearance of the perovskite films with and without polymer layers after exposure to high humidity (88%) over 15 days. The bare perovskite film gradually turned transparent over time due to the hydration of the lattice. The PS covered film did not efficiently avoid this process, while the PEO covered perovskite showed significantly higher stability.

Figure 5.6a shows the relative PLQY of $MAPbI_3$ thin films as a function of fluence, in the range between 10^{-2} and 1 J·cm^{-2} (CW illumination, corresponding to photon densities between $\sim 10^{20}$ - 10^{22} cm^{-3}). To exclude the effect of oxygen and moisture, the samples were kept and measured in vacuum. The solid lines show the data collected with increasing excitation intensity, while the dashed lines show the data collected in reverse order from high to lower intensities. In the case of bare perovskite film, it can be observed the hysteresis of the curve (as was discussed in Chapter 4). The PS-capped perovskite film also shows some PL hysteresis, though less pronounced than the bare film. In agreement, when illuminating a fresh spot of the sample at a fluence of $\sim$0.1

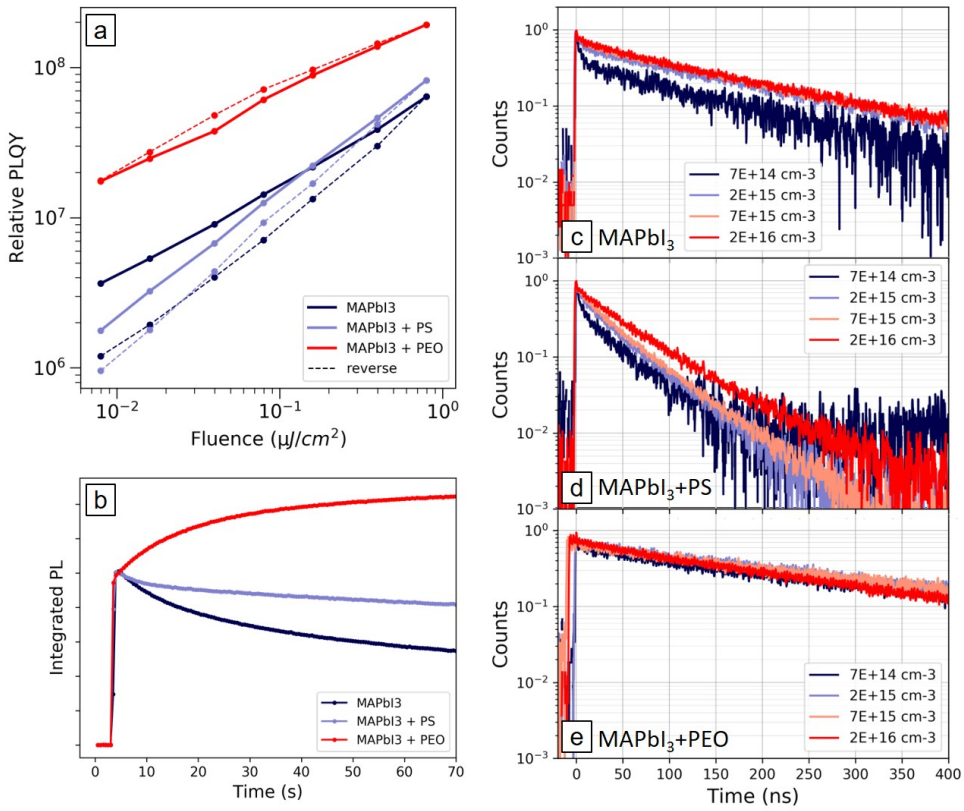

Figure 5.6: a) Relative PLQY curves of $MAPbI_3$ thin films without polymer passivation (dark blue), covered with PS (light blue) and with PEO (red), taken with increasing (solid lines) or decreasing (dashed lines) excitation densities; PL decays of $MAPbI_3$ thin films a) without polymer passivation, b) covered with PS and c) covered with PEO. Adapted from [110].

$\mu J \cdot cm^{-2}$ (corresponding to the central point in the fluence range in Figure 5.6a) and monitoring the integrated PL signal over time (Figure 5.6b), a quenching could be observed for both samples, more pronounced on the bare $MAPbI_3$ thin film. The PEO coated sample showed a higher PL signal, indicating a decrease in density of defects in the semiconductor and a reduced hysteresis, with a small positive hysteretic behavior. When monitoring the integrated PL intensity at 0.1 $\mu J \cdot cm^{-2}$ illumination, an enhancement was observed. The enhancement of PL, as discussed in Chapter 4, is related to a self-healing process and competes with the PL quenching. At room temperature and CW illumination the dominant observation of PL enhancement suggests that the

mechanism leading to PL quenching is blocked. Figure 5.6c-e shows the PL dynamics of the $MAPbI_3$ thin films with and without polymer coating. The film covered with PEO shows longer lifetime with respect to the bare perovskite, which is consistent with a decrease in trap density due to passivation of the surface defects. The film covered with PS shows shorter lifetime than the bare perovskite, which, combined with the low PL efficiency, suggests enhanced non-radiative recombination at the interface.

The nature of the interaction between perovskite and PEO has been investigated with XPS measurements (work performed by Min Kim, see reference [110]), comparing the core level scans of Pb4f of the films with and without polymer coating. While the PS-coated film shows no difference from the pristine perovskite, the PEO-coated perovskite exhibits additional peaks at lower binding energy that can be assigned to Pb-O. This indicated that the O in the PEO molecule can bind to the perovskite undercoordinated Pb on the surface. Although it has been argued that the halogen vacancies associated with the undercoordinated Pb result in only shallow trap states,[59,90,91] these sites can play an important role in the degradation mechanisms due to their interaction with O_2 and H_2O.[79,117–119] Considering a scenario of ion migration through defect sites, it can be inferred that the passivation of such defects can limit the mobility of ions improving the photo-stability. Furthermore, it was demonstrated in Chapter 4 that I_2 can form in $MAPbI_3$ and it is stabilized at the surface. The PEO layer can effectively passivate the surface sites which I_2 can bind to. This points out the important role of the surface in the photoinstabilities and is consistent with the strong effect of surface treatment for improving stability and performance.

5.2.2 Polymer interlayers applied in solar cell devices

The passivating PEO layer has also a significant technological relevance as it allows for the formation of high quality interlayer thin films which can be easily implemented in perovskite solar cells.

The PEO interlayer was deposited between the perovskite active layer and the selective charge extracting layers, either on the bottom or on the top of the perovskite film, or on both interfaces, as illustrated in Figure 5.7a. The devices were fabricated and characterized by Dr. Min Kim. Figure 5.7b shows the current density voltage (J–V) curves of $MAPbI_3$ solar cells with and without PEO interlayers and Table 5.1 shows the values of current density (J_{SC}), open circuit voltage (V_{OC}), power conversion efficiency

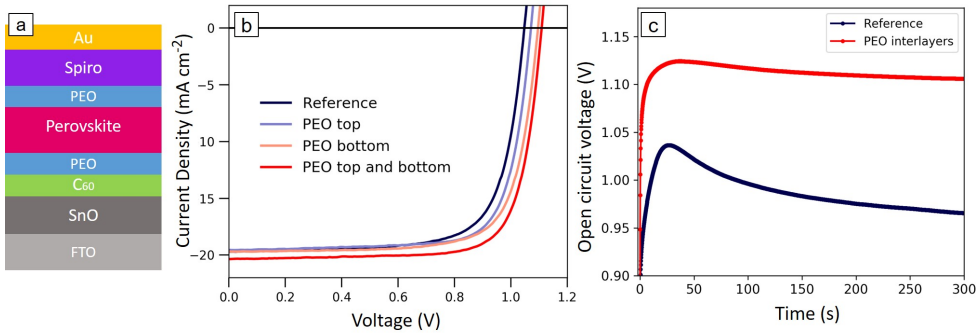

Figure 5.7: a) Device architecture and b) Current density voltage (J–V) curves of $MAPbI_3$ devices with and without PEO interlayers; c) V_{OC} over time from the device with top and bottom PEO interlayer and the reference device, under one sun illumination. Devices fabricated and characterized by Dr. Min Kim. Adapted from: [97]

(PCE) and fill factor.

Table 5.1: Photovoltaic parameters of $MAPbI_3$ devices with and without PEO interlayer [Devices fabricated and characterized by Min Kim].

	Scan direction	J_{SC} (mA/cm^2)	V_{OC}	PCE (%)	Fill Factor
Reference	Backward	19.72	1.049	15.05	0.73
	Forward	19.66	1.017	13.55	0.68
PEO Bottom	Backward	19.70	1.097	16.14	0.75
	Forward	19.64	1.082	14.46	0.68
PEO Top	Backward	19.57	1.071	15.86	0.76
	Forward	19.51	1.054	14.47	0.70
PEO top/bottom	Backward	20.35	1.109	17.23	0.76
	Forward	20.29	1.092	15.50	0.70

The increased V_{OC} in the devices fabricated with PEO interlayers is evidence of the surface passivation and reduced trap-assisted carrier recombination. Besides the improved performance, the PEO interlayers also result in improved stability, as demonstrated by the V_{OC} variations over time in Figure 5.7c. While the reference device shows a decrease in V_{OC} over a few minutes under constant illumination (in solar simulator, at one sun intensity, i.e. 100 mW/cm^2), the device made with PEO interlayers (top and bottom) shows higher stability, and some enhancement of V_{OC} over time, which is

consistent with the observed instabilities in the radiative efficiency (Figure 5.6b).

5.3 Chapter conclusions

Upon exposure to oxygen, the passivation of defects was observed, leading to a substantial enhancement of the PL and longer carrier lifetimes. It is interesting to note that the enhancement of the PL in oxygen happens even in samples exposed to oxygen for a long time prior to the photo-excitation. This suggests a combination of oxygen and photo-excitation is needed for effective defect passivation, which may be an effect of defect deactivation occurring by the reaction of oxygen molecules with trapped carriers. Some research groups have performed computational studies to investigate the interaction of oxygen molecules with the perovskite lattice and proposed a few possible mechanisms, such as the incorporation of superoxide[79,118] or the oxidation of interstitial iodine[100].

Despite the drastic enhancement of radiative efficiency observed upon exposure of the films to ambient atmosphere, oxygen and moisture can trigger degradation processes over long timescales.

These effects of the environment on the behavior of perovskites can lead to the development of better encapsulation and surface treatment methods aiming for improved device performance and stability. To demonstrate that, the semiconductor encapsulation was performed with either a hydrophilic or hydrophobic polymer layer. In particular, applying PEO (a hydrophilic polymer) to coat the semiconductor film allows for reproducible and high-quality deposition on the hydrophilic surface of perovskite. Furthermore, the hygroscopic polymer slows down the perovskite hydration process, preventing degradation. Spectroscopic studies demonstrated the chemical interaction of PEO with undercoordinated Pb on the perovskite surface. Applying PEO as an interlayer between the perovksite and the charge extaction layer in solar cell devices improves semiconductor photo-stability and the device V_{OC}. This study provides not only a fundamental understanding of degradation mechanism of perovskite but also a promising strategy to protect perovskite layer by using functional polymer layer.

6

How far can we go? The limits for radiative efficiency

Apart from competing trapping processes and surface losses, additional factors influence the carrier recombination and limit the efficiency of PL. The synthesis of colloidal nanocrystals (NCs) has been reported as an interesting approach for obtaining highly emissive and defect free perovskite crystals. This Chapter shows a dependence of the PLQY on crystal size, where it's observed that the larger crystals have lower PLQY. The Raman spectra indicate stronger lattice strain in larger crystals, suggesting a difference in the phonon distribution that could affect carrier dynamics and could be related to intrinsic limits for lead halide perovskite PLQY.

6.1 The efficiency limits for lead halide perovskites

According to the Shockley-Queisser model, the maximum power conversion efficiency of a solar cell device depends on the semiconductor bandgap, and the fundamental limit for of perovskites solar cells is 31%[16,17]. For reaching such efficiency, however, the following assumptions must be true:

1. Internal conversion efficiency equals 100%: That is, every photon absorbed results in one electron-hole pair.

2. Radiative efficiency equals 100%: That is, non-radiative recombination is negligible.

3. Photon recycling: if a photon is emitted by radiative recombination of an electron-hole pair, it's reabsorbed.

In a real solar cell device, it must be considered the losses from reflection, absorption of multiple layers, parasitic resistence, and angular dependence. It is not in the scope of this work to discuss all these factors. This Chapter focuses instead on the radiative efficiency of the material.

The PLQY can be defined in terms of the radiative and non-radiative recombination rates (k_{rad} and k_{nr}) as:

$$PLQY(\%) = \frac{k_{rad}}{k_{rad} + k_{nr}} \cdot 100 \tag{6.1}$$

which can be related to the measured PL lifetime (τ) by:

$$PLQY(\%) = \frac{\tau}{\tau_{rad}} \cdot 100 \tag{6.2}$$

where τ_{rad} is the radiative recombination lifetime ($\tau_{rad} = 1/k_{rad}$).

In practice, 100% PLQY is not very realistic, specially in solution processed materials with high density of defects. Also, according to Stokes' law, part of the excitation energy will always be converted into other forms of energy rather than a photon.[80] In metal halide perovskites, the Stokes shift is very close to zero, meaning that after thermalization of carriers to the band edge, little energy is dissipated as heat (considering exclusively radiative recombination). This overlap between absorption and emission energies is also very beneficial for photon recycling. It is also one of the basic requirements for lasing applications.

For reaching the maximum device efficiency, the non-radiative recombination channels in the semiconductor must be negligible (that is, $k_{rad} >> k_{nr}$). The most common non-radiative recombination path is a trap-assisted mechanism, such as discussed in Section 1.3.1. This includes very efficient surface recombination, that is mediated

by dangling bonds and imperfections present at the grain boundaries and surfaces of the thin film. Auger-like processes make up another non-radiative channel (as it was briefly discussed in Section 1.1.5), which is specially effective at high carrier densities or in confined structures. Alternatively, the system can relax by dissipating energy via multi-phonon process. This relaxation mechanism is usually very unlikely without the assistance of intra-gap states and without strong exciton/electron-phonon coupling.

The previous Chapters of this thesis presented a self-healing mechanism, atmosphere passivation, surface treatment and the possibility to control the nature and the activity of defects in lead halide perovskites. Although all these processes can enhance the radiative efficiency of the material, PLQY values of 100% in polyscrystalline perovskite thin films have not been reported to date. The colloidal synthesis of crystals as small as a few nanometers is an interesting approach for obtaining highly emissive and nearly defect free perovskite crystals, allowing for very bright emission over a wide range of wavelengths, with PLQYs reaching over 90% and interesting technological applications[7,10,126–128]

6.2 Perovskite nanocrystals

Nanocrystals (NCs) have been previously fabricated from either hybrid organic-inorganic or fully inorganic perovskites. The first colloidal synthesis of the fully inorganic $CsPbX_3$ NCs was reported by Protesescu et al.[129], yielding monodisperse cubic quantum dots and different compositions, where X is either Br, Cl, I or mixed Cl/I and Br/I systems. A mixture of oleylamine and oleic acid in reaction medium stabilizes the NCs in the colloidal suspension, and temperature control result in different sizes and tunable emission. The values reported for the exciton Bohr radius were 7 nm for $CsPbBr_3$ and 12 nm for $CsPbI_3$,[129] determining the size range that presents confinement of the carrier wavefunction. Low temperatures will result in smaller crystals that consequently show more blue-shifted emission. The band gap can also be tuned by controlling nanoplatelets thickness[130] or by anion exchange between the crystals[131].

Figure 6.1 shows PL spectra of cubic NCs (synthesized by Dr. Quinten Akkerman) compared to a polycrystalline drop cast film with micrometer size crystallites. The polycrystalline film has the center of emission is around 540 nm. The smaller crystals show a blue shift due to weak quantum confinement. Figure 6.1b shows the PL dynamics of the small (6 nm) and large (30 nm) NCs at two different excitation intensities. The PL

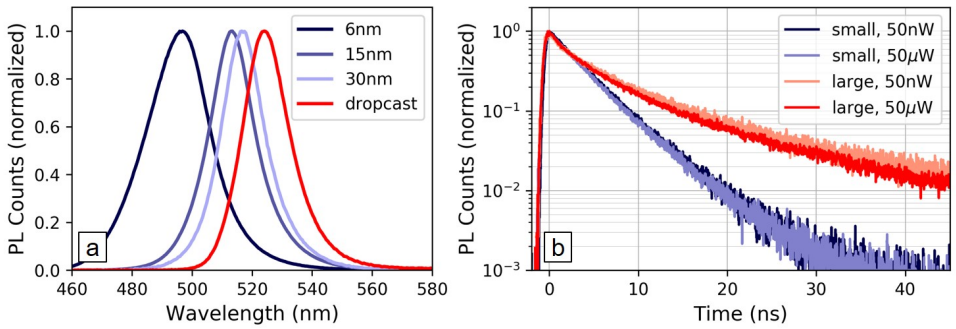

Figure 6.1: a) PL spectra of $CsPbBr_3$ NCs of different sizes, compared to a drop cast film with micrometer size crystallites; b) PL dynamics of small (6 nm) and large (30 nm) $CsPbBr_3$ NCs at 50 nW and 50 μW of excitation intensity. PL lifetimes are $\tau_{6nm} \approx 3.8ns$ and $\tau_{30nm} \approx 4.8ns$.

lifetimes are shorter in the small crystals and not dependent on the excitation intensity in both cases.

Figure 6.2a shows the PLQY of the NCs from Figure 6.1. The polycrystalline film shows the trap filling behavior as discussed in Section 1.3.3, while the colloidal NCs show no intensity dependence of the PLQY. A size dependence of the efficiency can also be observed, with PLQY ranging from 80% to 20% with increasing NC size. The first obvious effect of NC size would be the role of the surface, that increases relative to the bulk volume with decreasing size. Surface losses would however result in the opposite trend, with lower PLQY in smaller crystals. The high PLQY observed in the NCs around 6 nm size is possible because the colloidal NCs are stabilized in suspension by long ligands that passivate the dangling bonds of the surface. The lower values of PLQY in larger NCs are therefore probably related to bulk properties.

Figure 6.1b shows the PL decays obtained from colloidal NCs of two different sizes, where it can be observed shorter lifetimes for the smaller (6 nm, $\tau_{6nm} \approx 3.8ns$) NCs compared to the larger (30 nm, $\tau_{30nm} \approx 4.8ns$) ones. Having the experimental values for PLQY and τ, the radiative and non-radiative rates can be evaluated from Equations 6.1 and 6.1:

$$\begin{array}{llll} \mathrm{NC}_{6nm}: & k_{rad} \approx 2 \cdot 10^8 s^{-1} & \mathrm{NC}_{20nm}: & k_{rad} \approx 4 \cdot 10^7 s^{-1} \\ & k_{nr} \approx 5 \cdot 10^7 s^{-1} & & k_{nr} \approx 2 \cdot 10^8 s^{-1} \end{array}$$

The estimated values obtained for k_{rad} in the 6 nm NCs is about 5 times higher with respect to the 30 nm NCs, while k_{nr} is 4 times higher for the 30 nm NCs. The

reduced size of the NCs imply in higher exciton binding energy and possibly a high radiative efficiency from excitonic states, although it has been suggested that even in these colloidal crystals there is a predominance of free carriers.[132] The enhanced overlap of electron and hole wavefunctions result in higher radiative rates in NCs with reduced size. The higher non-radiative rate in larger NCs could be the result of a higher presence of defective crystals from the synthesis, decreased colloidal stability resulting in aggregation and poor surface passivation of the ligands. Alternatively, it could be related to more fundamental differences between the crystals.

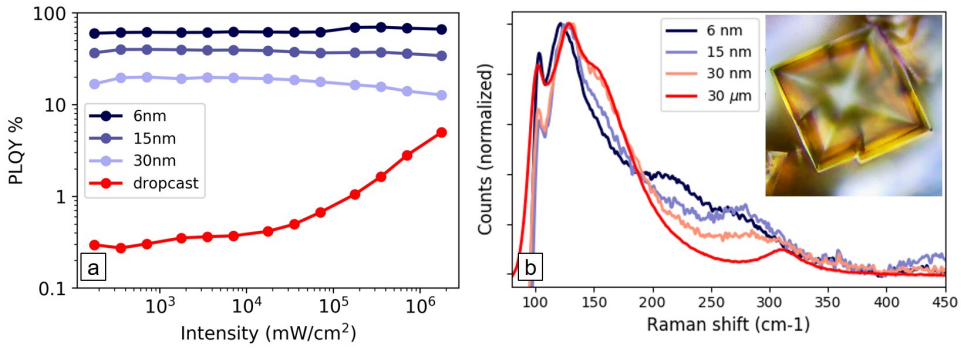

Figure 6.2: a) PLQY and of $CsPbBr_3$ NCs of different sizes, compared to a drop cast film with micrometer size crystallites; b) Raman spectra of the NCs of different sizes, compared to the spectrum of a 30 μm size crystal (inset).

Figure 6.2b shows the Raman spectra of the NCs of different sizes, compared to a micrometer-sized crystal. The differences in the lineshape can be interpreted as increasing lattice strain in the Pb-Br lattice[133]. This observation is in agreement with the relaxation of the lattice in 2D sheets of lead bromide perovskite, with increasing strain in stacked layers, as reported by Dou et al.[134]

The size dependence on the lattice strain could result in different phonon distributions and possibly affect the carrier recombination dynamics.[135] These effects, if present, could be related to intrinsic limits to the radiative efficiency of lead halide perovskites. Although not conclusive, these observations indicate some of the possibilities that lie ahead in the investigation of metal halide perovskite semiconductors.

7

Conclusions

To directly detect and identify defects in semiconductors is a very challenging task, even when they are present in relatively high densities as is the case of solution processed metal halide perovskites. Nonetheless, even a slight variation of defects in the lattice can have a strong impact in performance and stability of the semiconductor. One of the main tools used in this work is the photoluminescence efficiency and dynamics of the material, that, as discussed in Section 1.3, are extremely sensitive to various factors, including the presence of carrier trapping defects. Combining optical spectroscopy with theoretical predictions, this work takes one step further towards the understanding of the unusual defect properties of lead halide perovskites. The main conclusions of the work presented in the previous Chapters are summarized below.

Photoinduced healing and formation of defects

The inconsistency in observations has been an inconvenience to the research efforts involving lead halide perovskites, slowing down the understanding of its photophysics. The PL efficiency of thin films were monitored and its behavior was recorded under varied illumination conditions. When excluding atmospheric effects, it was revealed that photoexcitation can promote ion migration, resulting in either healing or formation of trapping sites, with opposite effects on the radiative efficiency. A model that associates PL quenching to the formation of surface-coordinated I_2 was proposed, pointing out the crucial role of

the surface on the photoinstabilities. These results provide a consistent framework which conciliates the various conflicting reports in literature regarding the photoinstability in metal halide perovskites. Moreover, it leads to a deeper understanding of the photophysical phenomena related to defects activity.

The effects of atmosphere

The effects of defect passivation upon exposure to oxygen and the detrimental effects of moisture over longer timescales have been demonstrated. The high sensitivity of the thin films to the presence of oxygen implies that the experiments are susceptible to variations in the semiconductor behavior depending on the atmospheric conditions. The effects of the atmosphere can also help in the development of surface treatment and encapsulation methods that maintain the benefits of defect passivation from short term exposure to air while protecting the film from the long term degradation.

Defect passivation and surface treatement

An effective method for improving the stability of perovskite solar cells was proposed, consisting of applying PEO, a hygroscopic polymer, as an interlayer. The polymer layer protects the perovskite from moisture degradation by retaining water molecules and also passivates surface defects. This improves the semiconductor photostability and the solar cell V_{oc}. This provides valuable information concerning the degradation of the perovskite layer and is also a promising strategy to improve solar cell stability.

Nature of defects and their role in recombination dynamics

Combining spectroscopic measurements with calculations, the main carrier trapping sites were identified and it was revealed that they are dominated by the halogen redox chemistry. It was shown that electron traps have very low detrapping rates due to energy barriers associated

with lattice distortions, and therefore can be filled under illumination, significantly reducing the effective trap density. Our results also imply that hole traps due to interstitial iodine can possibly be converted to less detrimental electron traps by controlling the oxidizing conditions during and after the film fabrication.

Bibliography

[1] Topsøe, Arzruni, A., and Bath, G. vom. "XVI.Auszüge". *Zeitschrift für Kristallographie - Crystalline Materials*, 8, 1-6, pp. 246–320. (1884).

[2] Mitzi, D. B., Wang, S., Feild, C. A., Chess, C. A., and Guloy, A. M. "Conducting layered organic-inorganic halides containing 110-oriented perovskite sheets". *Science*, 267, 5203, pp. 1473–1476. (1995).

[3] Chondroudis, K. and Mitzi, D. B. "Electroluminescence from an OrganicInorganic Perovskite Incorporating a Quaterthiophene Dye within Lead Halide Perovskite Layers". *Chemistry of Materials*, 11, 11, pp. 3028–3030. (1999).

[4] Kagan, C. R., Mitzi, D. B., and Dimitrakopoulos, C. D. "Organic-inorganic hybrid materials as semiconducting channels in thin- film field-effect transistors". *Science*, 286, 5441, pp. 945–947. (1999).

[5] Mitzi, D. B. "Thin-Film Deposition of OrganicInorganic Hybrid Materials". *Chemistry of Materials*, 13, 10, pp. 3283–3298. (2001).

[6] NREL. *Best Research-Cell Efficiencies*. URL: `https://www.nrel.gov/pv/assets/images/efficiency-chart.png` (visited on 05/23/2018).

[7] Li, G. et al. "Efficient light-emitting diodes based on nanocrystalline perovskite in a dielectric polymer matrix." *Nano letters*, 15, 4, pp. 2640–4. (2015).

[8] Sadhanala, A. et al. "Electroluminescence from Organometallic Lead Halide Perovskite-Conjugated Polymer Diodes". *Advanced Electronic Materials*, 1, 3, p. 1500008. (2015).

[9] Xing, G. et al. "Low-temperature solution-processed wavelength-tunable perovskites for lasing". *Nature Materials*, 13, 5, pp. 476–480. (2014).

[10] Yakunin, S. et al. "Low-threshold amplified spontaneous emission and lasing from colloidal nanocrystals of caesium lead halide perovskites". *Nature Communications*, 6, 1, p. 8056. (2015).

[11] Deschler, F. et al. "High Photoluminescence Efficiency and Optically Pumped Lasing in Solution-Processed Mixed Halide Perovskite Semiconductors". *The Journal of Physical Chemistry Letters*, 5, 8, pp. 1421–1426. (2014).

[12] Jia, Y., Kerner, R. A., Grede, A. J., Rand, B. P., and Giebink, N. C. "Continuous-wave lasing in an organic–inorganic lead halide perovskite semiconductor". *Nature Photonics*, 11, 12, pp. 784–788. (2017).

[13] Stranks, S. D. et al. "Electron-Hole Diffusion Lengths Exceeding 1 Micrometer in an Organometal Trihalide Perovskite Absorber". *Science*, 342, 6156, pp. 341–344. (2013).

[14] DeQuilettes, D. W. et al. "Photoluminescence Lifetimes Exceeding 8 µs and Quantum Yields Exceeding 30% in Hybrid Perovskite Thin Films by Ligand Passivation". *ACS Energy Letters*, 1, 2, pp. 1–7. (2016).

[15] Johnston, M. B. and Herz, L. M. "Hybrid Perovskites for Photovoltaics: Charge-Carrier Recombination, Diffusion, and Radiative Efficiencies". *Accounts of Chemical Research*, 49, 1, pp. 146–154. (2016).

[16] Shockley, W. and Queisser, H. J. "Detailed balance limit of efficiency of p-n junction solar cells". *Journal of Applied Physics*, 32, 3, pp. 510–519. (1961).

[17] Sha, W. E. I., Ren, X., Chen, L., and Choy, W. C. H. "The Efficiency Limit of CH 3 NH 3 PbI 3 Perovskite Solar Cells". *Applied Physics Letters*, 106, 22, (2015).

[18] Green, M. A. and Bein, T. "Perovskite cells charge forward". *Nature Materials*, 14, 6, pp. 559–561. (2015).

[19] Rose, G. "Ueber einige neue Mineralien des Urals". *Journal fr Praktische Chemie*, 19, 1, pp. 459–468. (1840).

[20] Wright, A. D. et al. "Electron-phonon coupling in hybrid lead halide perovskites". *Nature Communications*, 7, ncomms11755. (2016).

[21] Srimath Kandada, A. R. and Petrozza, A. "Photophysics of Hybrid Lead Halide Perovskites: The Role of Microstructure". *Accounts of Chemical Research*, 49, 3, pp. 536–544. (2016).

[22] DeQuilettes, D. W. et al. "Impact of microstructure on local carrier lifetime in perovskite solar cells". *Science*, 348, 6235, pp. 683–686. (2015).

[23] Grancini, G. et al. "Role of microstructure in the electron–hole interaction of hybrid lead halide perovskites". *Nat Photon*, 9, 10, pp. 695–701. (2015).

[24] Even, J. et al. "Solid-state physics perspective on hybrid perovskite semiconductors". *Journal of Physical Chemistry C*, 119, 19, pp. 10161–10177. (2015).

[25] Wang, T. et al. "Indirect to direct bandgap transition in methylammonium lead halide perovskite". *Energy & Environmental Science*, 10, 2, pp. 509–515. (2017).

[26] Motta, C. et al. "Revealing the role of organic cations in hybrid halide perovskite CH3NH3PbI3". *Nature Communications*, 6, 1, p. 7026. (2015).

[27] Niesner, D. et al. "Giant Rashba Splitting in CH3NH3PbBr3 Organic-Inorganic Perovskite". *Physical Review Letters*, 117, 12, p. 126401. (2016).

[28] Brivio, F., Butler, K. T., Walsh, A., and Schilfgaarde, M. van. "Relativistic quasiparticle self-consistent electronic structure of hybrid halide perovskite photovoltaic absorbers". *Physical Review B*, 89, 15, p. 155204. (2014).

[29] Frost, J. M. et al. "Atomistic Origins of High-Performance in Hybrid Halide Perovskite Solar Cells". *Nano Letters*, 14, 5, pp. 2584–2590. (2014).

[30] Filip, M. R., Eperon, G. E., Snaith, H. J., and Giustino, F. "Steric engineering of metal-halide perovskites with tunable optical band gaps". *Nature Communications*, 5, p. 5757. (2014).

[31] D'Innocenzo, V., Srimath Kandada, A. R., De Bastiani, M., Gandini, M., and Petrozza, A. "Tuning the Light Emission Properties by Band Gap Engineering in Hybrid Lead Halide Perovskite". *Journal of the American Chemical Society*, 136, 51, pp. 17730–17733. (2014).

[32] Grancini, G. et al. "The impact of the crystallization processes on the structural and optical properties of hybrid perovskite films for photovoltaics". *Journal of Physical Chemistry Letters*, 5, 21, pp. 3836–3842. (2014).

[33] Urbach, F. "The Long-Wavelength Edge of Photographic Sensitivity and of the Electronic Absorption of Solids". *Physical Review*, 92, 5, pp. 1324–1324. (1953).

[34] Shah, J. *Ultrafast Spectroscopy of Semiconductors and Semiconductor Nanostructures*. Vol. 115. Springer Series in Solid-State Sciences. Berlin, Heidelberg: Springer Berlin Heidelberg, 1999.

[35] Saba, M., Quochi, F., Mura, A., and Bongiovanni, G. "Excited State Properties of Hybrid Perovskites". *Accounts of Chemical Research*, 49, 1, pp. 166–173. (2016).

[36] Koch, S. W., Kira, M., Khitrova, G., and Gibbs, H. M. "Semiconductor excitons in new light". *Nature Materials*, 5, 7, pp. 523–531. (2006).

[37] Elliott, R. J. "Intensity of Optical Absorption by Excitons". *Physical Review*, 108, 6, pp. 1384–1389. (1957).

[38] Saba, M. et al. "Correlated electron–hole plasma in organometal perovskites". *Nature Communications*, 5, p. 5049. (2014).

[39] Saha, M. N. "On a Physical Theory of Stellar Spectra". *Proceedings of the Royal Society A: Mathematical, Physical and Engineering Sciences*, 99, 697, pp. 135–153. (1921).

[40] D'Innocenzo, V. et al. "Excitons versus free charges in organo-lead tri-halide perovskites." *Nature communications*, 5, p. 3586. (2014).

[41] Miyata, A. et al. "Direct measurement of the exciton binding energy and effective masses for charge carriers in organic–inorganic tri-halide perovskites". *Nature Physics*, 11, 7, pp. 582–587. (2015).

[42] Tanaka, K. et al. "Comparative study on the excitons in lead-halide-based perovskite-type crystals CH3NH3PbBr3 CH3NH3PbI3". *Solid State Communications*, 127, 9-10, pp. 619–623. (2003).

[43] Hirasawa, M., Ishihara, T., Goto, T., Uchida, K., and Miura, N. "Magnetoabsorption of the lowest exciton in perovskite-type compound (CH3NH3)PbI3". *Physica B: Condensed Matter*, 201, pp. 427–430. (1994).

[44] Sarritzu, V. et al. "Perovskite Excitonics: Primary Exciton Creation and Crossover from Free Carriers to a Secondary Exciton Phase". *Advanced Optical Materials*, 6, 3, p. 1700839. (2018).

[45] Droseros, N. et al. "Origin of the Enhanced Photoluminescence Quantum Yield in MAPbBr 3 Perovskite with Reduced Crystal Size". *ACS Energy Letters*, 3, 6, pp. 1458–1466. (2018).

[46] Kojima, A., Teshima, K., Shirai, Y., and Miyasaka, T. "Organometal Halide Perovskites as Visible-Light Sensitizers for Photovoltaic Cells". *Journal of the American Chemical Society*, 131, 17, pp. 6050–6051. (2009).

[47] Lee, M. M., Teuscher, J., Miyasaka, T., Murakami, T. N., and Snaith, H. J. "Efficient Hybrid Solar Cells Based on Meso-Superstructured Organometal Halide Perovskites". *Science*, 338, 6107, pp. 643–647. (2012).

[48] Mattheis, J., Werner, J. H., and Rau, U. "Finite mobility effects on the radiative efficiency limit of p-n junction solar cells". *Physical Review B*, 77, 8, p. 085203. (2008).

[49] Green, M. A. "Radiative efficiency of state-of-the-art photovoltaic cells". *Progress in Photovoltaics: Research and Applications*, 20, 4, pp. 472–476. (2012).

[50] Rau, U. "Reciprocity relation between photovoltaic quantum efficiency and electroluminescent emission of solar cells". *Physical Review B*, 76, 8, p. 085303. (2007).

[51] Tvingstedt, K. et al. "Radiative efficiency of lead iodide based perovskite solar cells". *Scientific Reports*, 4, 1, p. 6071. (2015).

[52] Nelson, J. *The Physics of Solar Cells*. Published by Imperial College Press and distributed by World Scientific Publishing co., May 2003.

[53] Ball, J. M. and Petrozza, A. "Defects in perovskite-halides and their effects in solar cells". *Nature Energy*, 1, 11, p. 16149. (2016).

[54] Leijtens, T. et al. "Carrier trapping and recombination: the role of defect physics in enhancing the open circuit voltage of metal halide perovskite solar cells". *Energy Environ. Sci.* 9, 11, pp. 3472–3481. (2016).

[55] Ayres, J. R. "Characterization of trapping states in polycrystalline-silicon thin film transistors by deep level transient spectroscopy". *Journal of Applied Physics*, 74, 3, pp. 1787–1792. (1993).

[56] Ueki, T., Itsumi, M., and Takeda, T. "Octahedral void defects observed in the bulk of Czochralski silicon". *Applied Physics Letters*, 70, 10, pp. 1248–1250. (1997).

[57] Balcioglu, A., Ahrenkiel, R. K., and Hasoon, F. "Deep-level impurities in CdTe/CdS thin-film solar cells". *Journal of Applied Physics*, 88, 12, pp. 7175–7178. (2000).

[58] Kerr, L. et al. "Investigation of defect properties in Cu(In,Ga)Se2 solar cells by deep-level transient spectroscopy". *Solid-State Electronics*, 48, 9, pp. 1579–1586. (2004).

[59] Yin, W.-J., Shi, T., and Yan, Y. "Unusual defect physics in CH 3 NH 3 PbI 3 perovskite solar cell absorber". *Applied Physics Letters*, 104, 6, p. 063903. (2014).

[60] Egger, D. A., Rappe, A. M., and Kronik, L. "Hybrid Organic-Inorganic Perovskites on the Move." *Accounts of chemical research*, 49, 3, pp. 573–81. (2016).

[61] Sanchez, R. S. et al. "Slow Dynamic Processes in Lead Halide Perovskite Solar Cells. Characteristic Times and Hysteresis". *The Journal of Physical Chemistry Letters*, 5, 13, pp. 2357–2363. (2014).

[62] Zhao, C. et al. "Revealing Underlying Processes Involved in Light Soaking Effects and Hysteresis Phenomena in Perovskite Solar Cells". *Advanced Energy Materials*, 5, 14, n/a–n/a. (2015).

[63] De Bastiani, M. et al. "Ion migration and the role of preconditioning cycles in the stabilization of the J-V characteristics of inverted hybrid perovskite solar cells". *Advanced Energy Materials*, 6, 2, p. 1501453. (2016).

[64] Tress, W. et al. "Understanding the rate-dependent J–V hysteresis, slow time component, and aging in CH 3 NH 3 PbI 3 perovskite solar cells: the role of a compensated electric field". *Energy & Environmental Science*, 8, 3, pp. 995–1004. (2015).

[65] Hoke, E. T. et al. "Reversible photo-induced trap formation in mixed-halide hybrid perovskites for photovoltaics". *Chem. Sci.* 6, 1, pp. 613–617. (2014).

[66] Sutter-Fella, C. M. et al. "Cation-Dependent Light-Induced Halide Demixing in Hybrid Organic–Inorganic Perovskites". *Nano Letters*, acs.nanolett.8b00541. (2018).

[67] DeQuilettes, D. W. et al. "Photo-induced halide redistribution in organic–inorganic perovskite films". *Nature Communications*, 7, p. 11683. (2016).

[68] Bischak, C. G. et al. *Origin of reversible photo-induced phase separation in hybrid perovskites*. June 2016. arXiv: 1606.07366. URL: http://arxiv.org/abs/1606.07366 (visited on 07/01/2016).

[69] Leijtens, T. et al. "Mapping electric field-induced switchable poling and structural degradation in hybrid lead halide perovskite thin films". *Advanced Energy Materials*, 5, 20, pp. 1–11. (2015).

[70] Deng, Y., Xiao, Z., and Huang, J. "Light-Induced Self-Poling Effect on Organometal Trihalide Perovskite Solar Cells for Increased Device Efficiency and Stability". *Advanced Energy Materials*, 5, 20, p. 1500721. (2015).

[71] Xiao, Z. et al. "Giant switchable photovoltaic effect in organometal trihalide perovskite devices". *Nature Materials*, 14, 2, pp. 193–198. (2015).

[72] Azpiroz, J. M., Mosconi, E., Bisquert, J., and De Angelis, F. "Defect migration in methylammonium lead iodide and its role in perovskite solar cell operation". *Energy Environ. Sci.* 8, 7, pp. 2118–2127. (2015).

[73] Yang, J.-H., Yin, W.-J., Park, J.-S., and Wei, S.-H. "Fast self-diffusion of ions in CH 3 NH 3 PbI 3 : the interstiticaly mechanism versus vacancy-assisted mechanism". *Journal of Materials Chemistry A*, 4, 34, pp. 13105–13112. (2016).

[74] Ming, W., Chen, S., and Du, M.-H. "Chemical instability leads to unusual chemical-potential-independent defect formation and diffusion in perovskite solar cell material CH 3 NH 3 PbI 3". *J. Mater. Chem. A*, 4, 43, pp. 16975–16981. (2016).

[75] Mosconi, E., Meggiolaro, D., Snaith, H. J., Stranks, S. D., and De Angelis, F. "Light-induced annihilation of Frenkel defects in organo-lead halide perovskites". *Energy Environ. Sci.* 9, 10, pp. 3180–3187. (2016).

[76] Tian, Y. et al. "Mechanistic insights into perovskite photoluminescence enhancement: light curing with oxygen can boost yield thousandfold". *Phys. Chem. Chem. Phys.* 17, 38, pp. 24978–24987. (2015).

[77] Galisteo-López, J. F., Anaya, M., Calvo, M. E., and Míguez, H. "Environmental Effects on the Photophysics of Organic-Inorganic Halide Perovskites." *The journal of physical chemistry letters*, 6, 12, pp. 2200–5. (2015).

[78] Fang, H.-H. et al. "Ultrahigh sensitivity of methylammonium lead tribromide perovskite single crystals to environmental gases". *Science Advances*, 2, 7, e1600534–e1600534. (2016).

[79] Aristidou, N. et al. "Fast oxygen diffusion and iodide defects mediate oxygen-induced degradation of perovskite solar cells." *Nature communications*, 8, p. 15218. (2017).

[80] Pelant, I. and Valenta, J. *Luminescence Spectroscopy of Semiconductors*. Oxford: Oxford University Press, 2012.

[81] Srimath Kandada, A. R. et al. "Nonlinear Carrier Interactions in Lead Halide Perovskites and the Role of Defects". *Journal of the American Chemical Society*, 138, 41, pp. 13604–13611. (2016).

[82] Yamada, Y., Nakamura, T., Endo, M., Wakamiya, A., and Kanemitsu, Y. "Photocarrier Recombination Dynamics in Perovskite CH 3 NH 3 PbI 3 for Solar Cell Applications". *Journal of the American Chemical Society*, 136, 33, pp. 11610–11613. (2014).

[83] Stranks, S. D. et al. "Recombination Kinetics in Organic-Inorganic Perovskites: Excitons, Free Charge, and Subgap States". *Physical Review Applied*, 2, 3, p. 034007. (2014).

[84] Wehrenfennig, C., Eperon, G. E., Johnston, M. B., Snaith, H. J., and Herz, L. M. "High Charge Carrier Mobilities and Lifetimes in Organolead Trihalide Perovskites". *Advanced Materials*, 26, 10, pp. 1584–1589. (2014).

[85] Cho, H. et al. "Overcoming the electroluminescence efficiency limitations of perovskite light-emitting diodes". *Science*, 350, 6265, pp. 1222–1225. (2015).

[86] Xiao, M. et al. "A Fast Deposition-Crystallization Procedure for Highly Efficient Lead(supporting)". *Angewandte Chemie*, 126, 37, pp. 10056–10061. (2014).

[87] Mello, J. C. de, Wittmann, H. F., and Friend, R. H. "An improved experimental determination of external photoluminescence quantum efficiency". *Advanced Materials*, 9, 3, pp. 230–232. (1997).

[88] Meggiolaro, D. et al. "Iodine chemistry determines the defect tolerance of lead-halide perovskites". *Energy & Environmental Science*, 11, 3, pp. 702–713. (2018).

[89] Brandt, R. E., Stevanović, V., Ginley, D. S., and Buonassisi, T. "Identifying defect-tolerant semiconductors with high minority-carrier lifetimes: beyond hybrid lead halide perovskites". *MRS Communications*, 5, 02, pp. 265–275. (2015).

[90] Yin, W. J., Shi, T., and Yan, Y. "Unique properties of halide perovskites as possible origins of the superior solar cell performance". *Advanced Materials*, 26, 27, pp. 4653–4658. (2014).

[91] Walsh, A., Scanlon, D. O., Chen, S., Gong, X. G., and Wei, S. H. "Self-regulation mechanism for charged point defects in hybrid halide perovskites". *Angewandte Chemie - International Edition*, 54, 6, pp. 1791–1794. (2015).

[92] Adinolfi, V. et al. "The In-Gap Electronic State Spectrum of Methylammonium Lead Iodide Single-Crystal Perovskites". *Advanced Materials*, 28, 17, pp. 3406–3410. (2016).

[93] Agiorgousis, M. L., Sun, Y. Y., Zeng, H., and Zhang, S. "Strong covalency-induced recombination centers in perovskite solar cell material CH3NH3PbI3". *Journal of the American Chemical Society*, 136, 41, pp. 14570–14575. (2014).

[94] Buin, A., Comin, R., Xu, J., Ip, A. H., and Sargent, E. H. "Halide-Dependent Electronic Structure of Organolead Perovskite Materials". *Chemistry of Materials*, 27, 12, pp. 4405–4412. (2015).

[95] Du, M.-H. "Density Functional Calculations of Native Defects in CH 3 NH 3 PbI 3 : Effects of Spin–Orbit Coupling and Self-Interaction Error". *The Journal of Physical Chemistry Letters*, 6, 8, pp. 1461–1466. (2015).

[96] Yamada, Y., Endo, M., Wakamiya, A., and Kanemitsu, Y. "Spontaneous defect annihilation in CH3NH3PbI3 thin films at room temperature revealed by time-resolved photoluminescence spectroscopy". *Journal of Physical Chemistry Letters*, 6, 3, pp. 482–486. (2015).

[97] Motti, S. G. et al. "Photoinduced formation, healing, and passivation of defects in lead halide perovskites". *under review*, (2018).

[98] Motti, S. G. et al. "Photoinduced Emissive Trap States in Lead Halide Perovskite Semiconductors". *ACS Energy Letters*, 1, 4, pp. 726–730. (2016).

[99] Priante, D. et al. "The recombination mechanisms leading to amplified spontaneous emission at the true-green wavelength in CH 3 NH 3 PbBr 3 perovskites". *Applied Physics Letters*, 106, 8, p. 081902. (2015).

[100] Meggiolaro, D., Mosconi, E., and De Angelis, F. "Mechanism of Reversible Trap Passivation by Molecular Oxygen in Lead-Halide Perovskites". *ACS Energy Letters*, 2, 12, pp. 2794–2798. (2017).

[101] Brennan, M. C., Draguta, S., Kamat, P. V., and Kuno, M. "Light-Induced Anion Phase Segregation in Mixed Halide Perovskites". *ACS Energy Letters*, 3, 1, pp. 204–213. (2018).

[102] Kim, G. Y. et al. "Large tunable photoeffect on ion conduction in halide perovskites and implications for photodecomposition". *Nature Materials*, 17, 5, pp. 445–449. (2018).

[103] Xing, J. et al. "Ultrafast ion migration in hybrid perovskite polycrystalline thin films under light and suppression in single crystals". *Physical Chemistry Chemical Physics*, 18, 44, pp. 30484–30490. (2016).

[104] Barker, A. J. et al. "Defect-Assisted Photoinduced Halide Segregation in Mixed-Halide Perovskite Thin Films". *ACS Energy Letters*, 2, 6, pp. 1416–1424. (2017).

[105] Chen, S. et al. "Light Illumination Induced Photoluminescence Enhancement and Quenching in Lead Halide Perovskite". *Solar RRL*, 1, 1, p. 1600001. (2017).

[106] Hong, D. et al. "Nature of Photo-induced Quenching Traps in Methylammonium Lead Triiodide Perovskite Revealed by Reversible Photoluminescence Decline". *ACS Photonics*, acsphotonics.7b01537. (2018).

[107] Varshni, Y. "Temperature dependence of the energy gap in semiconductors". *Physica*, 34, 1, pp. 149–154. (1967).

[108] Wright, A. D. et al. "Band-Tail Recombination in Hybrid Lead Iodide Perovskite". *Advanced Functional Materials*, 27, 29, p. 1700860. (2017).

[109] Boschloo, G. and Hagfeldt, A. "Characteristics of the Iodide/Triiodide Redox Mediator in Dye-Sensitized Solar Cells". *Accounts of Chemical Research*, 42, 11, pp. 1819–1826. (2009).

[110] Kim, M., Motti, S., Sorrentino, R., and Petrozza, A. "Enhanced Solar Cells Stability by Hygroscopic Polymer Passivation of Metal Halide Perovskite Thin Film". *Energy & Environmental Science, DOI: 10.1039/C8EE01101J*, (2018).

[111] Berhe, T. A. et al. "Organometal halide perovskite solar cells: degradation and stability". *Energy Environ. Sci.* 9, 2, pp. 323–356. (2016).

[112] Leijtens, T. et al. "Towards enabling stable lead halide perovskite solar cells; interplay between structural, environmental, and thermal stability". *Journal of Materials Chemistry A*, 5, 23, pp. 11483–11500. (2017).

[113] Aristidou, N. et al. "The Role of Oxygen in the Degradation of Methylammonium Lead Trihalide Perovskite Photoactive Layers". *Angewandte Chemie International Edition*, 54, 28, pp. 8208–8212. (2015).

[114] Huang, J., Tan, S., Lund, P., and Zhou, H. "Impact of H2O on organic-inorganic hybrid perovskite solar cells". *Energy Environ. Sci.* 10, 11, pp. 2284–2311. (2017).

[115] Christians, J. A., Miranda Herrera, P. A., and Kamat, P. V. "Transformation of the excited state and photovoltaic efficiency of CH3NH3PbI3 perovskite upon controlled exposure to humidified air". *Journal of the American Chemical Society*, 137, 4, pp. 1530–1538. (2015).

[116] Yang, J., Siempelkamp, B. D., Liu, D., and Kelly, T. L. "Investigation of CH3NH3PbI3degradation rates and mechanisms in controlled humidity environments using in situ techniques". *ACS Nano*, 9, 2, pp. 1955–1963. (2015).

[117] Bryant, D. et al. "Light and oxygen induced degradation limits the operational stability of methylammonium lead triiodide perovskite solar cells". *Energy & Environmental Science*, 9, 5, pp. 1655–1660. (2016).

[118] Zhang, L. and Sit, P. H.-L. "Ab initio study of the role of oxygen and excess electrons in the degradation of CH 3 NH 3 PbI 3". *Journal of Materials Chemistry A*, 5, 19, pp. 9042–9049. (2017).

[119] Feng, X. et al. "Photon-generated carriers excite superoxide species inducing long-term photoluminescence enhancement of MAPbI ₃ perovskite single crystals". *Journal of Materials Chemistry A*, 5, 24, pp. 12048–12053. (2017).

[120] Leguy, A. M. A. et al. "Reversible Hydration of CH 3 NH 3 PbI 3 in Films, Single Crystals, and Solar Cells". *Chemistry of Materials*, 27, 9, pp. 3397–3407. (2015).

[121] Fan, R. et al. "The Progress of Interface Design in Perovskite-Based Solar Cells". *Advanced Energy Materials*, 6, 17, p. 1600460. (2016).

[122] Deng, W., Liang, X., Kubiak, P. S., and Cameron, P. J. "Molecular Interlayers in Hybrid Perovskite Solar Cells". *Advanced Energy Materials*, 8, 1, p. 1701544. (2018).

[123] Tress, W. et al. "Interpretation and evolution of open-circuit voltage, recombination, ideality factor and subgap defect states during reversible light-soaking and irreversible degradation of perovskite solar cells". *Energy & Environmental Science*, 11, 1, pp. 151–165. (2018).

[124] Bella, F. et al. "Improving efficiency and stability of perovskite solar cells with photocurable fluoropolymers". *Science*, 354, 6309, pp. 203–206. (2016).

[125] Koushik, D. et al. “High-efficiency humidity-stable planar perovskite solar cells based on atomic layer architecture”. *Energy & Environmental Science*, 10, 1, pp. 91–100. (2017).

[126] Akkerman, Q. A. et al. “Strongly emissive perovskite nanocrystal inks for high-voltage solar cells”. *Nature Energy*, 2, 2, p. 16194. (2017).

[127] Zhu, H. et al. “Lead halide perovskite nanowire lasers with low lasing thresholds and high quality factors.” *Nature materials*, 14, 6, pp. 636–642. (2015).

[128] Zhang, F. et al. “Brightly Luminescent and Color-Tunable Colloidal CH 3 NH 3 PbX 3 (X = Br, I, Cl) Quantum Dots: Potential Alternatives for Display Technology”. *ACS Nano*, 3, 4, p. 150401163757003. (2015).

[129] Protesescu, L. et al. “Nanocrystals of Cesium Lead Halide Perovskites (CsPbX 3 , X = Cl, Br, and I): Novel Optoelectronic Materials Showing Bright Emission with Wide Color Gamut”. *Nano Letters*, 15, 6, pp. 3692–3696. (2015).

[130] Akkerman, Q. A. et al. “Solution Synthesis Approach to Colloidal Cesium Lead Halide Perovskite Nanoplatelets with Monolayer-Level Thickness Control”. *Journal of the American Chemical Society*, 138, 3, pp. 1010–1016. (2016).

[131] Akkerman, Q. a. et al. “Tuning the Optical Properties of Cesium Lead Halide Perovskite Nanocrystals by Anion Exchange Reactions”. *Journal of the American Chemical Society*, p. 150727153906000. (2015).

[132] Yettapu, G. R. et al. “Terahertz Conductivity within Colloidal CsPbBr 3 Perovskite Nanocrystals: Remarkably High Carrier Mobilities and Large Diffusion Lengths”. *Nano Letters*, 16, 8, pp. 4838–4848. (2016).

[133] Quarti, C. et al. “The raman spectrum of the CH3NH3PbI3 hybrid perovskite: Interplay of theory and experiment”. *Journal of Physical Chemistry Letters*, 5, 2, pp. 279–284. (2014).

[134] Dou, L. et al. “Atomically thin two-dimensional organic-inorganic hybrid perovskites”. *Science*, 349, 6255, pp. 1518–1521. (2015).

[135] Vanacore, G. M. et al. “Diffraction of Quantum Dots Reveals Nanoscale Ultrafast Energy Localization”. *Nano Letters*, 14, 11, pp. 6148–6154. (2014).

Publications

[1] Akkerman, Q. A., **Motti, S. G.**, Srimath Kandada, A. R., Mosconi, E., D'Innocenzo, V., Bertoni, G., Marras, S., Kamino, B. A., Miranda, L., De Angelis, F., Petrozza, A., Prato, M., Manna, L., D'Innocenzo, V., Bertoni, G., Marras, S., Kamino, B. A., Miranda, L., De Angelis, F., Petrozza, A., Prato, M., and Manna, L. "Solution Synthesis Approach to Colloidal Cesium Lead Halide Perovskite Nanoplatelets with Monolayer-Level Thickness Control". *Journal of the American Chemical Society*, 138, 3, pp. 1010-1016. (2016)

[2] **Motti, S. G.**, Gandini, M., Barker, A. J., Ball, J. M., Srimath Kandada, A. R., and Petrozza, A. "Photoinduced Emissive Trap States in Lead Halide Perovskite Semiconductors". *ACS Energy Letters*, 1, 4, pp. 726-730. (2016)

[3] Paternò, G. M., Chen, Q., Wang, X.-Y., Liu, J., **Motti, S. G.**, Petrozza, A., Feng, X., Lanzani, G., Müllen, K., Narita, A., and Scotognella, F. "Synthesis of Dibenzo[hi,st]ovalene and Its Amplified Spontaneous Emission in a Polystyrene Matrix". *Angewandte Chemie International Edition*, 56, 24, pp. 6753-6757. (2017)

[4] Meggiolaro, D., **Motti, S. G.**, Mosconi, E., Barker, A., Ball, J., Perini, C. A. R., Deschler, F., Petrozza, A., and De Angelis, F. "Iodine chemistry determines the defect tolerance of lead-halide perovskites". *Energy & Environmental Science*, 11, 3, pp. 702-713. (2018)

[5] Robbiano, V., Paterno, G. M., La Mattina, A. A., **Motti, S. G.**, Lanzani, G., Scotognella, F., and Barillaro, G. "Room-Temperature Low-Threshold Lasing From Monolithically Integrated Nanostructured Porous Silicon Hybrid Microcavities". *ACS Nano*, acsnano.8b00875. (2018)

[6] Kim, M., **Motti, S. G.**, Sorrentino, R., and Petrozza, A. "Enhanced Solar Cells Stability by Hygroscopic Polymer Passivation of Metal Halide Perovskite Thin Film". *Energy & Environmental Science*, DOI: 10.1039/C8EE01101J (2018)

[7] **Motti, S. G.**, Barker, A. J., Perini, C. A. R., Ball, J. M., Gandini, M., Kim, M. and Petrozza, A. "Competing photo-induced trap formation and healing in lead halide perovskites". *Under review.* (2018)

Acknowledgments

This work has been funded by *Conselho Nacional de Desenvolvimento Científico e Tecnológico* (CNPq).

I'll always be grateful to Prof. Guglielmo Lanzani for replying my first contact and accepting me in CNST, opening the first door that brought me here. I am specially grateful to my supervisor Dr. Annamaria Petrozza, who took me in her group and directed my efforts in the right direction. Her enthusiasm and vision stabilized my skepticism and frustrations, providing the right balance to build this work on. I thank Anna and Guglielmo for the trust deposited in me and for the fundamental support in taking the next steps of my career and personal life. My first mentor upon arrival was Ajay, to whom I am deeply grateful for having the patience to guide my steps in the new labs with his much valuable knowledge and expertise. I thank my spectroscopy colleagues Alex, Stefanie, and Ilaria for the support, for the (not always) scientific discussions, and for sharing the joys and sorrows of the spectroscopy life.

For the fabrication of the samples, I thank Min Kim, Marina, James, Carlo, and Roberto, those who never failed to keep up with our extravagant requests. Special thanks to Filippo de Angelis and Daniele Meggiolaro for the long Skype meetings, the stimulating discussions and the theoretical support for our data. I also thank the CNST staff: Silvia, Tessa, Alessandra, Stefano, Martina, Luca, Enrico, Andrea, those that keep the place standing and the work flowing, and I thank my old and

new spectroscopy colleagues at CNST: Giuseppe, Tania, Egle, Gabriel, Valerio and all my other colleagues in Anna's group for putting together the physical and intellectual structure that allowed me to carry out this work.

Besides all the science, starting a life in a new country is a great learning experience by itself. I'd also like to thank Isis, Stefanie, Alex, and all my friends for sharing these 3 years and helping out whenever needed. Most of all I thank James for the constant and fundamental support. Last but not least, I thank my family, who was the first and most important base for my personal, professional, and educational development.

Nobody ever figures out what life is all about, and it doesn't matter. Explore the world. Nearly everything is really interesting if you go into it deeply enough.

— Richard Feynman